From Strong Plates to Weak Boundaries: Strain Localization in the Lithospheric Mantle with Low- to High-Temperature Dislocation Creep

Etienne Van Broeck[1], Fanny Garel[1], Catherine Thoraval[1], Diane Arcay[1], and D. Rhodri Davies[2]

[1]Géosciences Montpellier, Université de Montpellier, CNRS, Montpellier, France
[2]Research School of Earth Sciences, The Australian National University, Canberra, ACT, Australia

Correspondence: Etienne Van Broeck (etienne.van-broeck@umontpellier.fr) and Fanny Garel (fanny.garel@umontpellier.fr)

Abstract. Plate-like behavior ~~may be reproduced in numerical experiments of mantle convection if rheology combines a~~ in mantle convection models is commonly obtained using a strongly temperature-dependent viscosity ~~capped~~ together with a low yield stress ~~. Other processes limiting the mantle ductile strengthhave been proposed, among which~~ that caps lithospheric strength. Yet, alternative mechanisms for limiting ductile strength, including low-temperature plasticity~~. We propose to investigate how such a rheology can promote deformation localizationat the lithospheric scale. We design a~~ , have been proposed. Here, we investigate how different rheological formulations promote lithospheric-scale strain localization, using 2-D thermo-mechanical ~~model of plate extensionto compare the modes of strain localization as a function of the rheological parameterization. Various experimental flow laws for olivine~~ simulations of upper mantle extension. We test a suite of olivine flow laws (diffusion creep and dislocation creep at low- and/or ~~high- temperature)are tested, sometimes combined with~~ high-temperature), with and without a yield-stress ~~formulation. We quantify the evolution of the deformation pattern throughout the lithosphere, and define new diagnostics to assess whether the decrease in plate viscosity is due to an increase in~~ cap, and introduce diagnostics that attribute plate weakening to either increasing strain rate (~~'mechanical weakening') and/or in temperature ('thermal weakening'). Deformation localization leads to~~ mechanical weakening) or increasing temperature (thermal weakening). Without a yield-stress cap, deformation remains distributed in all cases, indicating that weakening of the cold upper lithosphere is required in addition to ductile creep. In localizing simulations, a new extensional plate boundary ~~in two successive stages: (i)~~ develops in two stages: progressive narrowing of the deforming zone ~~, (ii)~~ followed by rapid thinning of the ~~highly deformed lithosphere. Here, a rheology combining diffusion creep and yield stress results in a mantle weakening that is either fully mechanical, respectively fully thermal, for temperatures lower, respectively higher, than $\sim$1300 K. Accounting for dislocation creep enables additional feedbacks between~~ weakened lithosphere. Across plate ages of 10-100 Myr, localization depends weakly on age but strongly on divergence rate, primarily through Stage-1 narrowing, and is controlled more by the stiffest lithospheric region than by the presence of a shallow weak layer. Including dislocation creep allows both mechanical and thermal weakening to operate within the deforming plate, ~~thereby enhancing the efficiency of strain localization . We demonstrate the consistency of using a~~ enhancing feedbacks and accelerating localization relative to yield-stress ~~approximation to cap the mantle strength for temperature below $\sim$1000 K. We also show that dislocation creep and~~ plus diffusion creep. This implies that yield-stress~~are not interchangeable for most of the lithospheric mantle (1000-1500 K), and using only the latter may~~

~~overestimate the duration of plate~~ /diffusion-only rheologies may overestimate break-up timescales in whole-mantle convection models. Low-temperature dislocation creep weakens the plate at 800-1000 K, providing a physically grounded mechanism for limiting ductile strength in this temperature range. Finally, we ~~discuss how our results compare to natural continental rifting cases .~~ propose that thermal weakening may in some cases promote rapid strength loss and accelerated extension during the late stages of natural rift evolution.

1 Introduction

Plate ~~tectonic theory~~ tectonics describes the motion of rigid lithospheric plates separated by ~~weak lubricating boundaries (Le Pichon, 1968)~~narrow, weak boundaries (e.g. Le Pichon, 1968). Observations from seismicity and geodetic strain-rate fields ~~derived from geodetic data confirm that most intraplate regions undergo only minor deformation , while strain~~ show that most deformation is concentrated within ~~narrow, seismically active plate boundaries(Kreemer et al., 2014). Yet~~these plate boundaries, while most plate interiors deform only weakly (e.g. Kreemer et al., 2014). However, broad intraplate deformation zones ~~are also observed~~also exist, for example between the India and Australia plates (e.g. Iaffaldano et al., 2018). ~~Reconstructions of past plate configurations demonstrate~~ In addition, plate reconstructions indicate that the number, size~~and arrangement~~, and organization of plates have ~~evolved significantly~~ changed through geological time ~~(Morra et al., 2013) . New boundaries may form either through the reactivation of pre-existing weak zones (e.g. sutures) or by the localization of initially distributed deformation, as reconstructed~~ (e.g. Morra et al., 2013), implying that plate boundaries are created, reorganized, and abandoned. Such transient boundary formation is evident in incipient continental rifts (Müller et al., 2019), back-arc basins ~~, or incipient subduction zones (Lallemand and Arcay, 2021).~~

~~Lithosphere weakening is necessary to sustain large lateral strength contrasts in the plate tectonics regime (Bercovici et al., 2015) .Laboratory experiments on~~ (Sdrolias and Müller, 2006), or subduction initiation settings (Lallemand and Arcay, 2021). New plate boundaries may develop by reactivating inherited weak zones (e.g. Mazzotti and Gueydan, 2018; Fuchs and Becker, 2022; Brune et al or by localizing initially distributed deformation into a narrow shear zone (e.g. Lamb and Watts, 2010; Schmalholz et al., 2014; Asti et al., 2 . Understanding when and how distributed deformation localizes remains central to explaining the dynamics of plate creation and the emergence of plate-like behavior in mantle convection.

A key difficulty is that the lithospheric mantle is expected to be very strong under cold, ductile conditions. For olivine, the dominant mineral in the lithospheric mantle, ~~yield rheological flow laws that predict high strength at lithospheric conditions, typically ∼700 MPa for temperatures below 1500 K (e.g., Kohlstedt et al., 1995). However, mantle convection simulations incorporating such ‘power law’ creep flow laws lead to a stagnant-lid regime when viscosity is~~ high-temperature power-law dislocation creep predicts large flow stresses in the cold ductile lithosphere (often exceeding hundreds MPa) (Kohlstedt et al., 1995; Karato, . By contrast, estimates of available tectonic driving forces, of order 2 to 50 TN m^{-1}, suggest that plate interiors do not deform at deviatoric stresses below 200 MPa unless additional weakening processes operate (Parsons and Richter, 1980). Consistent with this, strongly temperature-dependent ~~(Solomatov and Moresi, 1997), implying that an additional weakening mechanism is required (Solomatov, 2004).~~

~~Over the past decades, several candidate processes of weakening at lithospheric scale have been investigated~~non-Newtonian viscosity alone is insufficient to promote lithospheric break-up (Bercovici, 1993), and instead tends to produce stagnant-lid convection (e.g. Solomatov and Moresi, 1997). Generating plate-like behavior therefore requires mechanisms that both reduce lithospheric strength and promote strain localization (e.g. Solomatov, 2004; Mulyukova and Bercovici, 2019).

Many candidate weakening processes have been explored at lithospheric scales, including shear heating ~~(Fleitout and Froidevaux, 1980; Ka , anisotropic viscosity (Tommasi et al., 2009; Mameri et al., 2021)~~(e.g. Yuen and Schubert, 1979; Brun and Cobbold, 1980; Fleitout and Fr

, viscous anisotropy (e.g. Tommasi et al., 2009; Mameri et al., 2021; Duretz et al., 2025), strain softening ~~(Gueydan et al., 2014; Meyer et a~~ or damage formulations (e.g. Gueydan et al., 2014; Meyer et al., 2017; Tarayoun et al., 2019; Frederiksen and Braun, 2001), and grain-size reduction ~~with~~ leading to diffusion creep and/or grain-boundary sliding ~~(Bercovici, 2003; Bercovici and Ricard, 2013; Gueydan a~~ ~~. A common modeling approach has been to introduce a depth-dependent yield stress in combination with~~ (e.g. Bercovici and Ricard, 2013; . A widely used pragmatic approach in mantle convection modeling is to combine temperature-dependent creep ~~, which can reproduce plate-like behavior in mantle convection models (Tackley, 2000a; Rolf et al., 2012; Coltice et al., 2017, 2019; Ulvrova et al., 201~~ ~~. This parameterization is often treated as an analogue for brittle deformation. Yet, the yield stresses required to generate~~ with a yield-stress cap, which limits effective lithospheric strength and enables mobile-lid or plate-like ~~regimes ($< 200-300$ MPa, Crameri and Ta~~ ~~, imply~~ regimes (e.g. Moresi and Solomatov, 1998; Trompert and Hansen, 1998; Tackley, 1998; Korenaga, 2010; Nakagawa and Iwamori, . However, the required stress limits are typically low ($\lesssim$200-300 MPa, e.g. Richards et al., 2001; Crameri and Tackley, 2014; Mallard et al and correspond to effective friction coefficients ~~below 0.1, in stark contrast with laboratory values closer to 0.6 (Byerlee, 1978)~~ ~~, corresponding to lithospheric strengths greater than 500 MPa (Iaffaldano, 2012; Burov, 2011a, b).~~

~~Recent advances offer an alternative. Numerical crystal-scale simulations of dislocation dynamics in olivine suggest~~ (often $\lesssim 0.2$, e.g. Mo substantially below laboratory values (~ 0.6, e.g. Byerlee, 1978).

Low-temperature ductile deformation has been proposed as an alternative route to limiting lithospheric strength without imposing an ad-hoc stress cap throughout the ductile regime. Experiments show that olivine can deform under high-stress, low-temperature conditions following an exponential (Peierls-type) flow law (Frost and Ashby, 1982; Mei et al., 2010; Demouchy et al., 20 . Low-temperature dislocation creep has also been invoked to explain deformation of subducting slabs in the transition zone (Čížková et al., 2002; Garel et al., 2014). More recently, dislocation-dynamics models have provided a unified description of olivine dislocation creep that bridges classical high-temperature power-law creep and low-temperature Peierls creep, suggesting a continuous mechanical behavior across a wide range of temperatures and ~~strain-rates, mimicking a Peierls-type stress rheology (Gouriet et al., 2019). Expressed as a non-Newtonian dislocation creep viscosity, this rheology may enable the necessary feedbacks between deformation and weakening.~~

~~In this study~~strain rates controlled by the interplay of glide and climb (Gouriet et al., 2019). This unified formulation has already been implemented in geodynamical simulations to investigate feedbacks that weaken the asthenosphere around sinking slabs (Garel et al., 2020).

Here, we evaluate ~~for the first time the ability of the unified low-to-high-temperature (LT-HT~~the capacity of a unified low-to high-temperature (LT–HT) dislocation creep formulation ~~(Gouriet et al., 2019; Garel et al., 2020) to localize deformation in the lithospheric mantle~~(Gouriet et al., 2019; Garel et al., 2020) to promote lithospheric-scale strain localization in a controlled extensional setting. We compare its ~~behavior with other widely used ductile rheological formulations. To do so, we design~~ dynamical behavior with that obtained using commonly employed mantle rheologies (diffusion creep and/or high-temperature dislocation creep), with and without a yield-stress cap. Strain localization in geodynamical models is usually quantified using geometric measures such as 'plateness' (Weinstein and Olson, 1992; Tackley, 2000a) or relative shear-zone width 'localization potential' (Montési, 2013), while bulk plate strength can be inferred from the tectonic force required to sustain imposed kinematics (Brune et al., 2012). Recent studies have also introduced diagnostics of weakening to compare deformation mechanisms in subduction settings (Patočka et al., 2024), alongside theoretical analyses of weakening potentials (Montési and Zuber, 2002) or in simplified frameworks (Kaus and Podladchikov, 2006; Schmalholz and Fletcher, 2011). However, there remains a need for time-dependent diagnostics that track not only whether viscosity decreases, but also why it decreases as thermal and kinematic fields evolve self-consistently.

To address this, we introduce diagnostics that partition local viscosity change into contributions from increasing strain rate (mechanical weakening) and increasing temperature (thermal weakening) during localization. We apply these diagnostics to 2-D ~~numerical models of plate extension , with various~~ thermo-mechanical simulations of lithospheric extension across a range of initial plate ages and ~~extension velocities (Sect. 2)~~imposed extension rates. In this ~~set-up, spatial strain localization~~ framework, deformation focusing and plate thinning ~~- associated to an asthenosphere upwelling- promote an increase in temperature~~ are coupled to asthenospheric upwelling, enabling positive feedbacks that amplify strain rate and/or ~~in strain rate. Thus, this framework is ideal to investigate feedbacks associated with strain-rate and temperature-dependent rheologies.~~

~~To analyze the results, we apply and extend a suite of quantitative diagnostics , including measure of plateness (Tackley, 2000a) , tectonic forces required to maintain extension (Brune et al., 2012).Whereas previous studies have largely relied on static measures of localization efficiency for a given rheology (Montési and Zuber, 2002), we develop new time-dependent diagnostics to track the sequential processes that lead to plate weakening.~~

temperature increase depending on the rheological formulation. To isolate weakening processes within the lithospheric mantle, we model a single mantle material and intentionally neglect crustal layering and associated lithological and rheological contrasts. This simplified configuration is designed to clarify how low- to high-temperature dislocation creep, relative to yield-stress and diffusion-only parameterizations, controls the efficiency, depth distribution, and timescale of lithospheric-scale strain localization in the mantle.

In the remainder of the paper, we first describe the thermo-mechanical extension set-up, the rheological formulations tested, and the numerical implementation (Sect. 2). We then introduce post-processing diagnostics that quantify strain localization, plate thinning and bulk plate strength, and that partition viscosity change into strain-rate-driven and temperature-driven contributions (Sect. 3). We present results in four steps: (i) end-member deformation outcomes in a reference configuration, (ii) a two-stage localization trajectory and characteristic timescales in a representative localizing case, (iii) a comparison across rheological combinations to identify which dependencies control localization efficiency and the depth/temperature range of weakening, and (iv) sensitivity to initial plate age and imposed extension rate (Sect. 4). Finally, we discuss the implications for lithospheric weakening in natural rift systems, and for yield-stress-based parameterizations commonly used in whole-mantle convection models, and summarize the main conclusions (Sects. 5 and Conclusions).

2 Methods: thermo-mechanical model

2.1 Extension Set-Up

We construct a 2-D thermo-mechanical model of upper-mantle extension ~~,~~ in which lithospheric strength (viscosity) depends ~~both on~~ on both strain rate and temperature. The model domain is a 1200-km wide by 400-km deep rectangle composed entirely of mantle material (~~see properties,~~ Table 1).

This mantle-only configuration is designed to isolate strain localization within the lithospheric mantle (e.g. Gueydan and Précigout, 2014 and to facilitate comparison with large-scale plate-like convection models, which commonly neglect crustal structure and employ simplified rheologies.
Accordingly, we do not model crust-mantle interactions or full continental rift mechanics. This is a deliberate simplification, as crustal layering can reduce bulk lithospheric strength and introduce rheological contrasts that enhance localization in the mantle through crust-mantle mechanical coupling (e.g. Allemand and Brun, 1991; Burov and Watts, 2006; Rosenbaum et al., 2010). In many numerical rift models, strong coupling across rheological discontinuities favors a 'narrow-rift' style of deformation (e.g. Huismans and Beaumont, 2005; Gueydan et al., 2008; Chenin et al., 2018; Duclaux et al., 2020; Zwaan et al., 2021; Wang et al., 202 . In our set-up, localization is instead controlled by mantle rheology and by the imposed yield-stress parameterization (Sect. 2.2), allowing us to isolate how these ingredients influence the onset and evolution of localized extension.

Table 1. Parameter names and values for the model set-up.

Parameter	Symbol	Value	Unit
Box length	L	1200	km
Box height	H	400	km
Surface temperature	T_s	273	K
Mantle temperature	T_m	1600	K
Material properties			
~~Volumic mass~~ Density	ρ_{mantle}	3300	kg m^{-3}
Thermal diffusivity	κ	$1.\ 10^{-6}$	m^2 s^{-1}
Thermal expansivity	α	$3.\ 10^{-5}$	K^{-1}

~~Our focus is indeed on the weakening of the lithospheric mantle, which is a prerequisite to trigger intraplate strain localization (e.g. Gueydan and Précigout, 2014) even if the presence of a crustal layer lowers surface lithospheric strength and introduces strength contrasts (e.g. Burov and Watts, 2006).~~

The initial thermal ~~state~~ structure is prescribed using the half-space cooling model for a laterally uniform plate age. ~~Boundary conditions are as follows: the top surface is fixed at~~ Thermal boundary conditions are fixed temperatures of $T_s = 273$ K ~~, the base at~~ at the surface and $T_m = 1600$ K ~~, and the vertical sides are thermally insulating~~ at the base, with thermally insulating vertical sides (Fig. 1). The initial deformation state is derived from a purely horizontal velocity field, ~~leading~~

~~to a quasi-homogeneous initial intraplate strain rate $\dot{\varepsilon}_{t_0}$ (~~producing a nearly uniform initial strain rate in the plate ($\dot{\varepsilon}_{t_0}$ = 3.73 10^{-16} s^{-1} for $v_{1/2} = 1$ cm yr^{-1}, Fig. 2).~~This initial velocity field is calculated from the simulation lateral boundary conditions, where extension is imposed by prescribing symmetric, purely horizontal,~~ Extension is imposed through symmetric, depth-dependent ~~outflow velocities~~ horizontal outflow velocities on the side boundaries (Fig. 1). ~~This~~ The vertical profile $v_x(z)$ is ~~derived~~ obtained from a 1-D Couette ~~shear flow~~ solution with surface velocity $v_{1/2}$ and zero velocity at the base, calculated ~~for~~ using the depth- and ~~temperature dependent~~ temperature-dependent diffusion-creep viscosity ~~(eq. 1) of a 50-Myr old plate (Appendix ??~~of a 50-Myr-old plate (detailed in Supplementary Material S.1.2.1). This corresponds to an effective ~~'~~constant-velocity plate ~~' 89-km~~ 89 km thick, defined as the depth ~~at~~ above which horizontal velocity ~~deviates by more~~ differs by less than 1 % from $v_{1/2}$ (Garel and Thoraval, 2021). ~~Sensitivity tests varying the plate age used to define $v_x(z)$ confirm that this approximation does not significantly influence~~ Additional tests with alternative side-boundary velocity profiles produce no significant change in the results (~~Appendix ??).~~

detailed in Supplementary Material S.1.2.3). The upper boundary is treated as a free surface (Kramer et al., 2012). At the base, ~~a mixed condition is applied:~~ no-slip and closed ($v_x = v_z = 0$) is imposed on the lateral segments, while ~~a vertical inflow (~~vertical inflow with $v_x = 0$ ~~) is permitted~~ is allowed across a 600 km-wide central ~~part (Appendix ??), ensuring that strain localization develops preferentially~~ segment (see Supplementary Material S.1.2.2). This promotes localization at the domain center ~~. The central inflow, $v_z(x)$, evolves dynamically to balance time-dependent surface deformation and the prescribed lateral outflow~~ (see Fig. S3 in Supplementary Material), while allowing basal inflow to adjust dynamically to the imposed lateral outflow (see Fig. S7 in Supplementary Material S.1.2.4) and evolving surface deformation.

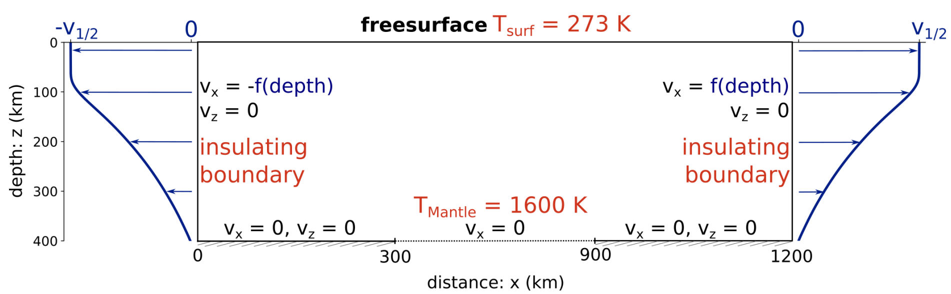

Figure 1. Simulation set-up in the 400×1200 km 2-D domain. ~~The mechanical~~ Mechanical boundary conditions (in blue) are a ~~free~~ free-surface top~~surface~~, and depth-dependent horizontal flow on the vertical sides, where $v_{1/2}$ is the plate half extension rate~~(Appendix ??)~~. ~~In most simulations, the box~~ The bottom boundary is no-slip and closed ($v_z = v_x = 0$), except over a ~~600-km-wide~~ 600 km-wide open segment ~~located~~ between ~~x =300~~ $x = 300$ and 900 km where purely vertical ~~velocity is free and horizontal velocity set to zero. In a one simulation, this vertical inflow~~ flow is ~~imposed~~ allowed (~~see Appendix ??~~$v_x = 0$). ~~The thermal~~ Thermal boundary conditions (in red) are constant temperatures at top (273 K) and bottom (1600 K), ~~while~~ and insulating vertical boundaries~~are insulating~~.

We first analyze different rheological parameterizations ~~using~~ in a reference configuration with $v_{1/2} = 1$ cm yr^{-1} and an initial plate age of 50 ~~Myrs~~ Myr (Sect. 4.1, 4.2 and 4.3). We then explore the influence of ~~plate resistance and far-field forcing~~

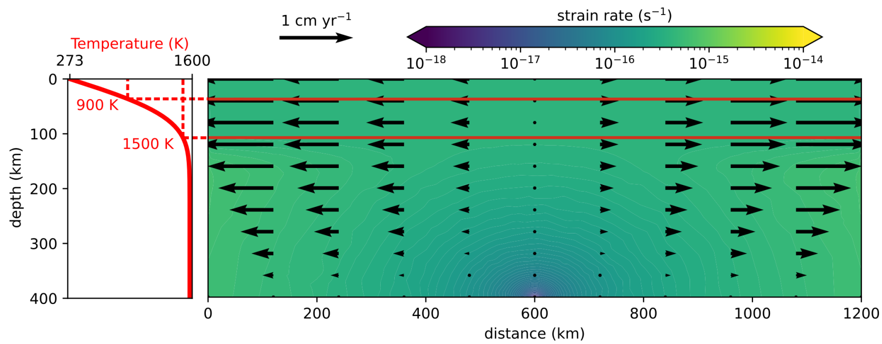

Figure 2. Initial conditions ~~:~~ showing (left) the temperature field calculated from the half-space cooling model (~~left panel:~~ temperature profile $T(z)$ for a 50 ~~Myrs-old~~ Myr-old plate) and (right) the second invariant strain rate $\dot{\varepsilon}_{t_0}$ (~~right panel -~~ here $\sim$3.73 10^{-16} s^{-1} for a half extension rate $v_{1/2}$~~equal to~~ =1 cm yr^{-1}). The imposed initial velocity field is depicted by black arrows, ~~and~~ with red lines indicating the 900 K and 1500 K isotherms~~using red lines~~. This purely velocity field ($v_z = 0$) is calculated by assuming at each depth a linear increase of the horizontal velocity along x from the domain center ($v_x(x = 600$ km$) = 0$) to the domain sides, where a Couette velocity is imposed at a boundary condition (cf $v_x(z)$ calculation for $x = 0$ or 1200 km in Supplementary material S1.2.1).

~~by varying plate age from 10 to 100 Myrand spreading velocity from~~ initial plate age (10-100 Myr) and half-extension rate (0.2~~to 5~~ -5 cm yr^{-1}) on localization behaviour (Sect. 4.4).

2.2 Rheological parameterization

2.2.1 Mechanisms of mantle deformation

Viscous deformation ~~of the mantle~~ is represented by combinations of (i) olivine creep flow laws ~~(diffusion and/or dislocation creep)~~ and (ii) a stress-limited viscosity ('yield stress'). ~~Creep flow laws are~~ The creep laws include diffusion creep and dislocation creep, based on experimental and numerical ~~studies of olivine deformation (e.g. Hirth and Kohlstedt, 1995a, b; Gouriet et al., 20~~ ~~, assuming~~ constraints on olivine deformation (e.g. Hirth and Kohlstedt, 1995a, b; Gouriet et al., 2019). We assume that multiple creep mechanisms may operate simultaneously (~~see~~ Sect. 2.2.2).

~~In contrast, a~~

A yield-stress formulation ~~has been widely adopted~~ is included in some simulations because such stress caps are widely used in geodynamical models to reproduce mobile-lid or plate-like behavior ~~at the surface of a convective mantle (Tackley, 2000b; Mallard et al., 20~~ ~~. Without such a cap, purely~~ (Tackley, 2000a; Mallard et al., 2016, e.g.). Without this type of stress limitation, strongly temperature-dependent ~~rheologies tend to~~ viscous rheologies typically produce stagnant-lid regimes (Solomatov, 1995). ~~Yield-stress parameterizations are therefore often treated as~~ In that context, yield stress is commonly interpreted as a first-order ~~proxies~~ proxy for pseudo-brittle deformation. Seismicity in oceanic lithosphere suggests that brittle failure ~~extends~~ may extend to temperatures of ~~900-1000K (e.g. Engeln et al. 1986; Abercrombie et Ekström 2001; McKenzie et al. 2005) . Accordingly, in few simulations, we restrict yielding~~ 600°C (900-1000 K) (e.g. Engeln et al., 1986; Abercrombie and Ekström, 2001; McKenzie et al., 2005). We therefore test, in a subset of simulations, cases in which yielding is restricted to temperatures below 900-950 K~~, preventing it from operating in the deeper ,~~ . This prevents yielding from operating throughout the deeper ductile lithosphere while ~~still allowing~~ retaining a pseudo-brittle response ~~near the surface.~~

in the shallow plate.

Elasticity is neglected in all simulations. Because our focus is on long-timescale viscous localization and plate-scale weakening, we expect this simplification to have limited influence on the localization trends examined here; we return to this point in the Discussion (Sect 5.2).

2.2.2 Computation of mantle effective viscosity

Diffusion creep in olivine is ~~approximated~~ represented by a temperature-dependent ~~,~~ Newtonian viscosity:

$$\eta_{\text{diff}} = A_{\text{diff}}^{-1} \cdot \exp\left(\frac{E_{\text{diff}} + P \cdot V_{\text{diff}}}{R \cdot (T + \delta T)}\right), \tag{1}$$

where A_{diff} is the pre-exponential constant, corresponding to a grain size of $\sim$3 mm (Garel et al., 2020), E_{diff} is the activation energy, V_{diff} is the activation volume, R the gas constant, P the lithostatic pressure ($\rho g z$), T the temperature, and δT a ~~term accounting~~ correction for a 0.5 K km^{-1} adiabatic gradient (Table 2).

~~Dislocation creep , which associated viscosity~~ We compare dynamic and lithostatic pressures in the Supplementary Material (Sect. S1.3.1).

Dislocation creep is non-Newtonian and ~~strain-rate dependent, is modeled using~~ strain-rate-dependent. We consider two alternative flow laws~~:~~

~~1. High-temperature~~ . First, we use conventional high-temperature (HT) ~~'~~power-law ~~'~~dislocation creep (Garel et al., 2020):

$$\eta_{\text{disl-HT}} = A_{\text{disl}}^{-\frac{1}{n}} \cdot \dot{\varepsilon}_{\text{disl}}^{\frac{1-n}{n}} \cdot \exp\left(\frac{E_{\text{disl}} + P \cdot V_{\text{disl}}}{n \cdot R \cdot (T + \delta T)}\right) \tag{2}$$

where A_{disl} is the pre-exponential constant, E_{disl} is the activation energy, V_{disl} the activation volume, n the stress exponent and $\dot{\varepsilon}_{\text{disl}}$ the second invariant of the strain-rate tensor associated with the dislocation creep ~~mechanism;~~

~~2. Unified~~ contribution. Second, we use a unified low- to high-temperature (LT-HT) dislocation creep ~~flow~~ law, derived from ~~dislocation dynamics~~ dislocation-dynamics models (Gouriet et al., 2019) and calibrated against macroscale ~~constraints on effective mantle viscosity~~ effective mantle-viscosity constraints (Garel et al., 2020):

$$\eta_{\text{disl-LT-HT}} = \frac{\sigma_{\text{disl-LT-HT}}}{2 \cdot \dot{\varepsilon}_{\text{disl}}} \tag{3}$$

with

$$\sigma_{\text{disl-LT-HT}} = A_0(T)\left(1 + \tanh\left[A_1(T)(\log_{10}(\dot{\varepsilon}_{\text{disl}}) - A_2(T))\right]\right) \tag{4}$$

where A_0, A_1, A_2 are polynomial functions of temperature (Table 2).

~~The bulk creep viscosity is then calculated assuming co-existing~~ This formulation converges to HT dislocation creep (Eq. 2) at high temperature, and predicts similar low stresses at lower temperature compared to other parameterizations Mei et al. (e.g. 2010); Demouchy et al. (e.g. 2013); Jain et al. (e.g. 2017); Warren and Hansen (e.g. 2023) (Fig. S12 in the Supplementary Material). When both diffusion and dislocation creep are present in the rheological parameterization, the bulk creep viscosity is computed assuming that the two mechanisms act in parallel:

$$\eta_{\text{creep}} = \left(\frac{1}{\eta_{\text{diff}}} + \frac{1}{\eta_{\text{disl}}}\right)^{-1} \tag{5}$$

~~with~~ and that the total strain rate ~~partitioned between the two mechanisms:~~ is partitioned between them:

$$\dot{\varepsilon}_{\cancel{\text{creep}}\,\text{II}} = \dot{\varepsilon}_{\text{diff}} + \dot{\varepsilon}_{\text{disl}} \tag{6}$$

assuming a single deviatoric stress σ

$$\sigma = 2\,\eta_{\text{creep}}\dot{\varepsilon}_{\text{II}} \quad = \quad 2\,\eta_{\text{diff}}\,\dot{\varepsilon}_{\text{diff}} \quad = \quad 2\,\eta_{\text{disl}}\,\dot{\varepsilon}_{\text{disl}} \tag{7}$$

An iterative scheme ~~ensures that η_{disl} is computed consistently~~ is used to compute η_{disl} from the dislocation creep strain rate (detailed in Supplementary Material S.1.3.2) rather than the total strain rate, thereby avoiding artificial weakening ~~(Appendix ??), and allows to compute the percentage of dislocation creep in~~ . This allows us to quantify the fraction of total creep deformation ~~(~~accommodated by dislocation creep (see Supplementary, Eq. ~~??).~~

Table 2. Variables used in the ~~different~~ rheological laws investigated in this study (Sect. 2.2).

Parameter	Symbol	Value	Unit
Diffusion creep			
pre-exponential constant	A_{diff}	1. 10^{-7}	Pa s
Activation energy	E_{diff}	410	kJ mol^{-1}
Activation ~~energy~~ volume	V_{diff}	4. 10^{-6}	m^3 mol^{-1}
HT dislocation creep			
pre-exponential constant	A_{disl}	4.4 10^{-17}	Pa s
Activation energy	E_{disl}	540	kJ mol^{-1}
Activation ~~energy~~ volume	V_{disl}	6. 10^{-6}	m^3 mol^{-1}
stress exponent	n	3.5	
LT-HT dislocation creep (*tanh*)			
A_0 = 4.4 10^8 - 5.26 10^4 T			
A_1 = 2.11 10^{-2} + 1.74 10^{-4} T			
A_2 = -41.8 + 4.21 10^{-2} T - 1.14 10^{-5} T^2			

S13).

The pseudo-brittle contribution is ~~introduced via~~ represented by a non-Newtonian ~~yield-stress~~ yield viscosity:

$$\eta_{\text{yield}} = \frac{\sigma_y}{2 \cdot \dot{\varepsilon}_{\text{II}}} \tag{8}$$

where σ_y is a constant yield stress (200-500 MPa ~~in different simulations~~depending on the simulation) and $\dot{\varepsilon}_{II}$ the ~~strain rate second invariant .~~

second invariant of the strain-rate tensor. The effective viscosity used in the momentum equation is then taken as the minimum of creep and yield viscosities:

$$\eta = \min(\eta_{\text{creep}}, \eta_{\text{yield}}). \tag{9}$$

Numerical stability is maintained by ~~applying~~ imposing viscosity cutoffs of 10^{18} and 10^{25} Pa s. At each ~~location in the domain, the dominant mechanism is tracked (yield vs.~~ point, we also identify the dominant deformation mechanism: yielding versus creep, and within creep, diffusion ~~vs. dislocation, for the one contributing to~~ versus dislocation, based on the creep mechanism contributing $\geq$50% ~~to~~ of the total strain rate.

2.2.3 Strategy ~~to investigate~~ for investigating rheological control on lithospheric extension~~in numerical experiments~~

~~We investigate in various simulations different combinations of rheologies presented in the previous section, which are listed in~~ We investigate a suite of rheological combinations (Table 3):

- ~~a purely Newtonian diffusion-creep viscosity~~ Diffusion creep only (D),
- ~~combinations of diffusion and either a~~ Diffusion creep combined with either HT or a LT-HT dislocation creep (~~$D-d_{\text{(LT-)HT}}$~~ $D-d_{\text{HT}}$ or $D-d_{\text{LT-HT}}$),
- ~~combinations of diffusion creep and~~ Diffusion creep combined with a yield-stress rheology ($D-Y_{200/500\ \text{MPa}}$),
- ~~combinations of diffusion and dislocation~~ Diffusion creep, dislocation creep, and yield-stress ~~rheology ($D-d_{\text{(LT-)HT}}-Y_{200/500\ \text{MPa}}$~~ con ($D-d_{\text{HT}}$ or LT-HT $-Y_{200/500\ \text{MPa}}$).

The two constant yield ~~stress values at~~ stresses, 200 and 500 MPa~~are chosen as either a representative value reproducing plate tectonics in numerical models of mantle convection ((Mallard et al., 2016, e.g.), or the upper bound for the validity of~~ , are chosen to span the range between values commonly used to generate plate-like behaviour in mantle convection models (Mallard et al., 2016, e.g.), and the upper stress range over which the LT-HT dislocation creep ~~(Gouriet et al., 2019; Garel et al., 2020), respectively. The simulation domain where yielding is allowed is in some simulations explicitly~~ formulation is calibrated (Gouriet et al., 2019; Garel et al., 2020). In a subset of simulations, yielding is restricted to the expected brittle domain ~~, here to temperatures~~ (see Sect. 5.1), by allowing it only below 900 or 950 K (~~$Y^{950\ \text{K}}_{200/500\ \text{MPa}}$ or $Y^{900\ \text{K}}_{200/500\ \text{MPa}}$).~~

~~These combinations feature different co-dependencies of the mantle viscosity on temperature and strain rate, with a transition from yield-stress~~ $Y^{950\ \text{K}}_{200\ \text{or}\ 500\ \text{MPa}}$ or $Y^{900\ \text{K}}_{200\ \text{or}\ 500\ \text{MPa}}$). These rheological combinations differ in both their strain-rate and temperature dependence, and in the depth and temperature at which deformation transitions from yield-dominated to creep-dominated ~~rheologies at different temperatures/depths. This will allow to explore different depth-distributions of deformation mechanisms: the associated feedbacks — between intraplate strain localization(increase in strain rate) and asthenosphere upwelling(increase in temperature) — are expected to lead to various scenarios and timing of lithosphere~~ behaviour. They therefore provide a controlled way to test how the depth distribution of weakening influences localization, asthenospheric upwelling, and the timing of lithospheric break-up under ~~a~~ constant extension velocity.

2.3 Numerical methods

We solve the conservation equations of mass, momentum and energy for an incompressible Stokes fluid under the Boussinesq approximation using the finite-element, control-volume ~~framework~~ code *Fluidity* (e.g., Davies et al., 2011). This ~~approach~~ framework has been widely ~~applied in geodynamical studies, and has been~~ used in geodynamical applications and extensively benchmarked against analytical and numerical reference solutions ~~.~~

~~The governing~~ (e.g. Le Voci et al., 2014; Garel et al., 2014; Kramer et al., 2021b; Duvernay et al., 2022). The equations are discretized on an unstructured Eulerian mesh ~~, which~~ that is dynamically adapted throughout ~~the simulations. Mesh refinement~~ each simulation. Refinement criteria are applied ~~simultaneously~~ to temperature, velocity, strain-rate, and viscosity~~fields, ensuring that sharp gradients such as lithospheric thermal boundaries, strain~~ , ensuring adequate resolution of lithospheric thermal gradients, localization zones, and ~~viscosity contrasts are adequately resolved.~~

~~The triangular element size varies between 500 m and~~ strong viscosity contrasts. Triangular element sizes range from 200-1000 m in the finest regions to 50 km ~~across the domain~~in the coarsest regions, with the highest resolution concentrated in the lithosphere and regions of active deformation (~~Fig. S1~~ Sect. S.1.1 in the Supplementary ~~material~~Material). A typical simulation ~~employs~~ contains approximately 50,000 nodes, although this ~~number varies depending on the minimum element size and adaptivity criteria.~~

varies as simulations evolve.

3 Post-processing diagnostics

~~In the following~~For post-processing, physical fields are interpolated from the ~~finite-element unstructured~~ unstructured finite-element mesh onto a regular grid with 5×1 km^2 ~~regular grid to compute spatial averages or Eulerian time-derivatives. Simulations are post-processed by calculating several diagnostics (detailed hereafter) to unravel and locate the various processes leading to plate break-up: co-evolution of spatial strain localization, plate thinning and weakening, and the causes of the latter.The lithosphere is defined here~~ spacing. This allows consistent calculation of spatial averages and Eulerian time derivatives. We define the lithosphere as the region colder than 1500 K. ~~This threshold is~~ In this single-material model, that threshold provides a first-order proxy ~~, since the unique mantle material leads to a gradual transitionfrom lithosphere to asthenosphere for~~ for the lithosphere-asthenosphere transition, which is otherwise gradual in temperature, deformation and velocity (Garel and Thoraval, 2021). We also ~~focus on the deepest region of the lithospheric plate between 900~~ pay particular attention to the deeper lithospheric interval between 800 and 1500 K~~.~~

, where the yield-creep transition and the majority of the weakening occur. Some diagnostics are vertically-averaged over the ~~whole lithosphere with the notation~~ lithosphere and denoted $\langle X \rangle_{1500\ \mathrm{K}}(x,t)$, ~~with~~ using either an arithmetic or ~~a~~ geometric mean depending on the range spanned by X ~~parameter span.~~

~~Finally, to allow comparison of simulations featuring different extension velocities~~ . To compare simulations with different extension rates $v_{1/2}$, ~~a global average strain is estimated as~~ we define a bulk extensional strain $\varepsilon(t) = \frac{2\cdot t\cdot v_{1/2}}{L}$ where t is ~~the~~ time and L is the domain width. All simulations are ~~conducted up~~ run to ~40 % ~~strain (~~bulk strain, corresponding to ~500 km cumulative horizontal ~~plate extension).~~

extension.

3.1 ~~Intraplate strain~~ Strain localization in the lithospheric mantle

~~Intraplate strain localization is first quantified using the strain rate~~ We first quantify strain localization within the plate using the strain-rate amplification $A_{\mathrm{SR}}(x,z,t)$ relative to the ~~initially-uniform intraplate strain rate~~ initially uniform strain rate in the plate $\dot{\varepsilon}_{t_0}$ (Fig. 2), and its ~~average (geometric mean) over the whole lithosphere~~ geometric mean over lithospheric thickness at each horizontal position.

~~To quantify how plate deformation spatially focuses~~ To track lateral focusing through time, we ~~track the width $w(t)$ of the intraplate deformed zone~~define the width of the deforming zone, $w(t)$, as the region where $\langle A_{\mathrm{SR}} \rangle_{1500\ \mathrm{K}}(x,t) > 1$~~, and calculate~~. From this, we compute a narrowing rate~~in the first stage of deformation (see Sect. 4.2)~~. We also quantify ~~an intraplate~~ the lateral viscosity contrast within the plate $R_{\mathrm{visc}}(t)$, as the ratio between the maximum vertically-averaged lithospheric viscosity along x ~~(geometric mean)~~ and the minimum ~~one (~~value in the central weak zone~~)~~:

$$R_{\mathrm{visc}}(t) = \frac{\max\left(\langle \eta \rangle_{1500\ \mathrm{K}}(x,t)\right)}{\min\left(\langle \eta \rangle_{1500\ \mathrm{K}}(x,t)\right)} \tag{10}$$

Finally, we compute ~~at each time~~ the *plateness* $P(t)$ ~~(Tackley, 2000b; Crameri, 2018; Fuchs and Becker, 2019), defined as one minus the relative width concentrating 80 % of the total cumulative strain rate (details of the *plateness* calculation are provided~~ (Tackley, 2000a; Crameri, 2018). Details of the calculation are given in the Supplementary material ~~and references therein).~~

(Sect. S.1.4.1).

3.2 Plate thinning, weakening, and bulk stiffness

~~Plate extension sets off a central thinning, and we compute the lithosphere~~ To quantify lithospheric thinning, we define the plate thickness $h_{\mathrm{plate}}(t)$ as the minimum depth of the 1500 K isotherm along x~~, from which we calculate~~. Its time evolution is used to estimate an upwelling rate~~in the second stage of deformation (see Sect. 4.2).~~

~~We track the increase or decrease of intraplate effective viscosity with the weakening rate $W(x,z,t)$ (in s^{-1}), time-derivative of the logarithm of the effective viscosity~~~~η~~. We track time-dependent weakening or hardening through the logarithmic rate of change in effective viscosity:

$$W(x,z,t) = -\frac{\partial \log_{10}(\eta)}{\partial t} \approx -\frac{1}{\Delta t}\log_{10}\left(\frac{\eta_{t+\Delta t}}{\eta_t}\right) \tag{11}$$

where Δt ~~(~~is chosen to be much smaller than the localization timescale (typically 0.05-1 Myr, ~~adjusted to the extension velocity)is a time increment much smaller than the localization timescale. We verify that a smaller~~ depending on extension rate). Smaller values of Δt ~~does~~ do not change the weakening amplitude. ~~Positive (resp. negative)~~ Positive values of W indicate ~~plate weakening (resp. hardening).~~weakening whereas negative values indicate hardening.

We also compute the ~~weakening rate averaged over the lithosphere~~ vertically averaged weakening rate $\langle W \rangle_{1500\ \mathrm{K}}(x,t)$ ~~(geometric mean)~~using a geometric mean. A 10-fold decrease in viscosity in 1 Myr corresponds to a weakening rate W of about 3 10^{-14} s^{-1}.

~~We quantify a bulk lithosphere strengthin 2-D as~~ As a bulk measure of lithospheric strength, we calculate the tectonic force $F(t)$ (in N m^{-1}) required to ~~sustain constant~~ maintain the imposed extension velocity at the side boundaries ~~(Bialas et al., 2010; Brune et al.~~

(Bialas et al., 2010; Brune et al., 2012):

$$F(t) \quad = \quad H \cdot \sqrt{(S_{xx} - S_{zz})^2 + S_{xz}^2} \tag{12}$$

$$\text{with} \quad S_{ij}(t) \quad = \quad \frac{1}{H} \int_0^{\mathrm{H}} \sigma_{ij}(z,t)dz \tag{13}$$

where S_{ij} is the stress tensor vertically averaged over the ~~whole~~ full domain height H ~~from local stress tensor σ_{ij} at horizontal position $x = 100$ km.~~

at $x = 100$ km, to minimize boundary effects (see Supplementary Material S1.4.2).

3.3 Physical controls on plate weakening

~~Montési and Zuber (2002) addressed the issue of strain localizationpotential related to rheology parameterization, featuring multiple dependencies on variables being either material properties (e.g., grain size, damage) or physical states (e.g. temperature , strain rate), by defining an effective stress exponent (their eq. 2). Their approach inspired us to calculate time derivatives of viscosity , which in our study depends solely on temperature and strain rate, to discriminate and quantify thermal and mechanical contributions to weakening.~~

~~At each position of the interpolated regular grid, the time-derivative of viscosity can be decomposed as the sum of its partial derivatives, with respect to temperature and strain rate:~~

$$\frac{\partial\eta(T,\dot\varepsilon)}{\partial t} = \frac{\partial\eta}{\partial T}\frac{\partial T}{\partial t} + \frac{\partial\eta}{\partial\dot\varepsilon}\frac{\partial\dot\varepsilon}{\partial t}$$

~~which is approximated, by calculating the viscosity η as depending on temperature $T(x,z,t)$~~ To distinguish why viscosity decreases during localization, we partition weakening into contributions associated with temperature and strain-rate changes. This builds on the general idea that localization potential can be related to the sensitivity of viscosity to evolving state variables (Montési and Zuber, 2002). At each point on the interpolated grid, viscosity depends only on temperature and strain rate~~$\dot\varepsilon(x,z,t)$ at each location, as:~~ , so its time derivative may be written as:

$$\frac{\Delta\eta}{\Delta t}\frac{\partial\eta(T,\dot\varepsilon)}{\partial t} = \frac{\Delta\eta}{\Delta t}\Big|_{\dot\varepsilon}\frac{\partial\eta}{\partial T}\frac{\partial T}{\partial t} + \frac{\Delta\eta}{\Delta t}\Big|_{T}\text{~~with~~}\frac{\partial\eta}{\partial\dot\varepsilon}\frac{\partial\dot\varepsilon}{\partial t} \tag{14}$$

~~We can now quantify the relative contributions to material weakening~~ We approximate this decomposition over a finite time interval Δt as:

$$\frac{\Delta\eta}{\Delta t} = \frac{\Delta\eta}{\Delta t}\Big|_{\dot\varepsilon} + \frac{\Delta\eta}{\Delta t}\Big|_{T} \begin{cases} \left.\dfrac{\Delta\eta}{\Delta t}\right|_{\dot\varepsilon} = \dfrac{\eta\big(T(x,z,t+\Delta t),\,\dot\varepsilon(x,z,t)\big) - \eta\big(T(x,z,t),\,\dot\varepsilon(x,z,t)\big)}{\Delta t} \\ \left.\dfrac{\Delta\eta}{\Delta t}\right|_{T} = \dfrac{\eta\big(T(x,z,t),\dot\varepsilon(x,z,t+\Delta t)\big) - \eta\big(T(x,z,t),\,\dot\varepsilon(x,z,t)\big)}{\Delta t} \end{cases} \tag{15}$$

The corresponding normalized contributions to weakening are then

$$F_\mathrm{T} = \frac{\left.\frac{\Delta\eta}{\Delta t}\right|_{\dot{\varepsilon}}}{\frac{\Delta\eta}{\Delta t}} \qquad \text{and} \qquad F_\mathrm{SR} = \frac{\left.\frac{\Delta\eta}{\Delta t}\right|_{T}}{\frac{\Delta\eta}{\Delta t}} \tag{16}$$

where F_T ~~and F_SR, caused respectively by the increase in temperature~~ measures the contribution from temperature evolution ('thermal' weakening) ~~or in strain rate~~ and F_SR, the contribution from strain-rate evolution ('mechanical' weakening)~~:~~

$$F_\mathrm{T} = \frac{\left.\frac{\Delta\eta}{\Delta t}\right|_{\dot{\varepsilon}}}{\frac{\Delta\eta}{\Delta t}} \qquad \text{and} \qquad F_\mathrm{SR} = \frac{\left.\frac{\Delta\eta}{\Delta t}\right|_{T}}{\frac{\Delta\eta}{\Delta t}} \qquad \text{with} \qquad F_\mathrm{T} + F_\mathrm{SR} = 100\%$$

~~A smaller time increment Δt may cause~~. We use $\Delta t \approx 0.25$ Myr for this partitioning. Smaller values introduce short-period oscillations in ~~the calculated~~ F_T and F_SR ~~.~~

without changing the broader trends. These diagnostics are evaluated only where the material is undergoing weakening ($W > 0$). Mixed cases can nevertheless arise, for example when mechanical weakening due to strain-rate increase exceeds thermal hardening due to plate cooling. In such cases, F_T may become negative and F_SR may exceed 1 (as discussed in Sect. 4.4). For plotting purposes, the colour scale for F_SR is capped between 0 and 1.

4 Results

4.1 ~~Diffuse vs. localized deformation during lithospheric extension~~

~~In Sect. 4.1, 4.2 and 4.3, we first perform simulations of an initially 50 Myrs-old lithosphere extended under a half spreading rate of $v_{1/2} = 1$ cm yr^{-1}. The initial intraplate strain rate is quasi-homogeneous throughout the whole lithosphere: $\dot{\varepsilon}_{t_0}$ ~3.73 10^{-16} s^{-1} (Fig. 2). Depending on the rheological parameterization (Table 3), we observe two end-members of intraplate deformation pattern for the final state ($\varepsilon \sim 40$ %) : either two distinct plates separated by a localized, narrow highly deformed zone, located above an asthenosphere upwelling ("localized plate boundary" Table 3), or a single plate displaying a spatially-diffuse,~~ We present our results in four steps. First, we describe the range of deformation patterns obtained for a reference plate age (50 Myr) and ~~relatively homogeneous deformation ("distributed deformation" in Table 3).~~ half-extension rate ($v_{1/2}$ =1 cm yr^{-1}), from distributed deformation to localization into a narrow extensional boundary. Second, we use a representative localizing case to define characteristic times and a two-stage evolution of localization based on the co-evolution of deforming-zone width and plate thickness. Third, we compare rheological parameterizations to explain the differences in localization efficiency and in the depth/temperature range over which weakening occurs. Fourth, we explore sensitivity to initial plate age and imposed extension rate.

~~Two simulations representative of these end-members are shown in~~

4.1 Diffuse vs. localized deformation during lithospheric extension

For an initially 50-Myr-old plate extended at $v_{1/2} = 1$ cm yr^{-1}, the rheological parameterization produces three distinct deformation outcomes by 40% bulk strain (Table 3, Fig. 3~~. The non-localizing simulation *ref-0* (rheology $D - d_{\mathrm{HT}}$, Table 2 and~~ , Fig. ~~3a) exhibits a long-lasting and steady intraplate deformation. This diffuse deformation mode corresponds to a slow plate thinning (∼0.05 cm yr^{-1}), arising from the competition between thickening by diffusive cooling and lithosphere extension~~A1). First, Simulation ***ref-1*** ~~will be used~~ serves as a reference for the strain localization scenario (Table 3, and Fig. 3b). Its rheology, labeled $D - d_{\text{LT-HT}} - Y_{500\ \mathrm{MPa}}$, accounts for diffusion creep, low- and high-temperature dislocation creep (eq. 3) and a yield stress of 500 MPa (eq. 8). This simulation shows a progressive narrowing of the ~~highly~~ enchanced deformed domain around the box center, where most of the deformation is accommodated as shown by the significant increase in the horizontal velocity gradient at the surface (Fig. 3b, 1-6 Myr). In a second stage, ~~a significant asthenosphere upwelling develops under~~ significant asthenospheric upwelling develops beneath the most stretched lithosphere portion, resulting in a boundary separating two divergent plates that behaves as a horizontal velocity discontinuity (Fig. 3b, 12 Myr). Hence, in localizing cases, a narrow extensional plate boundary develops at the domain center, separating two rigid plates (Simulation *ref-1* in Fig. 3b). These runs exhibit high plateness ($P > 0.95$), a large lateral viscosity contrast ($R_{\mathrm{visc}} > 100$), and a deformed-zone width $w < 100$ km, while plate thickness h_{plate} approaches a quasi-steady value after localization. The localized zone is underlain by focused asthenospheric upwelling.

~~In some experiments, we observe an intermediate scenario~~ Second, the non-localizing simulation *ref-0* (rheology $D - d_{\mathrm{HT}}$, Table 2 and Fig. 3a) exhibits a long-lasting and steady plate deformation. This diffuse deformation mode corresponds to a slow plate thinning (∼0.05 cm yr^{-1}), arising from the competition between thickening by diffusive cooling and lithosphere extension. In such cases where deformation is always distributed, the plate deforms broadly and remains laterally uniform, without any increase in the horizontal velocity gradient at the surface (e.g., Simulation *ref-0* in Fig. 3a). These runs show low plateness ($P < 0.3$) and weak lateral viscosity contrast ($R_{\mathrm{visc}} < 10$). Strain-rate amplification remains modest across the plate and deformation is expressed primarily as gradual, laterally uniform thinning.

Third, an intermediate regime occurs in which the deformation localization is very slow ~~. These simulations, labeled "incomplete localization" in Table 3 do not achieve fully localized deformation: the highly deformed zone remains larger than 150 km~~ (Appendix A). Strain begins to focus but the area where deformation is enhanced remains relatively wide at 40~~% strain , similarly to Fig~~% strain (incomplete localization). These runs still exhibit narrowing of the deformed zone and plate thinning, with $w \gtrsim 150$ km at the end of the simulations, comparable to the early-to-intermediate state of Simulation *ref-1* (e.g., Fig. 3b at 6 ~~Myr.~~

Myr).

In the remainder of the Results, we use a representative localizing simulation (*ref-1*) to define a reference localization trajectory and characteristic timescales, and then compare rheological combinations and forcing parameters against that trajectory.

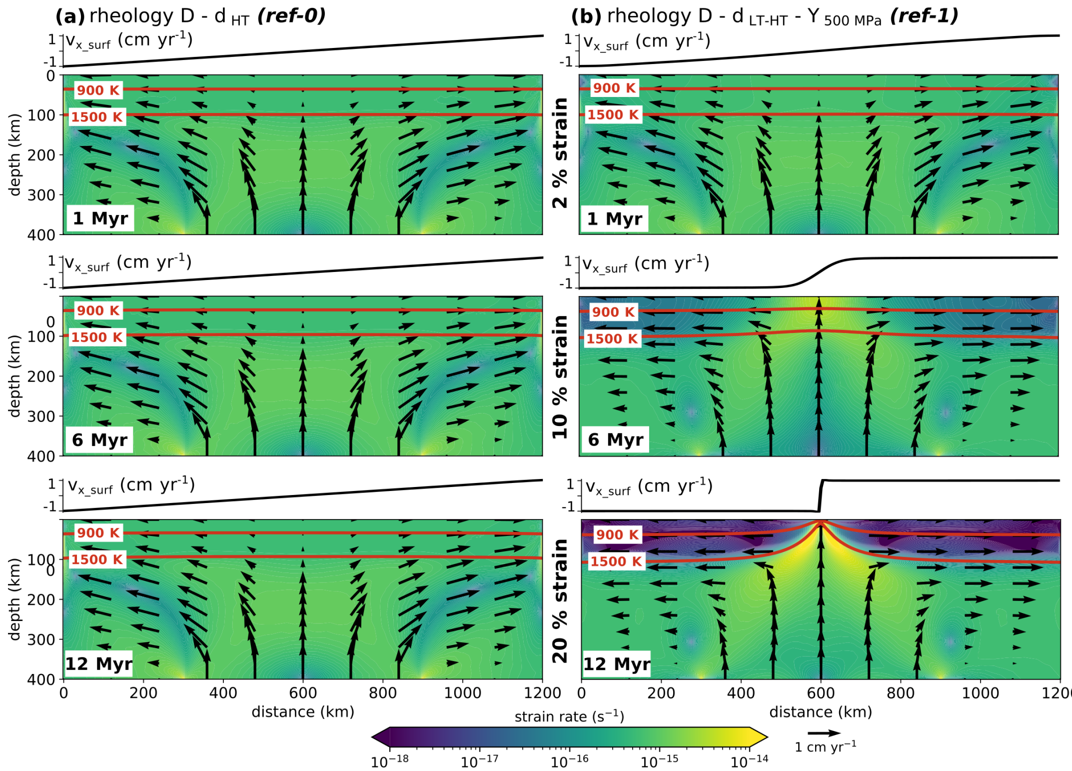

Figure 3. Evolution of the strain rate field (second invariant) during two end-member simulations, shown after 1 Myr, 6 Myr and 12 Myr of extension: (a) Simulation ~~$D-d_{HT}$~~ $D-d_{HT}$ (*ref-0*~~:~~), with diffusion creep and high-temperature dislocation creep, Table 3 ~~) showing mainly a homogeneous~~ characterized by uniform and diffuse lithospheric thinning; (b) Simulation ~~$D-d_{LT\text{-}HT}-Y_{500\,MPa}$~~ $D-d_{LT\text{-}HT}-Y_{500\,MPa}$ (*ref-1*), combining diffusion creep, low- and high-temperature dislocation ~~creeps~~creep, and a yield-stress set to 500 MPa~~)~~, which successfully ~~localizing intraplate~~ localizes plate deformation. ~~The~~ For each snapshot, the horizontal velocity at the surface is plotted above. Velocity field is depicted by black arrows, and the 900 K and 1500 K isotherms are ~~outlined~~ indicated in red.

4.2 A two-stage scenario of strain localization and lithosphere weakening

~~The spatial localization of deformation~~ We quantify the localization trajectory in Simulation *ref-1* ~~is illustrated using a distance-time representation of~~ using the ~~vertically-averaged strain rate amplification $\langle A_{SR}\rangle_{1500\,K}(x,t)$ (see~~ co-evolution of deformed-zone width w, the minimum plate thickness h_{plate}, and the weakening rate W (Sect. ~~3.1) in~~ 3). The deforming region (defined by $\langle A_{SR}\rangle_{1500\,K} > 1$, Sect. 3.1) progressively narrows toward the domain center (Fig. 4a~~and of the vertically-averaged weakening rate $\langle W\rangle_{1500\,K}(x,t)$ in~~), while weakening intensifies within the lithosphere beneath the developing boundary (Fig. 4b ~~. The more deformed region ($\langle A_{SR}\rangle_{1500\,K} > 1$)narrows with time, while , simultaneously, the weakening rate increases in the vicinity of the box center. The evolution through time of the weakening rate $W(z,t)$, computed for two vertical profiles at $x = 300$ km and at the box center $x = 600$ km are displayed in Fig. 4c and d, respectively.~~

and d).

The localization trajectory is well described by two stages (Fig. 5a). Stage 1 is dominated by lateral focusing of deformation: w decreases rapidly whereas h_{plate} decreases only modestly. Stage 2 is dominated by rapid plate thinning driven by asthenospheric upwelling: h_{plate} decreases rapidly while the narrowing of w slows down. Stages 1 and 2 are detailed below. We define two ~~successive stages to describe the process of deformation localization within the mantle lithosphere:Stage~~ characteristic times. The transition time t_{tr} marks a shift in trajectory in $h_{\mathrm{plate}}(t)$:$w(t)$ space (Appendix B); it coincides with the end of the approximately steady tectonic force plateau F (Fig. 6c). The plate-boundary time t_{PB} marks the onset of a quasi-steady geometry, when both h_{plate} and w become approximately stationary and the tectonic force has dropped to its post-localization value (Fig. 6c).

For Simulation *ref-1*, Stage 1 ~~, spatial focusing of the deformed zone (0-6.5 Myr): the width w of the highly deformed zone rapidly decreases with a narrowing rate up to 14 cm yr^{-1}, while the central plate thinning rate (upwelling rate of the 1500 K isotherm)is low, around 0.3 cm yr^{-1} (lithosphere thin from~~ lasts 6.5 Myr and is characterized by rapid narrowing (mean 14 cmyr^{-1}) with limited thinning (100 to 82 km ~~during stage 1, Fig.~~ in Fig.5a). ~~The weakening rate at the plate center is roughly homogeneous throughout the whole~~ During this stage, weakening at the domain center is distributed through much of the lithosphere thickness (Fig. 4d) ~~, and larger than the~~ and exceeds off-center weakening ~~rate~~ (Fig. 4c)~~. As a consequence, there is a small lateral~~ , producing a growing but moderate viscosity contrast (~~$R_{\mathrm{visc}} < 50$)between the weaker (and weakening) central region and the stiffer (and hardening)plate outskirts~~ $R_{\mathrm{visc}} < 50$; Fig.5b). In the plate interior outside the deforming zone, viscosity increases (hardening), particularly toward the end of Stage 1 (Fig. ~~5~~4b).

Stage 2 ~~, plate thinning associated with an asthenosphere upwelling (~~lasts 5.5 Myr (from 6.5 ~~-12~~to 12 Myr) ~~: the central deformed zone narrows more slowly (narrowing rate around 4 cm yr^{-1}), while the upwelling rate is almost 5 times faster than in Stage 1 (lithosphere thin from~~ and is characterized by rapid thinning (82 to 10 km~~during stage 2, Fig.~~) and a sharp reduction in tectonic force, whereas narrowing is slower (mean ~ 4 cm yr^{-1}; Fig.5a). ~~We define the transition time t_{tr} between Stage 1 and Stage 2 from the co-evolution of w and h_{plate} (see Appendix B): over about 2 Myr the upwelling progressively accelerates while the narrowing decelerates and the off-center plate hardens rapidly~~ Weakening peaks shortly before t_{PB} (Fig. ~~4band c). The~~ 5b), while the lateral viscosity contrast ~~increases up to 2000~~ continues to increase and reaches its maximum near t_{PB} (Fig. 5b). ~~During Stage 2, the central weakening is the highest for temperatures higher than 800 K, which corresponds to the plate region dominantly deforming by dislocation creep~~ After t_{PB}, the system evolves toward a steady thermal structure around the mature boundary and the weakening rate in the narrow boundary region approaches zero (Fig. 4~~d and Fig 8a).Outside the deforming central region, the plate viscosity is rather steady ($W \sim 0$).~~

b).

~~The end of~~

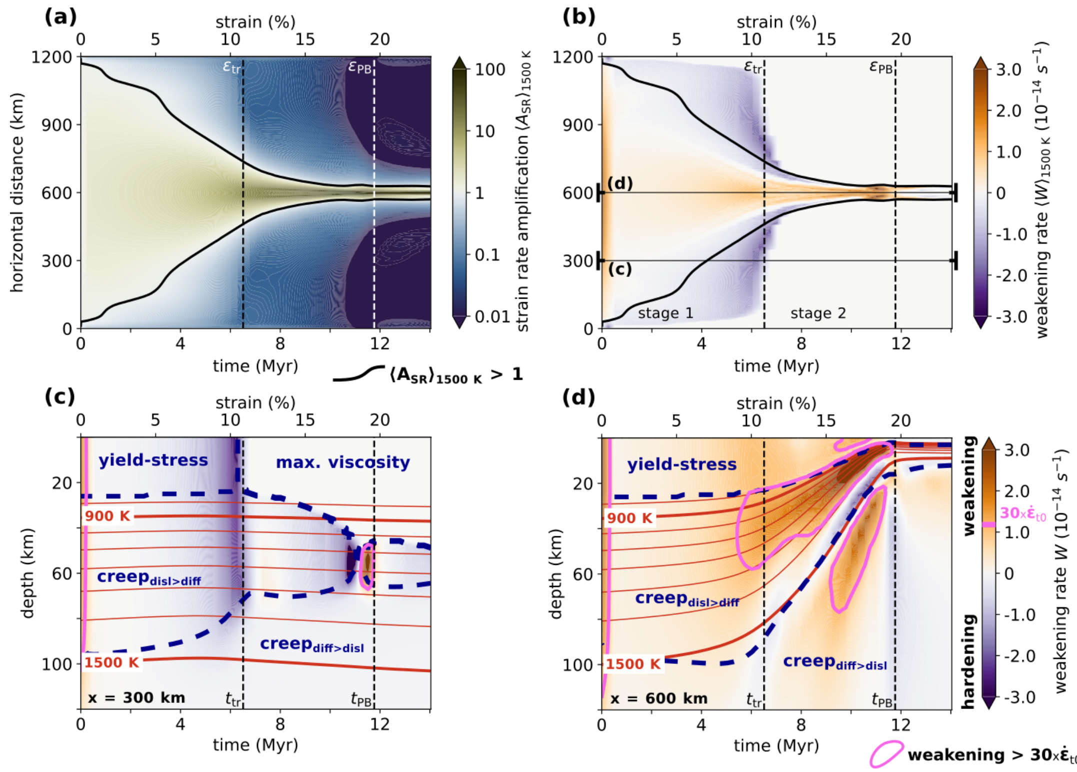

~~Lithospheric deformation localization and weakening in Simulation $D - d_{\text{LT-HT}} - Y_{500\,\text{MPa}}$ (*ref-1*, Table 3). (a) Time-space evolution of the strain-rate amplification $\langle A_{\text{SR}}\rangle_{1500\text{ K}}(x,t)$, computed as the vertically-averaged ratio relative to the initial homogeneous strain rate in the plate (here $\dot{\varepsilon}_{t_0}$ ~3.73 10^{-16} s^{-1}, see Sect. 3.1). Along the black thick line, this ratio is equal to 1. (b): Time-distance plot of the geometric mean of the vertically-averaged weakening rate $\langle W\rangle_{1500\text{ K}}(x,t)$ (Sect. 3.2). We represent only values where >60 % (resp. <40 %) of the lithosphere thickness is in weakening, averaging only the weakening values for which $W > 0$ (resp. hardening values $W \leq 0$). (c), (d) Depth-time evolution of the weakening rate W at x =300 km (c) or 600 km (d). The pink outline corresponds to a high weakening zone where $\frac{W}{\dot{\varepsilon}_{t_0}} > 30$, the red lines depict the isotherms from 800 to 1500 K. Regions with different dominant deformation mechanisms are delimited by dashed dark blue contours. In all panels, the vertical dashed lines indicate the transition time, t_{tr} and the plate boundary time, t_{PB}.~~

Figure 4. Localization of lithospheric deformation and weakening in Simulation $D - d_{\text{LT-HT}} - Y_{500\,\text{MPa}}$ (*ref-1*, Table 3). (a) Time-distance evolution of strain-rate amplification $\langle A_{\text{SR}}\rangle_{1500\text{ K}}(x,t)$, calculated as the vertically-averaged ratio relative to the initial uniform strain rate in the plate (here $\dot{\varepsilon}_{t_0}$ ~3.73 10^{-16} s^{-1}, see Sect. 3.1). The thick black line features the isocontour 1 of this ratio. (b) Time-distance plot of the geometric mean of the vertically-averaged weakening rate $\langle W\rangle_{1500\text{ K}}(x,t)$ (Sect. 3.2). Orange shades indicate where weakening ($W > 0$) affects more than 60 % of lithospheric thickness, with plotted values representing the geometric mean at a given x and time t over all depths z where $W(x,z,t) > 0$. On the other hand, purple-blue shades indicate where weakening affects less than 40 % of lithospheric thickness, plotting the vertical geometric mean for depths where $W \leq 0$ (hardening or neutral). Areas where weakening affects between 40 % and 60 % of the lithospheric thickness are left white. (c), (d) Depth-time evolution of the weakening rate W at $x = 300$ km (c) and 600 km (d). The pink outline highlights zones of high weakening where $\frac{W}{\dot{\varepsilon}_{t_0}} > 30$, and the red lines indicate isotherms from 800 to 1500 K. Regions with different dominant deformation mechanisms are delineated by dashed dark-blue contours. In all panels, vertical dashed lines indicate the transition time, t_{tr} and the plate boundary time, t_{PB}.

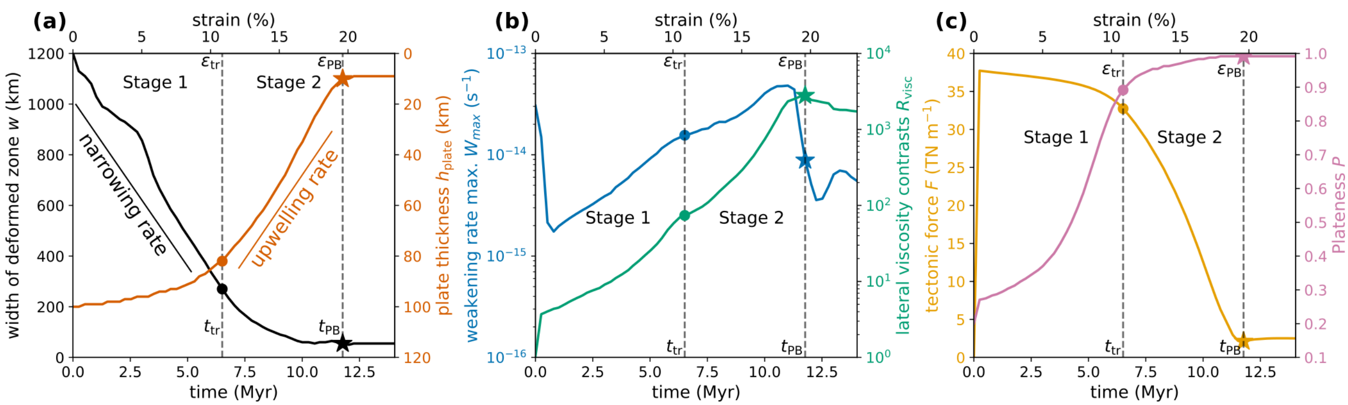

Figure 5. Results for Simulation $D - d_{LT-HT} - Y_{500\,\mathrm{MPa}}$, *ref-1*. (a) Temporal evolution (and corresponding cumulative strain in %) of the width of deformed zone w (black) and minimum lithosphere thickness (orange) as defined in Sect. 3.1. Average narrowing and upwelling rates are calculated for Stage 1 and Stage 2, respectively. Rates can be expressed in km Myr^{-1} or in cm yr^{-1} (where 1 cm yr^{-1} = 10 km Myr^{-1}). Temporal evolution (and corresponding cumulative strain in %) of (b) the maximum weakening rate (blue) within the lithosphere, defined as the region between the 273 and 1500 K isotherms- at $x = 600$ km (eq. 11), and plate lateral viscosity contrast (green) R_{visc} (eq. 10), and (c) tectonic force (yellow) and plateness (pink). In all panels, vertical dashed lines indicate the transition time, t_{tr} and the plate boundary time, t_{PB}, also displayed on the curves by dots (for t_{tr}) and stars (for t_{PB}).

4.3 Influence of rheological parameterization on localization scenario

Across all rheological combinations, simulations that localize deformation follow the same two-stage trajectory defined in Sect. 4.2 (Fig. 7). Stage 1 is dominated by progressive narrowing of the deforming zone with only modest thinning, whereas Stage 2 is ~~defined as the time t_{PB} when the central upwelling becomes stationary (here 12 Myr,~~ dominated by rapid plate thinning associated with focused asthenospheric upwelling and only limited additional narrowing (Fig. ~~5a), even if the plate boundary widens slightly after this time (lateral shifting of isotherms and late off-center weakening visible~~ 6a–b). The major rheological control is therefore whether deformation localization occurs and how quickly the system progresses through the two stages, rather than the geometrical trajectory or the maximum weakening rate (10^{-13} s^{-1} for all simulations in Fig. ~~4c).The lateral viscosity contrast remains stable, with a weak plate boundary located in-between quasi-non-deforming plates (~~6f).

In simulations without a yield-stress cap, deformation remains distributed regardless of whether diffusion creep is combined with high-temperature dislocation creep or with low- to high-temperature dislocation creep (e.g., Simulation *ref-0*; Fig. 3~~b). Note that there is almost no plate weakening, neither hardening, at the box center once the boundary formation is completed (Fig. 5b)~~ a). Thus, in this lithospheric extension setup, dislocation and diffusion creep alone are insufficient to generate lithospheric-scale localization; additional weakening of the cold upper lithosphere (here provided by a yield-stress cap) is required.

Among simulations that do localize strain, the characteristic times vary substantially between rheologies (Table 3).

~~Simulation $D-d_{LT-HT}-Y_{500\,\mathrm{MPa}}$, *ref-1*. (a) Time evolution of the width of deformed zone w (black) and minimum lithosphere thickness (red) as defined in Sect. 3.1. An average narrowing (resp. upwelling) rate is computed over Stage 1 (resp. Stage 2). These rates can be expressed in km Myr^{-1} or in cm yr^{-1} (i.e. 1 cm yr^{-1} = 10 km Myr^{-1}). (b) Maximum value, over the lithosphere thickness encompassed between the 273 and 1500 K isotherms, of the weakening rate at x =600 km as a function of time (eq. 11) in blue, and intraplate lateral viscosity contrast R_{visc} (eq. 10) in green .~~

~~The relative contributions of temperature (F_{T}) and strainrate (F_{SR}) to material weakening (Eq. 16)are computed over time and depth at the box center. (x = 600 km) in Figure 8a, with (i) superimposed boundaries (in dashed dark blue) delimiting the dominant deformation mechanism defined in Sect. 2.2.2, and (ii)a 'highly weakening' zone (weakening rate normalized by the initial intraplate strain rate $\frac{W}{\dot{\varepsilon}_{t_0}} > 30$, in pink contour~~ Localization takes about twice as long for diffusion creep plus yield stress (e.g., $D-Y_{200\,\mathrm{MPa}}$ and $D-Y_{500\,\mathrm{MPa}}$) and for cases in which yielding is restricted to temperatures below 950 K (e.g., $D-d_{\mathrm{HT}}-Y^{950\,\mathrm{K}}_{500\,\mathrm{MPa}}$), than for rheologies that combine diffusion creep, dislocation creep, and yield stress (e.g., $D-d_{\mathrm{HT}}-Y_{200/500\,\mathrm{MPa}}$ and $D-d_{\mathrm{LT\text{-}HT}}-Y_{200/500\,\mathrm{MPa}}$; Fig. ~~8a).~~

~~The upper part of the lithosphere is dominated by yielding, while the plate base deforms mainly in the dislocation creep regime and the underlying asthenosphere ($T > 1500$ K)deforms mainly by diffusion creep~~ 6a–b). Consistently, the tectonic force required to maintain the imposed extension velocity during Stage 1 is the largest for $D-Y_{500\,\mathrm{MPa}}$ (Fig. 6c), indicating a stronger deforming zone at the plate center, as also suggested by the low lateral viscosity contrast R_{visc} (Fig. ~~8a).The temperature delimiting the (deeper) dislocation-creep and the~~ 6e).

We interpret these differences using the weakening-partition diagnostics (Sect. 3.3), which quantify the relative contributions of strain-rate increase (F_{SR}) and temperature increase (~~top)~~ F_{T}) to viscosity reduction (Fig. 8). In all simulations, the shallow lithosphere is yield-dominated ~~lithosphere, is around 800 K, increasing slightly from Stage 1 to Stage 2. The area in yielding mechanism exhibits F_{SR} =100 % and can only be weakened by an increase in strain rate.In the lower part of the lithosphere ($800 < T < 1500$ K), the major cause of weakening smoothly switches from an increase in~~ and weakening is purely strain-rate ~~during Stage 1 ($F_{\mathrm{SR}} > 50$ %) to a temperature increase during Stage 2 ($F_{\mathrm{T}} > 90$ %).~~

~~Depth-time evolution of the relative contributions to weakening of the strain rate (F_{SR}) and temperature (F_T) computed at $x = 600$ km, for Simulations (a)$D - d_{LT-HT} - Y_{500\,\mathrm{MPa}}$ (*ref-1*) ; (b) $D - d_{HT} - Y_{500\,\mathrm{MPa}}$; (c) $D - Y$ 500 MPa ; and (d) $D - d_{HT} - Y^{950K}_{500\,\mathrm{MPa}}$. Light blue lines are the isotherms from 800 to 1500 K, the high- weakening zone is outlined in pink, and the dashed dark blue lines delimits the dominant deformation mechanisms as in Fig. 4.~~

4.4 ~~Influence of the rheological parameterization on the localization scenario~~

~~When no yield-stress rheology is implemented in the top, coldest part of the lithosphere, our experiments systematically result in non-localizing simulations with laterally-distributed deformation , regardless of the creep mechanisms (Table 3), as observed for Simulation *ref-0* (~~driven there ($F_{\mathrm{SR}} = 1$). Differences emerge in the deeper lithosphere, where deformation transitions to creep and where maximum weakening occurs. The temperature of the yield-to-creep transition depends strongly on the creep rheology: it is highest for diffusion creep alone (about 1300 K in $D - Y_{500\,\mathrm{MPa}}$), lower when high-temperature dislocation creep is included (about 1000 K in $D - d_{\mathrm{HT}} - Y_{500\,\mathrm{MPa}}$), and the lowest when low- to high-temperature dislocation creep is included (about 800 K in $D - d_{\text{LT-HT}} - Y_{500\,\mathrm{MPa}}$; Fig. ~~3a). This highlights the need to limit the resistance of the upper part~~ 8). These shifts imply that a thicker portion of the lithosphere ~~to allow plate weakening in the ductile mantle.~~deforms in the creep regime when dislocation creep is included, extending thermo-mechanical weakening to lower temperatures.

~~We now compare the localization scenarios obtained with rheologies different from Simulation *ref-1* ($D - d_{\text{LT-HT}} - Y_{500\,\mathrm{MPa}}$), either modifying the creep rheology and /or lowering the yield stress:~~

- ~~yield-stress and diffusion creep only ($D - Y_{500\,\mathrm{MPa}}$ or $D - Y_{200\,\mathrm{MPa}}$),~~
- ~~yield-stress, diffusion creep and high-temperature (HT) dislocation creep($D - d_{\mathrm{HT}} - Y_{500\,\mathrm{MPa}}$), possibly restricting the yield-stress domain to temperatures lower than 950 K ($D - d_{HT} - Y^{950K}_{500\,\mathrm{MPa}}$),~~
- ~~diffusion creep and LT-HT dislocation creep with a lower yield stress of 200 MPa ($D - d_{\text{LT-HT}} - Y_{200\,\mathrm{MPa}}$).~~

The ~~2-stage co-evolution of the lithosphere thickness h_{plate} vs. the width of the deformed zone w (Sect. 3)is similar for all simulations (~~weakening-partition diagnostics further show that dislocation creep enables both mechanical and thermal weakening within the creeping lithosphere. In rheologies that include dislocation creep, weakening is predominantly strain-rate driven during Stage 1 (typically $F_{\mathrm{SR}} > 60\%$ in the main weakening zone), while weakening becomes almost purely temperature-driven during Stage 2 (typically $F_{\mathrm{T}} > 0.9$; Fig. ~~7). Deformation is well-localized for all rheologies (plateness P converges to 1 - Fig 6d), with tectonic force F strongly decreasing in Stage 2 after the transition time t_{tr} (~~8a, b). In contrast, for diffusion

Table 3. List of numerical simulations with a half-extension rate $v_{1/2}$ of 1 cm yr^{-1} and an initial plate age of 50 Myr. Reference simulations for scenarios of distributed deformation 'distr. def.' (***ref-0***) or localized plate-boundary 'loc. PB' (***ref-1***) are shown in Fig. 3a and b, respectively. The intermediate regime of incomplete localization 'inc. loc.' is shown in Fig. D2c and f. The characteristic times of transition t_{tr} and plate-boundary formation t_{PB} are defined in Sect. 4.2.

Simulation name	Rheological combination			Outcomes		
	diff. creep	disl. creep	yield stress (MPa)	final state	t_{tr} (~~Ma~~Myr)	t_{PB} (~~Ma~~My
D	D	∅	∅	distr. def.	-	-
$D-Y_{200\ \mathrm{MPa}}$	D	∅	200	loc. PB	9.0	19.3
$D-Y_{500\ \mathrm{MPa}}$	D	∅	500	loc. PB	12.3	21.8
~~$D-d_{\mathrm{HT}}$~~ $D-d_{\mathrm{HT}}$ (***ref-0***)	D	HT	∅	distr. def.	-	-
$D-d_{HT}-Y_{200\ \mathrm{MPa}}$	D	HT	200	loc. PB	5.0	10.3
~~$D-d_{\mathrm{HT}}-Y_{500\ \mathrm{MPa}}$~~ $D-d_{\mathrm{HT}}-Y_{500\ \mathrm{MPa}}$	D	HT	500	loc. PB	6.5	11.5
~~$D-d_{\mathrm{LT\text{-}HT}}$~~ $D-d_{\mathrm{LT\text{-}HT}}$	D	LT-HT	∅	distr. def.	-	-
~~$D-d_{\mathrm{LT\text{-}HT}}Y_{200\ \mathrm{MPa}}$~~ $D-d_{\mathrm{LT\text{-}HT}}Y_{200\ \mathrm{MPa}}$	D	LT-HT	200	loc. PB	5.0	10.5
~~$D-d_{\mathrm{LT\text{-}HT}}-Y_{500\ \mathrm{MPa}}$~~ $D-d_{\mathrm{LT\text{-}HT}}-Y_{500\ \mathrm{MPa}}$ (***ref-1***)	D	LT-HT	500	loc. PB	6.5	11.8
$D-Y^{950\ \mathrm{K}}_{200\ \mathrm{MPa}}$	D	∅	200 (for $T<950\ K$)	~~inc.loc~~ distr. def.	-	-
$D-Y^{950\mathrm{K}}_{500\ \mathrm{MPa}}$	D	∅	500 (for $T<950\ K$)	distr. def.	-	-
~~$D-d_{\mathrm{HT}}Y^{900\ \mathrm{K}}_{200\ \mathrm{MPa}}$~~ $D-d_{\mathrm{HT}}Y^{900\ \mathrm{K}}_{200\ \mathrm{MPa}}$	D	HT	200 (for $T<900\ K$)	distr. def.	-	-
~~$D-d_{\mathrm{HT}}-Y^{950\mathrm{K}}_{200\ \mathrm{MPa}}$~~ $D-d_{\mathrm{HT}}-Y^{950\mathrm{K}}_{200\ \mathrm{MPa}}$	D	HT	200 (for $T<950\ K$)	inc. loc.	-	-
~~$D-d_{\mathrm{HT}}-Y^{900\ \mathrm{K}}_{500\ \mathrm{MPa}}$~~ $D-d_{\mathrm{HT}}-Y^{900\ \mathrm{K}}_{500\ \mathrm{MPa}}$	D	HT	500 (for $T<900\ K$)	distr. def.	-	-
~~$D-d_{\mathrm{HT}}-Y^{950\mathrm{K}}_{500\ \mathrm{MPa}}$~~ $D-d_{\mathrm{HT}}-Y^{950\mathrm{K}}_{500\ \mathrm{MPa}}$	D	HT	500 (for $T<950\ K$)	loc. PB	12.5	19.0
~~$D-d_{\mathrm{LT\text{-}HT}}-Y^{950\mathrm{K}}_{200\ \mathrm{MPa}}$~~ $D-d_{\mathrm{LT\text{-}HT}}-Y^{950\mathrm{K}}_{200\ \mathrm{MPa}}$	D	LT-HT	200 (for $T<950\ K$)	loc. PB	5.0	10.5
~~$D-d_{\mathrm{LT\text{-}HT}}-Y^{950\mathrm{K}}_{500\ \mathrm{MPa}}$~~ $D-d_{\mathrm{LT\text{-}HT}}-Y^{950\mathrm{K}}_{500\ \mathrm{MPa}}$	D	LT-HT	500 (for $T<950\ K$)	loc. PB	6.5	11.8

creep plus yield stress, weakening in the creeping domain is entirely temperature-driven ($F_{\mathrm{T}} \geq 1$; Fig. ~~6e). The maximum vertically-averaged weakening rate $\langle W\rangle_{1500\ \mathrm{K}}(x=600\ \mathrm{km},t)$ at the box center also peaks for all simulations around 10^{-13} s^{-1} at the end of Stage 2 before t_{PB} (Fig. 6f).However, strain localization is much slower in simulations $D-Y_{200\ \mathrm{MPa}}$, $D-Y_{500\ \mathrm{MPa}}$ and $D-d_{HT}-Y^{950K}_{500\ \mathrm{MPa}}$ (group~~ 8c), limiting mechanical weakening during Stage 1 ~~) compared to Simulations $D-d_{\mathrm{LT\text{-}HT}}-Y_{500\ \mathrm{MPa}}$, $D-d_{\mathrm{LT\text{-}HT}}-Y_{200\ \mathrm{MPa}}$ and $D-d_{\mathrm{HT}}-Y_{500\ \mathrm{MPa}}$ (group 2), as the characteristic times t_{tr}~~ and delaying the onset of rapid thinning. This interpretation is illustrated by Fig.9, which shows theoretical viscosity profiles for two idealized end-member evolutions: a 10-fold increase in strain rate at constant plate age, used as a proxy for Stage 1, and ~~t_{PB} are approximately doubled (Table 3). This is also evidenced by the more sluggish evolution of the deformed zone width w and the plate thickness h_{plate} at $x=600$ km~~ plate thinning at constant strain rate, used as a proxy for Stage 2. For a given creep law, the effect of a Stage-1-type strain-rate increase can be estimated from the viscosity contrast between the yield-creep transition and the warm sub-lithospheric layer at about 75 km depth (Fig.~~6a and bfor group 1).~~

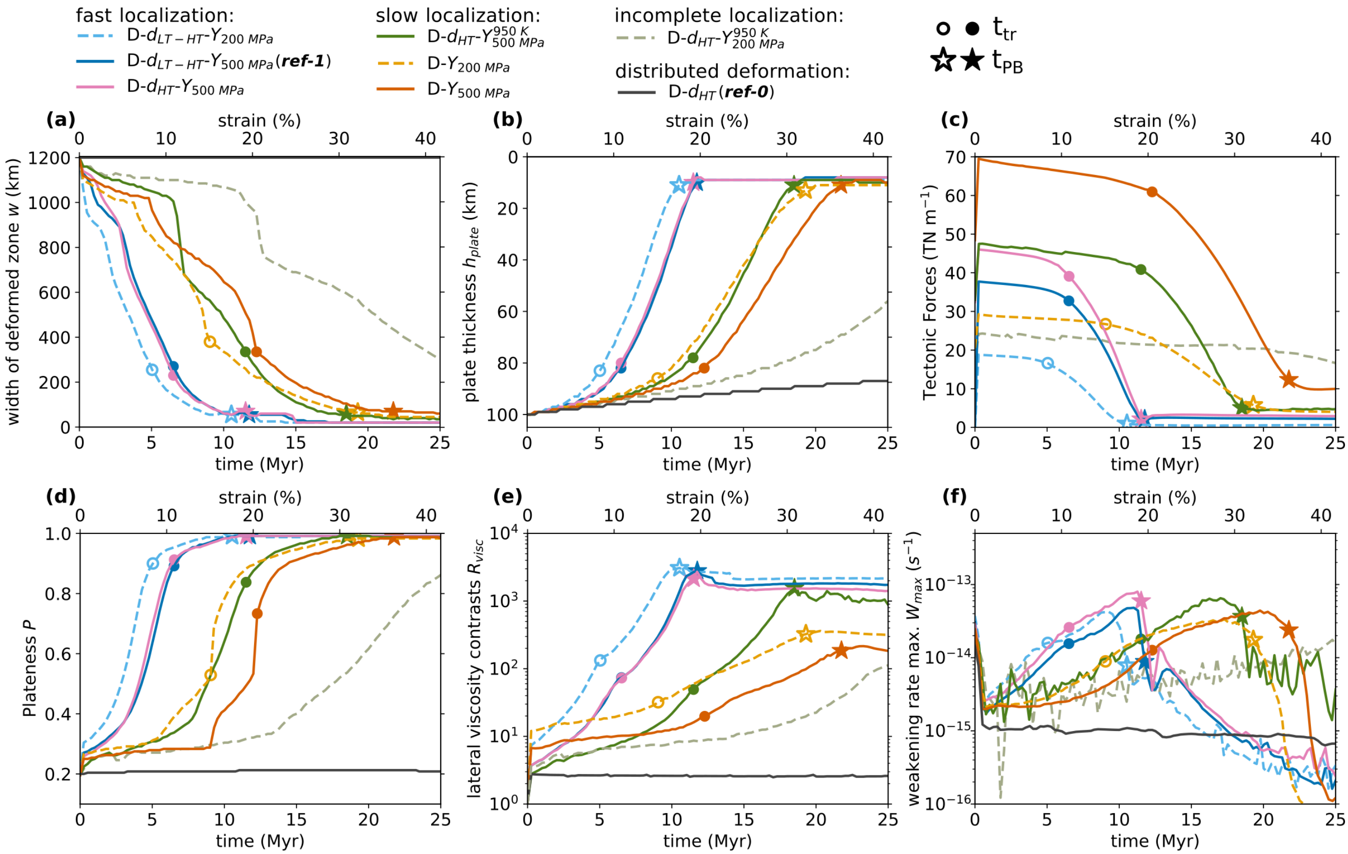

Figure 6. Temporal evolution (and corresponding cumulative strain in %) of diagnostics for simulations with 8 different rheological combinations, and the same initial plate age (50 Myr) and extension velocity ($v_{1/2}$ = 1 cm yr^{-1}). (a) width of deformed zone w, (b) plate thickness h_{plate} at x = 600 km, (c) tectonic force F, (d) plateness P, (e) lateral viscosity contrast R_{visc}, and (f) maximum weakening rate W_{max} over the whole lithosphere thickness (T < 1500 K) at x = 600 km. In all panels, characteristic times are indicated by dots (t_{tr}) and stars (t_{PB}).

~~Co-evolution of the minimum plate thickness $h_{\text{plate}}(t)$ as a function of the width $w(t)$ of the most deformed zone (see Sect.3.2) for experiments in which $v_{1/2}$ = 1 cm yr^{-1} and the initial lithospheric age is 50 Myr. The transition time t_{tr} between Stages 1 and 2 is indicated by a circle symbol (defined in Appendix B and in Fig B1), and , the localization time t_{PB} by a star symbol, with h_{plate} and w becoming steady after t_{PB}. Empty and filled symbols refer to rheologies with a yield stress set to 200 and 500 MPa, respectively. Time (and strain in %) evolution of (a) width of deformed zone w, (b) plate thickness h_{plate} at x = 600 km, (c) tectonic force F, (d) plateness P, (e) lateral viscosity contrast R_{visc}, and (f) maximum weakening rate W_{max} over the whole lithosphere thickness (T < 1500 K) at x = 600 km. Simulations have the same initial plate age (50 Myr) and extension velocity ($v_{1/2}$ = 1 cm yr^{-1}), but are computed using different rheological combinations.~~

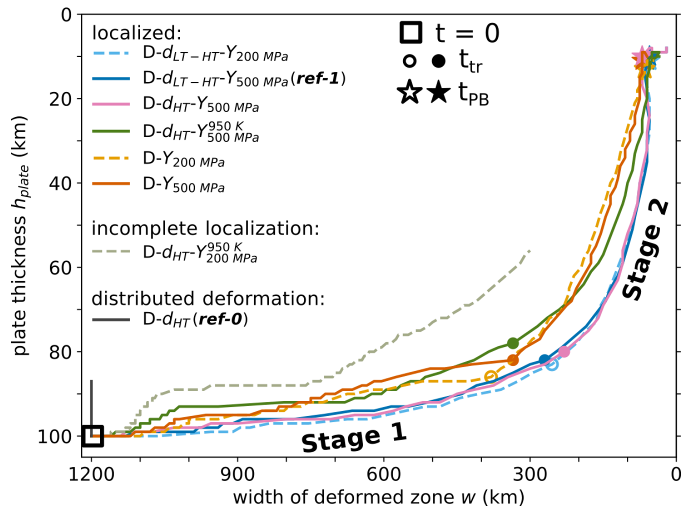

Figure 7. Co-evolution of the minimum plate thickness $h_{\text{plate}}(t)$ as a function of the width $w(t)$ of the most deformed zone (see Sect.3.2) for experiments with the same initial age (50 Myr) and extension velocity $v_{1/2}$ = 1 cm yr^{-1} for 8 different rheological combinations. The transition time t_{tr} between Stages 1 and 2 is indicated by a circle symbol and the localization time t_{PB} by a star symbol. Open and filled symbols correspond to rheologies with a yield stress set to 200 and 500 MPa, respectively.

~~Focusing first on Stage 1 (narrowing of spatial deformation with little plate thinning), we observe that the tectonic force F required to maintain the extension velocity (Sect. 3.2) is the largest for Simulation $D-Y_{500\text{ MPa}}$ (Fig. 6c) , indicating a stronger central deformed zone, as confirmed by the lower plateness and~~ 9b). By this measure, the ~~slower increase in lateral viscosity contrast (Fig. 6d and e). Figure 9a presents various vertical viscosity profiles and their evolution when strain rate increases ten-fold, as expected in~~ mechanical weakening associated with LT-HT dislocation creep (6-fold) is intermediate between that associated with HT dislocation creep (5-fold) and that associated with the yield-stress-plus-diffusion-creep rheology (10 or 1-fold). However, the 10-fold strain rate increase during Stage 1 ~~where the deformation focuses~~ produces the lowest absolute viscosities below the yield-creep transition. The same approach can be used to estimate the amplitude of Stage-2-type thermal weakening from the viscosity change accompanying lithospheric thinning and warming (Fig. ~~4a). The three fastest Simulations (group 2) exhibit weaker plates than Simulation $D-Y_{500\text{ MPa}}$, in particular between 900 and 1300 K. Interestingly, the mechanical weakening~~ 9d). Although the viscosity reduction associated with lithospheric warming is largest for diffusion creep (> 100) and smallest for LT-HT dislocation creep ~~rheology (factor 3-10 in viscosity decrease in Stage 1, Fig. 9b)is comparable with the ones of HT-dislocation creep~~ (~~factor 5,~~ < 40), the absolute viscosity reached after a given amount of warming and thermal rejuvenation remains lower when dislocation creep is included (Fig. 9~~b)and of yielding (factor 10, Fig. 9b), even though the mathematical formulations differ (Eq. 3, 2 and 8). Moreover, when the top lithosphere is weaker with a yield-stress of 200 MPa compared to 500 MPa (smaller force F in Fig.6c), we note that even if deformation localization is slightly faster, viscosity constrasts remain moderate when plate boundary is formed (Fig. 6e).~~ c).

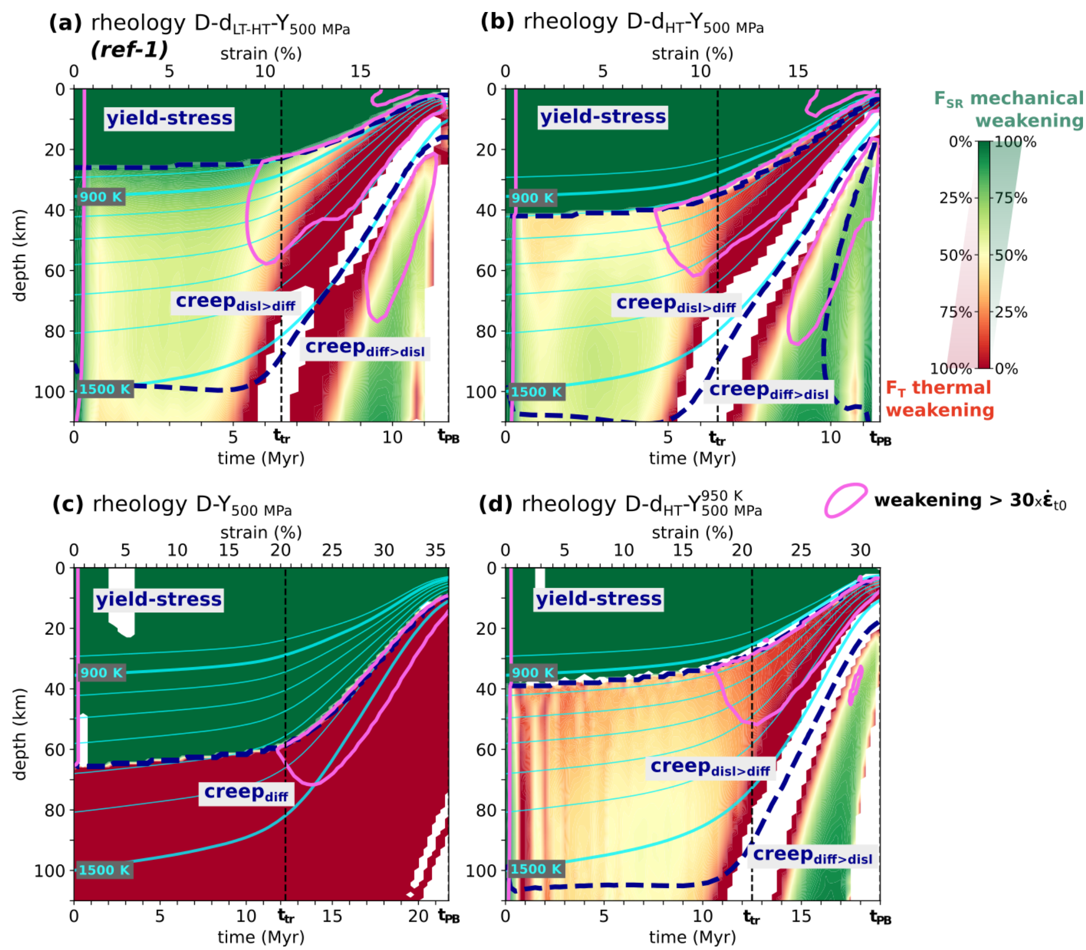

Figure 8. Depth-time evolution of the relative contributions to weakening from strain rate (F_{SR}) and temperature (F_T), computed at box center $x =$ 600 km, for simulations (a) $D - d_{LT-HT} - Y_{500\,\mathrm{MPa}}$ (*Ref-1*) ; (b) $D - d_{HT} - Y_{500\,\mathrm{MPa}}$; (c) $D - Y$ 500 MPa ; and (d) $D - d_{HT} - Y^{950K}_{500\,\mathrm{MPa}}$. The diagnostics are calculated only in regions in weakening ($W > 0$), with hardening or stable regions ($W \leq 0$) shown in white. The color scale is capped between 0 and 1. Areas of intense weakening, where the weakening rate normalized by the initial strain rate in the plate $\frac{W}{\dot{\varepsilon}_{t0}}$ exceeds 30, are highlighted by pink contours. Boundaries between dominant deformation mechanisms are marked by dashed dark-blue lines, and isotherms from 800 to 1500 K are displayed in light blue.

~~Thus, localization efficiency is not solely controlled by the resistance of the pseudo-brittle part of the lithosphere, and we explain the faster localization and larger weakening rate in Stage~~ Finally, restricting yielding to temperatures below 950 K produces a marked delay even when dislocation creep is present (compare $D - d_{\mathrm{HT}} - Y_{500\mathrm{MPa}}$ and $D - d_{\mathrm{HT}} - Y^{950\ \mathrm{K}}_{500\ \mathrm{MPa}}$; Table 3). Vertical profiles for the $D - d_{\mathrm{HT}} - Y^{950\ \mathrm{K}}_{500\ \mathrm{MPa}}$ case show that imposing a thermal cutoff on the yield rheology creates a stiff layer less than 4 km thick at the base of the shallow yielding domain, between the colder lithosphere above and the warmer creeping mantle below (Appendix C). Although thin, this layer remains mechanically important because it forms a local viscosity peak that slows the overall decrease in viscosity throughout the whole lithosphere, which in turns delays deformation focusing. This highlights the importance of capping the lithosphere strength in the creep domain within the mid-lithosphere temperature range (roughly 800-1300 K in these setups): even a thin stiff layer at these depths is sufficient to impede Stage 1 ~~for simulations featuring dislocation creep (Fig. 6f) by an efficient non-Newtonian feedback in the ductile domain: weaker plates promote a faster deformation focusing~~ narrowing and to delay both t_{tr} and t_{PB} (Fig. ~~4a), which causes both larger strain rates and upwelling rates (thus a temperature increase), further weakening the plate. We also note from Figure 8, which compares the physical controls on weakening at the box center, that a rheology featuring dislocation creep allows significant mechanical and thermal weakening throughout the ductile lithosphere, in particular $F_{\mathrm{SR}} > 50$ % at the plate base ($1300 < T < 1500$ K)~~9; Table3). This explains why lowering the yielding cutoff to 900 K inhibits localization within the simulated strain window (Table 3). Additional resolution tests show that, despite its striking sharpness, the presence of this high-stiffness layer is well resolved, and ~~$F_{\mathrm{T}} >$~~ is thus a robust result (Sect. S1.1. in the Supplementary Material).

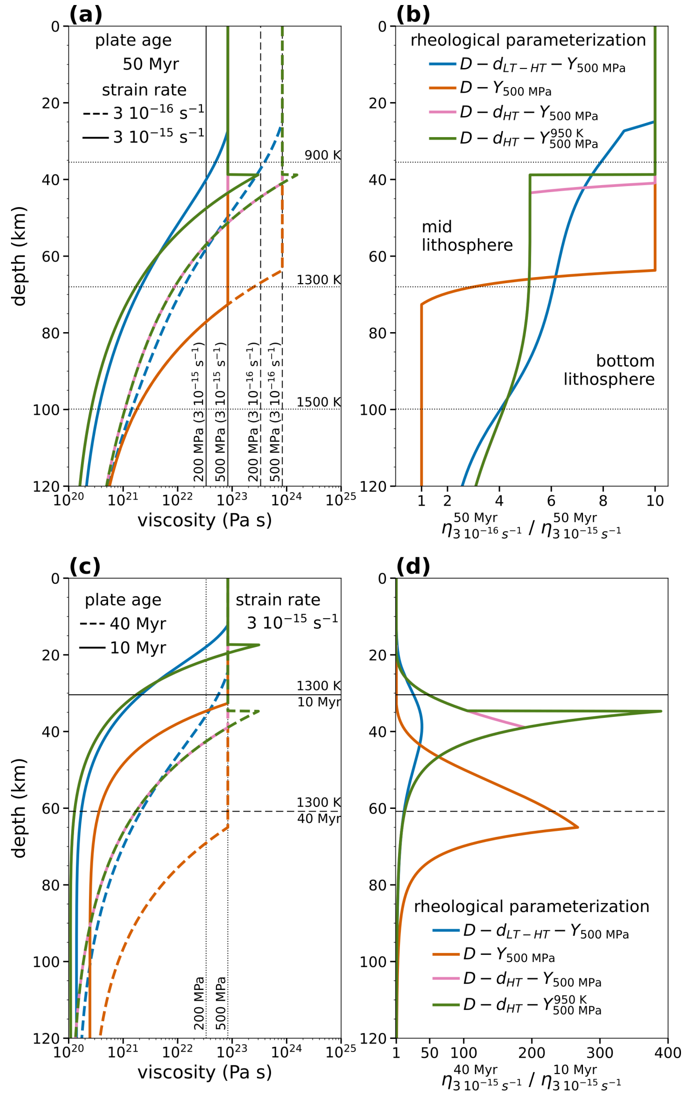

Figure 9. Theoretical (a,c) viscosity profiles, and (b,d) viscosity ratio illustrating (a-b) the effect of a 10-fold increase in strain rate with constant plate age of 50 Myr (proxy of Stage 1 evolution if temperature increase is neglected), and (c-d) the effect of thermal-structure variations associated with decreasing plate age from 40 to 10 Myr at a constant strain rate of 3 10^{-15} s^{-1} (proxy of plate thinning in Stage 2 assuming no mechanical contribution). Profiles are computed for 4 rheologies, with vertical black lines in panels (a) and (c) indicating yield viscosities corresponding to 200 or 500 MPa (eq. 8).

4.4 Influence of initial plate age and imposed extension rate

We test the robustness of the two-stage localization pathway and its sensitivity to: (i) the initial thermo-mechanical state of the lithospheric mantle and (ii) the magnitude of far-field forcing. We vary initial plate age (from 10 ~~% in the mid-lithospheric layer ($800 < T < 1300$ K). In contrast, for rheology $D-Y_{500\,\mathrm{MPa}}$, there is only thermal weakening (F_T = 100 %)at the plate base through Newtonian diffusion creep , and only mechanical weakening (F_SR =~~ to 100 ~~%)in the mid-lithospheric layer through yield-stress rheology.Thus, the basal lithosphere is more prone to weaken (thus to stretch) in~~ Myr), and the imposed half-extension rate (from 0.2 to 5 cm yr^{-1}). We focus on two rheological combinations that exhibit markedly different rates of deformation localization in the reference setup (Fig. 6): diffusion creep plus yield stress ($D-Y_{500\ MPa}$), and diffusion creep plus low-to-high-temperature dislocation creep plus yield stress ($D-d_{LT-HT}-Y_{500\ MPa}$) (Table 4).

Across most age-velocity combinations, the localization trajectory remains fundamentally characterized by a two-stage scenario: Stage 1 ~~for group~~is characterized by progressive narrowing of the deforming zone, while plate thickness changes only modestly; Stage 2 ~~simulations, enhancing plate thinning and asthenosphere upwelling.~~

~~This is confirmed by Simulation $D-Y_{200\,\mathrm{MPa}}$ (that does not feature dislocation creep), in which localization is slower than in Simulation $D-d_{LT-HT}-Y_{500\,\mathrm{MPa}}$, even if the plate strength is lower, as suggested by the tectonic force in Stage 1 (30 vs.38 TN m^{-1}, respectively,Fig 6f~~is characterized by rapid plate thinning associated with asthenospheric upwelling, with comparatively minor additional narrowing (Appendix D; Fig. D). The basic control on characteristic times is the extension rate, whereas initial plate age exerts only a weak influence (Fig. 10a,b). This ~~strengthens the idea that thermal and mechanical weakenings both occurring at mid-lithospheric depths accelerate deformation localization . Furthermore, Simulation $D-d_{HT}-Y^{950K}_{500\,\mathrm{MPa}}$ (group 1) highlights the crucial weakening of the lithosphere between 900-1300 K: if yielding is restricted to temperature lower than 950 K, then the high-viscosity thin layer at mid-lithospheric depth (Fig. 9a) is enough to hamper localization compared to Simulation $D-d_{HT}-Y_{500\,\mathrm{MPa}}$ (group 2 in~~ set of experiments further underlines that dislocation creep accelerates deformation localization relative to diffusion creep plus yield stress. For a given extension rate, the dislocation-creep rheology produces lower effective viscosity in the central deforming zone (typically by a factor of 5 to 10 at t_{tr}), which increases the lateral viscosity contrast between the weak zone and the plate interior and reduces the tectonic force required to maintain the imposed velocity (Fig. ~~6).~~

~~From~~ 10e, g). This enhanced strength contrast is expressed primarily through Stage 1~~to Stage 2, we observe in the lower part of the lithosphere between 900 and 1500 K, in all simulations involving dislocation creep, a transition from strain rate-dominated weakening ($F_\mathrm{SR} > 50$ %) in~~ : for all tested ages and velocities, the Stage 1 ~~to temperature-dominated weakening ($F_\mathrm{T} > 90$ %) in Stage~~ duration (measured by strain at t_{tr}) is shorter when using dislocation creep, while the differences in Stage 2 ~~(Fig. 8a, b and d) . On the other hand, mantle weakening in Simulation $D-Y_{500\,\mathrm{MPa}}$~~ timing are smaller and diminish further as extension rate increases.

Extension rate strongly modulates Stage 1 duration. Faster extension increases strain rate within the deforming zone, lowering effective viscosity via both yielding and (where active) dislocation creep, thereby increasing the narrowing rate (Fig. ~~8e) is either purely thermally-driven in the diffusion creep domain (F_T=100 %) or fully controlled by strain rate increase in the~~

~~yielding realm (F_{SR}=100 %). The larger weakening ($W > 30\,\dot{\varepsilon}_{t_0}$ pink contour~~ 10c,e). As a result, the total strain required to reach the transition from Stage 1 to Stage 2 decreases systematically with extension rate for both rheologies (Fig. ~~8)occurs in~~ 10a). In contrast, the Stage 2 ~~at lower temperature in the presence of dislocation creep~~ duration is comparatively insensitive to extension rate for $v_{1/2} \gtrsim 1\ \mathrm{cm\ yr^{-1}}$ (Fig. ~~8a,b,d) than in Simulation $D-Y_{500\ \mathrm{MPa}}$, for which it is restricted to diffusion creep domain at $T > 1300$ K~~ 10b), even though upwelling rates increase with extension rate (Fig. 10d). The maximum lateral viscosity contrast increases with extension rate up to $\sim 2\ \mathrm{cm\ yr^{-1}}$ and then saturates (Fig. ~~8e).~~

~~This suggests another feedback that is more efficient for rheologies featuring dislocation creep, as illustrated in Fig. 9b which presents the viscosity profile evolution during the upwelling in Stage 2 (approximated as plate age decrease from 50 to ~20~~10f), suggesting that once a sufficiently weak plate boundary is formed, it cannot weaken much further at higher extension rates.

Only the slowest forcing conditions fail to localize within the simulated strain window, and this occurs exclusively for the diffusion-plus-yield rheology. For old plates (50-100 Myr) ~~. Plate thinning induces a larger thermal weakening at shallower depths for dislocation creep compared to diffusion creep, allowing the upwelling to weaken the bulk of the plate (not only its base), hence promoting spatial localization of deformation.~~

~~Finally, we note that a very large portion of the lithosphere undergoes yielding in Simulation $D-Y_{500\ \mathrm{MPa}}$, limited by a temperature smoothly increasing from 1300 to 1400 K as strain rate rises during the simulation, compared to cooler temperatures of the yield-creep transition of 750-800 K for Simulation *ref-1*, 1000-1050 K for Simulations $D-d_{\mathrm{HT}}-Y_{500\ \mathrm{MPa}}$ and 950 K for Simulation $D-d_{HT}-Y^{950K}_{500\ \mathrm{MPa}}$ (~~extended at $v_{1/2} = 0.2\ \mathrm{cm\ yr^{-1}}$, localization remains incomplete by 40% strain (Table 4). In these cases, thermal diffusion can outweigh extensional thinning during early deformation, leading to net lithosphere thickening and delayed weakening (Appendix D; Fig. D1 and Fig. ~~8). Once the plate boundary is formed, almost all the lithospheric thickness is dominated by the yield stress rheology when the rheological parameterization excludes the creep flow by dislocation ($D-Y_{500\ \mathrm{MPa}}$).~~

~~Theoretical (a) (c) viscosity profiles, and (b) (d) viscosity ratio when (a) (b) increasing the strain rate as in Stage 1 (constant plate age of 50 Myr), or (c) (d) reducing the plate thickness as in Stage 2, here approximated as a decrease in plate age (constant strain rate of $3\cdot10^{-15}\ \mathrm{s^{-1}}$), computed for the 4 rheologies described in Sect. 4.3. The equivalent viscosities for yield stresses of 200 or 500 MPa (eq. 8) are also indicated using vertical lines in panels (a) and (c).~~ D2). Even in cases that eventually localize at low velocities or for initially young plates, the resulting plate boundary remains relatively wide and thick, and the maximum viscosity contrast remains modest ($R_{\mathrm{visc}} \lesssim 200$ at t_{PB}; Fig. 10f), indicating a weaker degree of focusing than in faster-extension cases.

4.5 ~~Influence of initial plate age and imposed extension rate~~

~~In this section, we compare the scenarios of deformation localization for simulations featuring, on the one hand, a different initial plate age (10, 30, 50 or 100 Myrs), which alters the thermal and mechanical structure of the lithospheric mantle, and, on the other hand, a different extension velocity $v_{1/2}$ imposed at plate sides, controlling the constant far-field extension~~

~~rate (0.2, 0.5, 1, 2 or 5 cm yr^{-1}).We consider only two rheological parameterizations for which plate age and/or extension velocity are varied: $D-Y_{500\,\mathrm{MPa}}$ and $D-d_{\text{LT-HT}}-Y_{500\,\mathrm{MPa}}$ (Table 4), since they result in clearly distinct scenarios of strain localization for the reference geodynamical set-up (initially 50-Myrs old lithosphere stretched at a half velocity $v_{1/2}$ of~~ The weakening-partition diagnostics clarify how forcing modulates feedbacks. At low extension rates (and in some young-plate cases, early in Stage 1), thermal hardening associated with cooling competes with mechanical weakening, such that net weakening in the ductile lithosphere is dominated by strain-rate effects (note that F_{SR} can exceed 1 ~~cm yr^{-1} - Sect. 4.3). The corresponding diagnostics are presented in Fig. 10, D1 and in Appendix D, Fig. D2, D3~~where temperature decreases while strain rate increases, Sect. 3.3). For the dislocation-creep rheology, this strain-rate-driven weakening extends to higher temperatures within the ductile lithosphere (up to $\sim$ 1300 K), supporting continued narrowing despite thermal hardening. By contrast, for diffusion creep plus yield stress, weakening below the yielding layer remains predominantly thermal; when cooling dominates early, the system remains in a thick yielding-dominated configuration that inhibits rapid focusing, contributing to incomplete localization under the slowest forcing.

~~For most combinations of initial lithospheric age and extension velocity, the overall 2-stage process of deformation localization and plateboundary formation (Sect. 4.3) remains unchanged at first order, with Stage 1 associated to narrowing of the more deformed region — with little variation in plate thickness — and Stage 2 to upwelling— with little change in the width of the deformed zone—. This is illustrated in Appendix D, Fig. D3 , which shows thickness vs. width for different ages and velocities and indicates that their co-evolution does not depend much on the rheology parameterizations , nor significantly on the extension velocity, with plate age setting the initial plate thickness. As in the reference set-up, we always observe a faster strain localization in Stage 1 for a rheology including dislocation creep compared to the sole combination of yield and diffusion creep (Fig. 10a). The mean plate viscosity $\langle\eta\rangle_{1500\,\mathrm{K}}$ at x = 600 km is 5-10 times lower for rheology $D-d_{\text{LT-HT}}-Y_{500\,\mathrm{MPa}}$ compared to $D-Y_{500\,\mathrm{MPa}}$, with greater lateral viscosity contrast between the weak boundary and the stiff plate interior (Fig. 10e and f).~~

~~For two experiments at very low half-extension rate (0.2 cm yr^{-1}), the formation of a new~~

Table 4. List of simulations investigating different lithospheric ages at spreading onset and half-spreading rates $v_{1/2}$. Three rheological combinations are tested (first column). The last two columns list the average strain obtained at the characteristic times of transition t_{tr} and plate-boundary t_{PB}, respectively (Sect. 3). The initial strain rate in the plate ($\dot{\varepsilon}_{t_0}$) is ~~homogeneous~~ spatially uniform and equal to: 7.47 10^{-17}, 1.87 10^{-16}, 3.73 10^{-16}, 7.47 10^{-16} and 1.87 10^{-15} s^{-1} respectively for $v_{1/2}$ = 0.2, 0.5, 1, 2 and 5 cm yr^{-1}.

Set-up parameterization			**Outcomes**				
rheology	$v_{1/2}$ (cm yr^{-1})	initial age (Myr)	final state	t_{tr} (Myr)	t_{PB} (Myr)	$\varepsilon(t_{\mathrm{tr}})$(%)	$\varepsilon(t_{\mathrm{PB}})$ (%)
$D - Y_{500\ \mathrm{MPa}}$	0.2	50	inc. loc.	-	-	-	>40 %
	0.2	100	inc. loc	-	-	-	>40 %
	0.5	50	loc. PB	27.5	46.0	22.9	38.4
	1	10	loc. PB	13.8	21.3	23.0	35.5
	1	30	loc. PB	12.5	22.0	20.9	36.7
	1	50	loc. PB	12.3	21.8	20.5	36.3
	1	100	loc. PB	12.3	20.5	20.5	34.2
	2	50	loc. PB	4.8	9.5	15.8	31.7
	5	10	loc. PB	1.9	3.5	15.5	29.2
	5	50	loc. PB	1.4	3.7	11.7	30.9
	5	100	loc. PB	1.4	3.6	11.3	29.7
$D - d_{\mathrm{LT\text{-}HT}} - Y_{500\ \mathrm{MPa}}$	0.2	10	loc. PB	46.1	96.1	15.4	32.1
	0.2	50	loc. PB	44.1	95.0	14.7	31.7
	0.2	100	loc. PB	45.0	99.0	15.0	33.0
	0.5	50	loc. PB	14.0	26.0	11.7	21.7
	1	10	loc. PB	5.8	9.5	9.6	15.9
	1	30	loc. PB	6.3	10.5	10.4	17.5
	1	50	loc. PB	6.5	11.8	10.9	19.6
	1	100	loc. PB	6.8	12.8	11.3	21.3
	2	50	loc. PB	2.8	5.0	10.0	16.7
	5	10	loc. PB	1.1	1.7	9.2	13.8
	5	50	loc. PB	1.2	2.0	9.6	16.3
	5	100	loc. PB	1.2	2.2	10.0	18.3
$D - d_{\mathrm{HT}}$	0.2	10	distr. def	-	-	-	-
	0.2	100	distr. def	-	-	-	-
	1	50	distr. def	-	-	-	-
	5	10	distr. def	-	-	-	-
	5	100	distr. def	-	-	-	-

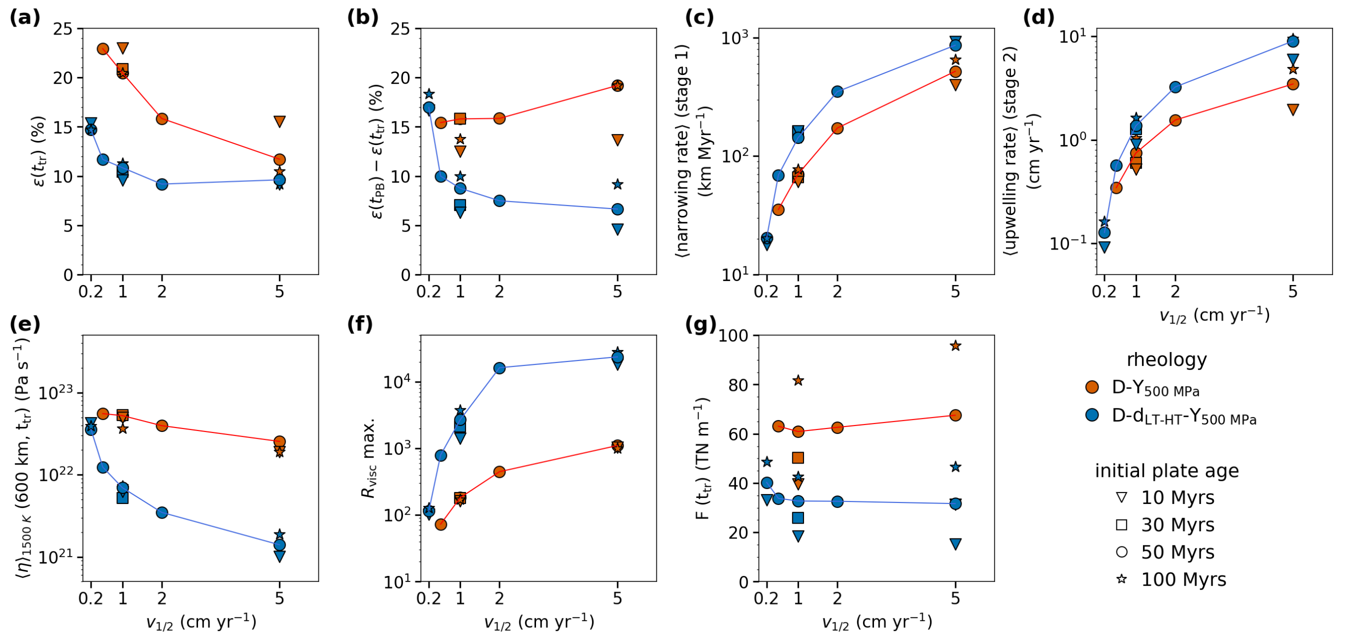

~~Diagnostics as a function of half-extension velocity $v_{1/2}$ for two different rheologies, $D-Y_{500\,\mathrm{MPa}}$ (red) and $D-d_{\mathrm{LT\text{-}HT}}-Y_{500\,\mathrm{MPa}}$ (blue). The symbols correspond to initial plates ages ranging from 10 to 100 Myrs. (a) Strain $\varepsilon(t_{\mathrm{tr}})$, as a proxy for duration of Stage 1. (b) Difference $\varepsilon(t_{\mathrm{PB}})-\varepsilon(t_{\mathrm{tr}})$ as a proxy for duration of Stage 2. (c) Narrowing rate during Stage 1. (d) Upwelling rate during Stage 2. (e) Effective viscosity vertically-averaged over the lithosphere thickness ($T<1500$ K) at $\mathrm{t_{tr}}$ and at the horizontal position $x=600$ km. (f) Maximum lateral viscosity contrast (R_{visc} max.) during the two stages, the maximum is reach around $\mathrm{t_{PB}}$. (g) Tectonic force F at time t_{tr}. In all panels, solid lines simply join the markers corresponding to the initial lithospheric age of 50 Myrs, used as a reference age.~~

Figure 10. Diagnostics as a function of half-extension velocity $v_{1/2}$ for two different rheologies, $D-Y_{500\,\mathrm{MPa}}$ (red) and $D-d_{\mathrm{LT\text{-}HT}}-Y_{500\,\mathrm{MPa}}$ (blue). Symbols represent initial plate ages ranging from 10 to 100 Myr. (a) Strain $\varepsilon(t_{\mathrm{tr}})$, used as a proxy for the duration of Stage 1. (b) Difference $\varepsilon(t_{\mathrm{PB}})-\varepsilon(t_{\mathrm{tr}})$ used as a proxy for duration of Stage 2. (c) Mean narrowing rate during Stage 1. (d) Mean upwelling rate during Stage 2. (e) Effective viscosity vertically-averaged over the lithosphere thickness ($T<1500$ K) at t_{tr} and at horizontal position $x=600$ km. (f) Maximum lateral viscosity contrast (R_{visc} max.) during the two stages, with a maximum reached around $\mathrm{t_{PB}}$. (g) Tectonic force F at time t_{tr}. In all panels, solid lines connect the markers corresponding to the initial lithospheric age of 50 Myr, used as a reference age.

5 Discussion

Taken together, our results show that lithospheric-scale strain localization in this extensional setting is controlled not simply by the integrated strength of the plate, but by where weakening occurs and how rheology couples deformation focusing to asthenospheric upwelling through rheology-modulated feedbacks linking deformation focusing, plate weakening and asthenospheric upwelling. Three main conclusions emerge. First, simulations showing deformation localization follow a robust two-stage evolution, with progressive narrowing followed by rapid plate thinning. Second, dislocation creep accelerates localization by extending thermo-mechanical weakening into a broader portion of the ductile lithosphere. Third, even a thin stiff layer in the mid-lithosphere can markedly delay plate-boundary formation, implying that simplified weak-plate parameterizations may miss an important control on localization efficiency. In the following, we discuss these points in turn and consider their implications for natural rifting and for large-scale geodynamical models.

5.1 A two-stage pathway to plate-boundary formation

A robust result of this study is that all simulations that successfully localize strain follow the same two-stage pathway to plate-boundary formation, irrespective of the rheological parameterization (Fig. 7). In Stage 1, deformation mainly focuses laterally: the width of the deforming zone decreases rapidly, whereas plate thickness changes only modestly. In Stage 2, the localization pattern shifts to rapid plate thinning driven by focused asthenospheric upwelling, while additional narrowing becomes limited. The transition between these two stages therefore marks the point at which a progressively focused deforming region evolves into a rapidly thinning lithosphere, at the end of which a mature plate boundary is ~~not achievedat 40 % strain (for rheology $D-Y_{500\,\mathrm{MPa}}$, 50 or 100 Myrs-old plates, 0.2 cm yr^{-1}, Table 4). We will comment on this result below~~achieved.

~~The initial plate age does not alter much the duration of strain localization : the strain necessary to complete plate boundary formation $\varepsilon_{\mathrm{PB}}$ remains encompassed between 15 and 20 % (resp. 30-36 %) for rheology $D-d_{\mathrm{LT\text{-}HT}}-Y_{500\,\mathrm{MPa}}$ (resp. $D-Y_{500\,\mathrm{MPa}}$), as presented in Table 4. By contrast, we find that, whatever the rheology, increasing the extension velocity, hence intraplate strain rate, results in (i) lower viscosity in the deformed zone at t_{tr}, (ii) faster localization during Stage~~ This two-stage behavior provides a simple physical framework for interpreting the localization process. Stage 1 ~~(decrease in $\varepsilon_{\mathrm{tr}}$ and increase in narrowing rate) Fig. 10a , c and e).Indeed, non-Newtonian viscosities (yielding and dislocation creep (Eq. 3 and 8) lessen the effective viscosity at high strain rates , thus accelerating deformation localization in Stage 1.~~

~~When the extension velocity is larger, plate thinning in Stage~~ is primarily a focusing problem, in which viscosity reduction within the deforming zone, allowed by non-Newtonian rheology, progressively increases the contrast with the surrounding plate interior. Stage 2 ~~is also faster (Fig. 10d), with larger weakening amplitude and stronger mechanical component compared to simulations with small $v_{1/2}$ (Fig. D1). A second-order effect is the shift to higher temperature of the deformation mechanism transition from yield stress to dislocation creep dominant and dislocation to diffusion creep dominant for $D-d_{\mathrm{LT\text{-}HT}}-Y_{500\,\mathrm{MPa}}$ rheology (Fig. D1), or from yield stress to diffusion creep for $D-Y_{500\,\mathrm{MPa}}$ rheology (Fig. D2). Thus, a higher proportion of~~

~~the plate is prone to mechanical weakening, even in~~ is primarily a thinning process, in which upwelling and heating beneath the localized zone further reduce temperature-dependent viscosity and accelerate lithospheric thinning. In that sense, the transition time t_{tr} represents a dynamical tipping point: beyond it, thermal weakening associated with asthenospheric upwelling becomes dominant and plate-boundary development proceeds rapidly.

A broadly comparable two-stage evolution has been inferred for some natural rift systems: the Atlantic and Australia-Antarctica rifts have probably undergone an early stage of deformation, at (total) extension rates slower than 1 cm yr^{-1}, lasting ~25-50 Myr, followed by an abrupt acceleration of extension over only 2-10 Myr (Brune et al., 2016). This acceleration is interpreted as the consequence of 'the rapid decrease of rift strength' in constant-force rifting models (Brune et al., 2016), and of 'a positive feedback loop between extension velocity and rift strength loss' in whole-mantle convection models Ulvrova et al. (2019). Our models do not reproduce such settings directly, particularly because extension is imposed kinematically rather than through a self-consistent far-field force balance.

We performed additional simulations with either an abrupt or a linear temporal increase of extension velocity imposed at side boundaries (Supplementary Material S.1.2.5.), in which the tectonic force F remains quasi-constant during Stage 1 before abruptly dropping during Stage 2 ~~, which accelerates the thinning of the lithosphere (see also deeper transition from diffusion creep to yield for higher strain rate in Fig. 9a).~~

~~As $v_{1/2}$ increases from 0.2 to 5 cm yr^{-1}, strain at the transition time $\varepsilon_{\mathrm{tr}}$ is roughly halved for rheology $D-Y_{500\ \mathrm{MPa}}$. In contrast, for rheology $D-d_{\mathrm{LT-HT}}-Y_{500\ \mathrm{MPa}}$, $\varepsilon_{\mathrm{tr}}$ decreases more modestly from 15 % ($v_{1/2}$=0.2 cm yr^{-1}) to a plateau around 10 % for $v_{1/2}\geq$1 cm yr^{-1} (Fig. 10a). This behavior is consistent with the isocontour of weakening normalized to initial intraplate deformation rate ($\frac{W}{\dot{\varepsilon}_{t_0}}>30$ - pink contour on~~ (Fig. S9 in the Supplementary Material). As in the constant-extension velocity models, Stage-1 narrowing is dominated by mechanical weakening, while Stage 2 is associated with thermal weakening with rapid F decrease and fast plate thinning (Fig. ~~D1)which shows that~~ 6, ref 8). We speculate that imposing forces or stresses at side boundaries, instead of imposing velocities, would result in a decrease in plate strength at time t_{tr}, and an increase in extension velocity, ~~for all initial plate ages, a larger intraplate region is affected as extension velocityincreases from 0.2 to 1 cm yr^{-1}. However, the overall weakening pattern remains similar for $v_{1/2}$ of 1 or 5 cm yr^{-1}. This plateau in 'localization efficiency' is further reflected in the stagnation of the lateral viscosity contrast for both rheologies as extensionrates increase from 2 to 5 cm yr^{-1} (Fig. 10f).~~

~~In simulations with slow extension (0.2 cm yr^{-1}), or young plates (10 Myrs) undergoing a mild extension speed ($v_{1/2}\lesssim$1 cm yr^{-1}), the lithosphere first undergo a moderate to strong thickening during Stage 1 (~~as predicted by rifting models and reconstructed in the natural rifting cases (Brune et al., 2016). Thus, we propose that rifting acceleration in nature may correspond to a geodynamic tipping point with thermal weakening of the lithospheric mantle enhancing plate strength drop, thus further promoting plate extension.

5.2 Importance of enabling thermo-mechanical weakening through dislocation creep

The clearest rheological result of this study is that simulations including dislocation creep localize deformation substantially faster than those with yield stress plus diffusion creep alone (Table 3; Fig. ~~D1 and D2~~6a,b). This ~~thickening rate is $\sim$0.1 cm yr^{-1}, and is higher for younger plates: thermal diffusion can overcome extension for low $v_{1/2}$ and young plates. In these experiments, significant lithospheric weakeningoccurs later~~ difference does not arise simply because the plate is weaker in some bulk sense. Rather, dislocation creep changes where and how weakening operates within the lithosphere and enhance the feedbacks leading to deformation localization: faster narrowing or thinning increases mechanical or thermal weakening, causing the decrease in viscosity at the domain center (associated with efficient focusing of deformation in Stage 1 ~~, with purely mechanical weakening (F_{SR}=100 %) also present within the dislocation creep domain at temperatures up to 1300 K).~~

~~Depth-time evolution of the relative contributions to weakening F_{T} and F_{SR} computed at the horizontal position $x = 600$ km where deformation is maximum for rheology $D - d_{\mathrm{LT\text{-}HT}} - Y_{500\ \mathrm{MPa}}$. Panels are displayed with rows varying by initial plate age and columns by half-extension velocity $v_{1/2}$. The central panel corresponds to the reference setup (initial plate age of 50 Myrs, half-extension rate of 1 cm yr^{-1}). The background colorbar is the same as Fig. 8, light blue lines are the isotherms from 800 to 1500 K, the high- weakening zone is outlined in pink, and the dashed dark blue lines delimits the dominant deformation mechanisms as in Fig. 4 and Fig. 8.~~

~~At such low intraplate strain rates, the region dominated by yield stress exhibit limited weakening, resulting in very slow lithosphere thinning. In the extreme cases of a 0.2 cm yr^{-1} half extension rate with rheology $D - Y_{500\ \mathrm{MPa}}$, only a thin basal portion of the lithosphere can be weakened by the temperature increase. This weakened base is minor compared to the 4-5 times thicker yielding-dominated lithosphere~~ and with rapid central upwelling in Stage 2), thereby increasing the lateral viscosity contrast, which in turn further enhances narrowing or thinning, and so on.

When dislocation creep is included, the transition from yield-dominated to creep-dominated deformation occurs at lower temperatures, so a larger fraction of the ductile lithosphere participates in creep deformation (Fig. ~~D2). Consequently, plate thinning progresses too slowly to achieve localization before the total strain reaches 40 %. Even for simulations that do achieve localization, for $D - d_{\mathrm{LT-HT}} - Y_{500\ \mathrm{MPa}}$ or $D - Y_{500\ \mathrm{MPa}}$ rheology, the lateral viscosity contrast at t_{PB} remains below 200 for a 0.2 cm yr^{-1} half extension, indicating that the plate boundary remains rather stiff and thick – at least $\sim$50-km thick for the rheology $D - d_{\mathrm{LT-HT}} - Y_{500\ \mathrm{MPa}}$ regardless of the initial plate age~~8). In practice, this extends weakening into colder parts of the deforming plate, particularly through the approximate 800-1300 K interval. As a result, dislocation creep broadens the part of the lithosphere that can respond dynamically to both increasing strain rate and increasing temperature, thereby enabling positive feedbacks over a thicker region.

6 ~~Discussion~~

5.1 ~~New diagnostics for weakening physical controls~~

~~Beyond the specific rheological comparisons, this study highlights the viscosity decrease ('weakening') during strain localization (Fig. 4), and introduces new diagnostics to quantify the physical origin of lithospheric weakening (Sect. 3.3). These new~~

~~diagnostics go beyond the classical assessment of strain localization using plateness (Tackley, 2000b) or shear zone relative width (Montési, 2013). We do not quantify in detail the growth rate of an instability (Kaus and Podladchikov, 2006) nor calculate *a priori* effective rheological properties (Montési and Zuber, 2002; Schmalholz and Fletcher, 2011). Rather, the new diagnostics F_{T} and F_{SR} apply to self-consistently evolving temperature and strain rate fields to quantify their separate contributions to weakening in a geodynamical setting.~~

~~Combined with more classical geometrical diagnostics of strain localization and plate thinning (Sect. 3.1 and 3.2), this framework offers several advantages. First, it disentangles the respective roles of mechanical and thermalfeedbacks, enabling us to track how weakening evolves during different stages of localization~~ The weakening-partition diagnostics show that this has two important consequences. First, during Stage 1, dislocation creep allows significant strain-rate-driven weakening within the creeping lithosphere, which promotes faster narrowing of the deforming zone. Second, during Stage 2, it permits stronger temperature-driven weakening over a thicker part of the lithosphere, which accelerates plate thinning once focused asthenospheric upwelling is established. In contrast, in diffusion-creep-plus-yield-stress simulations, weakening below the shallow yielding layer is almost entirely thermal, limiting mechanical weakening during Stage 1 and delaying the onset of rapid thinning (Fig. ~~4 and 8)and how it is influenced by plate age and extension rate (Fig. D1). Second, it allows us to analyze where in the lithosphere either thermal weakening, associated with both dislocation and diffusion creeps, or mechanical weakening, associated with either dislocation creep or yield-stress rheology, dominates (Fig. 8). Therefore, we can compare simulations with any rheological parameterization, including a combination of several creep mechanisms depending on the same physical state. Here, it highlights why dislocation creep , enabling both thermal and mechanical weakening , exerts such a strong influence on lithospheric weakening in the range 900-1200 K.~~

~~These diagnostics open new opportunities for application beyond our study on lithospheric extension with temperature and strain rate-dependent viscosities. They could be used to assess the role of dislocation creep in subduction zone initiation (e.g., Gurnis et al., 2004; Billen and Hirth, 2005; Ueda et al., 2008; Zhong and Li, 2019; Zhang et al., 2021; Arcay et al., 2023) , to test weakening feedbacks above mantle plumes (Thoraval et al., 2006; Ballmer et al., 2009; Agrusta et al., 2015), or to investigate co-dependent fields such as grain size (e.g., Bercovici and Karato, 2002; Fuchs and Becker, 2019; Dannberg et al., 2025) , which itself evolves dynamically with temperature and strain rate. More broadly, such diagnostics could be used to distinguish between weakening driven either by inherited properties (e.g. mechanical anisotropy, damage or smaller grain size) or by evolving thermo-mechanical fields, to analyze how damaged lithospheric zones may further promote plate break-up in their surroundings (e.g. Tommasi et al., 2009; Bercovici and Ricard, 2014; Fuchs and Becker, 2022).~~

5.1 ~~**Weakening of lithospheric mantle by yielding vs. dislocation creep**~~

~~Our simulations show thatweakening in the ductile domain partly controls the scenario of strain localization, with feedback efficiency depending on the rheological parameterization.~~

~~First, dislocation creep and yield-stress are not interchangeable at moderate-to-high temperatures (1000-1500 K): they both promote lithospheric weakening, but in different ways. Simulations without dislocation creep (e.g.~~ 8~~)~~.
This difference is also consistent with the analysis of the theoretical viscosity profiles shown in Fig.9 (Sect. 4.3). Relative to

diffusion creep plus yield stress, rheologies including dislocation creep produce the lowest viscosity associated with both mechanical weakening during a Stage 1-type strain-rate increase and stronger thermal weakening during a Stage 2-type thinning trajectory. In addition, dislocation creep extends both effects to lower temperatures and shallower depths. The main consequence is therefore not simply a lower viscosity, but a stronger coupling between deformation focusing, asthenospheric upwelling, and further weakening.

Our results further suggest that, ~~$D-Y_{500\ \mathrm{MPa}}$ or $D-Y_{200\ \mathrm{MPa}}$) localize much~~ if deformation is driven by far-field kinematics, as in our modeling conditions, overall lithospheric strength exerts only a second-order control on localization efficiency. For example, Simulation $D-Y_{200\ \mathrm{MPa}}$ localizes more slowly than ~~those that include it (e.g. $D-d_{HT}-Y_{500\ \mathrm{MPa}}$ or $D-d_{HT}-Y_{200\ \mathrm{MPa}}$). In the absence of (any) dislocation creep (rheologies $D-Y$), lithosphere weakening at the base of the plate cannot entail from the strain rate increase in Stage 1, since the diffusion creep viscosity is Newtonian ($F_{\mathrm{SR}}=0$ below 1300 K in Fig 8c, and no mechanical weakening in Fig. 9b). Furthermore, the absence of dislocation creep also prevents the colder heart of the mantle lithosphere(800< T < 1300 K) to be thermally weakened during plate thinning in Stages 1~~ simulations $D-d_{\mathrm{LT-HT}}-Y_{500\ \mathrm{MPa}}$ and ~~2. In contrast, when dislocation creep is modeled , the 10-fold increase in strain rate during Stage 1 further weakens the plate (Fig. 9b). This promotes a faster plate thinning starting in Stage 1 and accelerating in Stage 2 compared to simulations with rheologies $D-Y$ (Fig. 6b), which exhibits temperature-independent yield-stress rheology in most of the lithosphere (Fig. 8c). In turn, this further enhances thermal weakening through both diffusion and dislocation creep. This thermal weakening occurs at temperatures lower than 1300 K only in simulations featuring dislocation creep~~ $D-d_{\mathrm{HT}}-Y_{500\ \mathrm{MPa}}$, even though the former has a lower tectonic force during Stage 1 (Fig.6c). Extra simulations are performed with depth-dependent yield stress, keeping the peak strength of 500 MPa at the same depth as in the constant σ_Y simulations (Appendix E). These complementary tests exhibit comparable localization characteristic times despite the lower strength at the plate surface, which supports the previous conclusion: reducing near-surface strength does not substantially change localization times if a deeper mechanically important layer remains. Localization is therefore not controlled solely by average plate weakness, but by rheology-dependent feedbacks and by the depth distribution of strength within the lithosphere. Nevertheless, we acknowledge that the situation would be different if lithospheric deformation were instead driven by far-field constant stresses or forces, especially in case of a low to moderate tectonic rate. In such a setting, imposing a yield stress of 500 MPa instead of 200 MPa might significantly modify the evolution of lithospheric spreading.

The aforementioned feedbacks between the temperature and strain rate fields enabled by the activation of dislocation creep are modeled in our experiments while shear heating is not included. Shear heating has been proposed to enhance shear localization by thermal runaway (e.g. Fleitout and Froidevaux, 1980; Kaus and Podladchikov, 2006; Thielmann and Kaus, 2012; Kiss et al., 2019) . Using *a posteriori* calculations, we estimate a maximum heat dissipation rate for Simulation *ref-1* (~~Fig 8a and c~~$D-d_{LT-HT}-Y_{500MPa}$) larger than $\sim 10^{-6}$ W m^{-3} in a ~15 km thick layer directly below the yield-creep transition (Supplementary Material S3.2). Considering that a heat dissipation rate of order 10^{-5} W m^{-3} can lead to a temperature increase close to ~50 K (Kiss et al., 2020; Arcay et a
, we therefore expect that the temperature rise due to shear heating would remain lower than 50 K in our simulations. Therefore, including shear heating could foster thermal weakening in our experiments, further enhancing plate weakening and strain localization, but to a low-to-moderate extent. This effect is predicted to be especially emphasized when using (LT-)dislocation

creep for which the temperature-dependent creep layer is the thickest (Supplementary Material S3.2).

~~Second, in the absence of a~~ Taken together, these results show why yield-stress rheologies are not dynamically equivalent to rheologies that include dislocation creep at moderate to high temperatures. Dislocation creep accelerates localization because it expands the depth and temperature range over which both mechanical and thermal weakening can operate, thereby strengthening the feedbacks required to transform distributed extension into a localized plate boundary.

5.1 Implementing yield-stress or LT-dislocation creep as ductile strength-limiters

In these simulations, yield stress plays two distinct roles. First, it acts as a proxy for shallow pseudo-brittle weakening, enabling deformation of the very cold upper lithosphere. That role is essential in the present extension setting: without weakening of the shallow plate, deformation remains distributed and of low amplitude, even when dislocation creep is included. Some mechanism that weakens the cold upper lithosphere is therefore required in addition to any deeper ductile strength-limiter. Second, in rheologies that do not include low-temperature dislocation creep~~and when yielding is restricted to temperatures below 900-950 K, whatever the yield strength value, localization is either inhibited (Table 3 - Sim. $D-Y^{950\ K}_{500\ MPa}$, $D-d_{HT}-Y^{900\ K}_{200\ MPa}$, $D-d_{HT}-Y^{900\ K}_{500\ MPa}$) or delayed beyond 40 % strain (Sim. $D-d_{HT}-Y^{950\ K}_{200\ MPa}$, $D-d_{HT}-Y^{950\ K}_{500\ MPa}$). This outcome results from the presence of a high-viscosity layer (10^{25} Pa s) within the mid-lithosphere, whose thickness (a few kilometers at most) and strength depend on both the rheological parameterization, and the thermo~~, yield stress also limits the effective strength in a part of the deeper lithosphere. This is evident from the comparison between simulations with and without an imposed thermal cutoff for yielding. When LT~~–mechanical state of the plate (Fig. 9). This shows that a deformation mechanism which enables weakening is required for temperature higher than 900-950 K to achieve strain localization.Low-temperature dislocation creepand yield stress seem to play analogous roles in reducing the high lithospheric strength in the temperature range 800-1100 K , with comparable localization in models $D-d_{\mathrm{LT\text{-}HT}}-Y_{500\,\mathrm{MPa}}$ and $D-d_{\mathrm{HT}}-Y_{500\,\mathrm{MPa}}$~~ HT dislocation creep is present, restricting yielding to temperatures below 950 K has no effect on localization timescales. By contrast, when only HT-dislocation creep is included, the same restriction markedly delays localization or prevents it within the simulated strain window (Table 3). In ~~convection models reproducing plate-like surface dynamics for yield stresses lower than 300 MPa (Tackley, 2000a; Mallard et al., 2016), the yield-stress parameterization may represent a proxy for both brittle failure and deeper ductile weakening. In our models, the transition between yielding and diffusion creep occurs around 1300 K~~ that sense, when low-temperature dislocation creep is absent, the yield stress partly substitutes for a ductile strength-limiter within the approximate 800–1100 K interval, that is, across the temperature range over which deformation transitions from dislocation creep to yielding (Fig. 8~~c), several hundred degrees hotter than the observed seismological brittle–ductile transition (e.g. Engeln et al., 1986;~~ ~~. For crystalline materials and based on a homologous temperature about 0.4-0.6 relatively to the solidus temperature for olivine or peridotite, the transition from semi-brittle to ductile deformation is predicted to range from 600 to 1000 K (Wang, 2016; Hirschmann, 200~~). ~~This range is compatible with the transition between a 500-MPa yield-stress and either HT-dislocation creep (~1000 K, Fig. 8b), or LT-HT dislocation creep (~~This interval overlaps at least partly with the low-temperature ductile regime inferred for olivine at temperatures greater than about 800-900 K from laboratory and theoretical studies on melting and homologous temperatures (Wang, 2016; Hirschmann, 2000; Demouchy et al., 2023). It also overlaps with the mantle brittle-ductile transition expected up to approximately 600°C (900-1000 K), ~~Fig. 8a), but not with the transition between yield and diffusion creep for rheology $D-Y_{500\,\mathrm{MPa}}$ (1300 K~~as inferred from seismicity in the oceanic lithosphere (e.g. Engeln et al., 1986; Abercrombie and Ekström, 2 , and may extend to 900°C (1200-1300 K) under hydrous mantle conditions (Kohli et al., 2021), making the physical interpretation of such stress caps intrinsically ambiguous because deformation around the brittle-ductile transition is likely governed by multiple poorly constrained processes (Kohlstedt et al., 1995; Meyer et al., 2019).

Our simulations further show that lowering stresses of the shallowest part of the lithosphere does neither accelerate nor modify the breakup process (Appendix E), whereas even a stiff layer less than 5 km thick within the mid-lithosphere can strongly delay Stage-1 narrowing and therefore delay plate-boundary formation (sect. 4.3, Fig. ~~8c).~~

~~This thermal transition between the pseudo-brittle yielding and creeps deformation mechanisms depends both on the strain rate and on the rheological parameterizations for creep and yield stress. The presence of a mantle layer dominated by a pseudo-brittle yield stress-rheology will also depend on the geological setting. For example, a yield-stress rheology in~~ C1; Appendix C). This layer forms a thin but mechanically important bottleneck between the shallow yielding domain and the ~~mantle might not be needed below a 30-km thick continental crust when a~~ warmer, weaker creeping mantle. As long as this bottleneck remains strong, it dampens the feedbacks between deformation focusing, plate thinning, and further weakening, with strain rate increase lessened in the whole lithospheric section, hence milder ensuing viscosity reduction (Fig. C-b, c). In that sense, the relevant control on localization is not simply the weakness of the shallowest lithosphere, but the peak strength of the lithosphere, and whether the stiff layer can itself weaken. This underlines the need to cap the lithosphere strength beyond the brittle realm, in a temperature range corresponding approximately to 800-1000 K, i.e. the thermal range within the mid-lithosphere where the activation of HT-dislocation creep would otherwise lead to very high viscosities.

Our results therefore support the view that yield stress in geodynamical models should not be interpreted only as a shallow brittle proxy. In practice, it may also act as a first-order proxy for deeper ductile strength limitation when low-temperature ~~dislocation creep is implemented, except for very old plates (Fig. D1g,h,i). In contrast, we expect a~~ plasticity is not represented explicitly. Following Van Heck and Tackley (2008) and Tackley (2000a), we therefore suggest distinguishing between a shallow pseudo-brittle ~~mantle underneath a 10-km thick oceanic crust (Fig. D1).~~

~~Third, the low-to-high-temperature dislocation creep (Eq. 3)leads, at temperatures lower than 1000 K, to much lower differential stresses $\sigma_{\text{disl-LT-HT}}$ (Eq. 4) compared to high-temperature dislocation creep (e.g.~~ stress cap and a deeper parameterization representing low-temperature ductile strength limitation, even if the latter is not dynamically equivalent to LT-dislocation creep itself (Sect. 5.2).

Simulations with (LT-)-HT dislocation creep exhibit significantly lower tectonic forces F than simulations with only yielding and diffusion creep. In addition, using lower yield stress values also reduce the tectonic forces needed to maintain extension (Fig. ~~9). This is~~ 6c). Nevertheless, initial F values of approximately 20-40 TN m^{-1} remain on the high side compared to estimates proposed for natural rifting (~ 1 TN m^{-1}, Brune et al., 2023), ridge push ($\sim 2-3$ TN m^{-1}, Parsons and Richter, 1980) , but would be in agreement with ~~other formulations of olivine low-temperature plasticity (Evans and Goetze, 1979; Karato, 2008; Mei et al as compiled by Jain et al. (2017).~~

~~Our study demonstrates that~~ estimation of slab pull ($\sim 10-50$ TN m^{-1}, e.g., Conrad and Lithgow-Bertelloni, 2002; Toth and Gurnis, 19 . In large-scale mantle convection models, chosen yield stresses are low ($\lesssim$200-300 MPa, e.g. Richards et al., 2001; Crameri and Tackley, 2 , or with a low yield-stress increase with pressure (often $\lesssim 0.2$, e.g. Moresi and Solomatov, 1998; Korenaga, 2010; Crameri et al., 2012; Na compared to values derived from friction coefficients inferred from laboratory experiments (~ 0.6, e.g. Byerlee, 1978). These choices generally result in lithospheric strengths lower than laboratory-based estimates (>500 MPa, e.g. Kohlstedt et al., 1995; Karato, 200 , but they allow models to reproduce plate-like behavior and reorganizations (Janin et al., 2025). Our results suggest that including low-~~and high-temperature dislocation creep is a realistic mechanism able to induce significant weakening in the 'cold heart' of the~~ (to high-)temperature dislocation creep provides an alternative mechanism to act as a strength-limiter in the lithospheric mantle, ~~in between ∼800-1300 K. In the absence of dislocation creep, no thermal (resp. mechanical) weakening is possible in the cold region (resp. the bottom) of the lithosphere below 1100 K (resp. above 1300 K). Thus, models with a rheology combining only diffusion creep and yield stress (e.g. Coltice et al., 2019) may underestimate localization efficiency and over-predict the duration of continental break-up. In addition, low-temperature creep also explains deformed slab morphologies in the transition zone (Čížková et al., 2002; Garel et al., 2014)~~allowing a somewhat higher stress-cap, more consistent with deformation experiments, while still enabling plate weakening and strain localization. Other plausible mechanisms have also been proposed to generate plate-like behavior compatible with higher yield stress values, such as lateral strength heterogeneities associated with cratonic continental blocks (Rolf et al., 2012).

5.2 ~~Limitations~~ Implications for geodynamical models and limitations of the present study

~~The simulations presented in this study feature a unique (mantle) material, and do not explicitly model the presence of crustal layers with their own vertical strength variations (e.g. Burov, 2011a). We discuss further in Sect. **??** how our results can relate to natural cases of lithospheric rifting and spreading.~~

~~In addition to dislocation creep, mantle strength in the range 800-1300 K may also be controlled by the accumulation of damage/strain or the reduction in grain size (e.g. Precigout et al., 2007; Bercovici et al., 2015; Fuchs and Becker, 2021; Li and Gurnis, 202 . The interplay - and relative importance - of low-temperature dislocation creep relative to such strain-weakening effects will depend on the respective parameterizations for rheology and properties evolution, and is beyond the scope of the present study. Our simulations exhibit lithosphere weakening and strain localization even though no shear heating is implemented. The latter has been shown to enhance localization through thermal weakening (Fleitout and Froidevaux, 1980; Kaus and Podladchikov, 2006; Thielm , and we expect that , in our set-up, this would lead to an enhanced thermal weakening during Stage 1 and 2 where dissipation is expected to be large (increasing strain rates in the narrowing deformed zone), especially for regions deforming under dislocation creep.~~

~~Finally, we explore in this study only a controlled lateral extension on a 2-D domain. Including high-temperature~~ A central implication of this study is that rheologies combining diffusion creep with a simple yield-stress cap (e.g. Moresi and Solomatov, 1998; Tron may overestimate the time required to localize strain and form new plate boundaries. In our simulations, adding dislocation creep substantially accelerates localization relative to rheology $D-Y$ because it extends the thermal range of weakening in the ductile lithosphere and strengthens the feedbacks that link strain-rate increase, asthenospheric upwelling, and further viscosity reduction. This suggests that large-scale geodynamical models may localize too slowly if they omit this rheological contribution. Yet, including dislocation creep in whole-mantle convection simulations ~~may also increase plateness in mobile-lid regime, or decrease plate mobility in other cases, even possibly leading to stagnant-lid convection (Arnould et al., 2023). Indeed, in addition to lithosphere stiffness, the rheological parameterization affects~~ will have other dynamical consequences, such as a sub-plate asthenosphere weakening scaling with surface plate velocities (e.g. Patočka et al., 2024), or an increased mechanical decoupling at lithosphere-asthenosphere ~~viscosity contrast and mechanical decoupling , thus altering mantle flow wavelength and overlying plates' deformation and mobility (Arnould et al., 2023; Semple and Lenardic, 2021), with yet another feedback expected between plate velocities and asthenosphere weakening through dislocation creep (Patočka et al., 2024).~~

5.3 ~~Comparison with natural cases and models of rifting~~

~~To assess the applicability of our modeling results to geological settings, an interesting test is to evaluate whether the modeled forces, strain localization scenarios and its duration can be compared with extensional plate boundary formation in numerical modeling and in nature.~~ boundary that alters mantle flow and surface deformation pattern (Semple and Lenardic, 2021; Arnould et al., 2023)

.

~~Numerical models of continental rifting typically involve a 30-40 km thick crustal layer, and a 100-120 km thick lithosphere (Huismans and Beaumont, 2007; Brune et al., 2014; Gueydan and Précigout, 2014; Chenin et al., 2018; Tetreault and Buiter, 2018), which corresponds to a plate older than 50 Myrs. The simulated mode of rifting is mainly controlled by the lower crustal rheology. A very weak lower crust (i.e., $<$ 50 MPa at depth $>$ 20 km, e.g. using rheologies of wet quartzite, feldspar or wet feldspar, respec promotes mechanical decoupling between the crust and mantle, leading to a wide-rifting style (e.g., Gueydan et al., 2008; Tetreault and Bui This style of rifting exhibits an upwelling while deformation is still distributed in the crust, which is a different scenario from the two-stage evolution highlighted in our results~~More broadly, our results highlight a limitation of vertically-uniform stress-limiters. A low and constant yield-stress is not dynamically equivalent to a rheological structure in which shallow pseudo-brittle weakening coexists with a deeper ductile layer, since the latter can undergo strong thermo-mechanical weakening. The distinction matters because localization is sensitive not only to the integrated plate strength, but also to the depth distribution of strength and weakening. In particular, a thin stiff mid-lithosphere layer can act as a bottleneck that delays localization even when the plate is weak in a vertically averaged sense. This supports the view that simplified weak-plate approaches should distinguish a pseudo-brittle yield cap from a ductile strength, either self-consistently limited using low-temperature dislocation creep (e.g. Mei et al., 2010; Jain et al., 2017; Gouriet et al., 2019; Demouchy et al., 2023; Warren and Hansen, 2023), or capped with a so-called "ductile yield stress" as in Tackley (2000a); Van Heck and Tackley (2008).

~~In contrast, when a stronger lower crust (i.e., $<$ 300 MPa at depth $>$ 20 km, e.g. using dry quartzite or mafic granulite, respectively Ranalli is present and promotes mechanical coupling between the crust and mantle, rifting starts with a broadly distributed deformation, both in the crust and mantle. The deformed zone then smoothly narrows, with crustal faulting and associated mantle shearing. This stage is followed by crustal and lithosphere thinning, associated to a rapid asthenosphere upwelling (e.g. Huismans and Beaumont, 200~~

~~.Thus,~~ A second important result of our study is the ~~narrow-rifting style is comparable to our two-stage localization . We propose that the yield stress parameterization in our models approximates a mechanical coupling between a strong crust and the underlying lithospheric mantle (Fig. 9).~~introduction of weakening-partition diagnostics, that provide a general framework for analyzing the rheological control on deformation localization. By separating strain-rate-driven and temperature-driven contributions to viscosity reduction, they allow for identifying when localization is controlled primarily either by mechanical weakening or by thermal feedbacks. This weakening-partition diagnostics should be transferable to other geodynamic settings, including subduction initiation (e.g. Gurnis et al., 2004; Billen and Hirth, 2005; Ueda et al., 2008; Zhong and Li, 2019; Zhang et al., 2021; or plume-lithosphere interaction (e.g. Brune et al., 2013; Agrusta et al., 2015). It can also be extended to rheologies with additional state dependencies such as grain size, damage, or composition (e.g. Bercovici and Ricard, 2013; Fuchs and Becker, 2021; Dannberg et al., 2 .

The ~~absence of crustal layers in our models may also explain why the tectonic forces during Stage~~ main limitation of the present study is the mantle-only configuration. By excluding crustal layering, we isolate mantle rheological controls but do not attempt to reproduce the full mechanical complexity of natural rift systems. Crust-mantle coupling, lithological discontinuities, and additional weakening processes such as strain softening, grain-size evolution, and damage are all expected to promote a more rapid localization in a 'narrow-rift' setting featuring a strong lower crust (e.g. Allemand and Brun, 1991; Buck, 1991; Huismans and Beaum . Indeed, for rifting models under total extension around 1~~, in the simulations including dislocation creep (Fig 6c), range between 20 and 50 TN m^{-1}, which nears or exceeds the upper bound of available tectonic forces, e.g. rifting extension (~ 1 TN m^{-1}, Brune et al., 2023), ridge push ($\sim 2-3$ TN m^{-1}, Parsons and Richter, 1980), or slab pull, likely to drive plate kinematics in the vicinity of a subduction zone ($\sim 10-50$ TN m^{-1}, e.g., Conrad and Lithgow-Bertelloni, 2002; Toth and Gurnis, 1998; Sc .~~

~~Moreover, our simulations exhibit slower localization than other numerical models of 'narrow' continental rifting under constant-velocity boundary conditions. In these models with velocities $v_{1/2}$ of 0.4 to 0.5~~ cm yr^{-1} ~~, the transition time t_{tr} can be estimated around~~ (e.g. Brune et al., 2014; Gueydan and Précigout, 2014; Chenin et al., 2018) the corresponding transition time (t_{tr}) and break-up time (t_{PB}) are approximately 5 ~~Myrs, and the plate-boundary formation t_{PB} between 9 and 16 Myrs (Brune et al., 2014; Gueydan and Précigout, 2014; Chenin et al., 2018)~~Myr and 9-16 Myr, respectively, compared to ~~respectively~~ 14 and 26 ~~Myr in the model $D-d_{\text{LT-HT}}-Y_{500\,\text{MPa}}$ (Table 3). Even lower velocities ($v_{1/2} = 0.15$ cm yr^{-1}) exhibit plate break-up~~ Myr in our fastest model (rheology $D-d_{\text{LT-HT}}-Y_{500\,\text{MPa}}$). In that sense, the absolute times reported in this study are best interpreted as end-member values for a simplified mantle system, rather than as direct predictions for crust-bearing rifts. The interplay between low-temperature dislocation creep and additional weakening mechanisms will depend on the details of the rheological parameterizations and their evolution laws, but is beyond the scope of the present study (e.g. Precigout et al., 2007; Bercovici et . The presence of a crust also questions the existence of a brittle mantle (Burov et al., 2006), since the transition between pseudo-brittle yield-stress and LT-dislocation creep is expected around 800 K for a background strain rate of $10^{-16}-10^{-15}$ s^{-1} (Fig. 8), which corresponds to 27 km depth for a 50 Myrs old plate, i.e. shallower than a continental Moho (∼~~40 Myrs (Huismans and Beaumont, 2007), compared to 95 Myr in our simulation with $v_{1/2}$=0.2 cm yr^{-1} (Fig. D1). This likely comes from the very strong yielding layer at 500 MPa extending up to the surface in our simulations, while crustal resistance is~~

~~expected to be rather low at the surface, increasing with depth up to~~ 30-km deep), but deeper than an oceanic one ($\sim$~~300 MPa. Moreover, the presence of rheological discontinuity between lower crust and mantle is expected to enhance strain localization in the mantle (e.g., Allemand and Brun, 1991; Gueydan et al., 2008). Besides, we do not include any strain softening in our study as opposed to most rifting models (e.g. Huismans and Beaumont, 2003, 2007; Brune et al., 2013; Tetreault and Buiter, 2018; Heckenbach e , which@@ is known to enhance strain localization in the mantle (Frederiksen and Braun, 2001).~~

~~The compilation by Brune et al. (2017) suggests that the Iberian Newfoundland margin and the central South Atlantic rift segment have recorded an early phase of distributed deformation through crustal faulting, followed by a necking phase and rapid strain localization that ultimately lead to mantle exhumation and breakup. However, geological observations cannot precisely reconstruct the detailed evolution of lithosphere thinning relative to strain localization -e.g. Iberia-Newfoundland margin Pérez-Gussinyé et al. (2006); Pérez-Gussinyé (2013); Mohn et al. (2015); Tucholke et al. (2006, 2007) and South AtlanticChaboureau et a -, and cannot disentangle a 'narrowing' Stage 1 from a subsequent 'upwelling' Stage 2 as described in our results (Sect. 4.3). Similarly, in our simulations the narrowing of deformed zone overlaps with the incipient upwelling (Fig.5 & 7).~~ 4-10 km depth).

~~Nevertheless, some natural continental rift systems (for example : North East, Central North and South Atlantic rift, North America - Iberia rift or Australia-Antartica rift)seem to present an early stage of deformation, at (total) extension rates slower than 1 cm yr^{-1}, lasting ∼25-50 Myr, followed by an acceleration of extension over only 2 to 10 Myr (Brune et al., 2016) . This abrupt plate acceleration was reproduced in numerical models of rifting using constant tectonic boundary forces at domain sides (Brune et al., 2016), interpreted as a consequence of 'the rapid decrease of rift strength'. It was also described by Ulvrova et al. (2019) in 2-D spherical annulus models of mantle convection, proposed as the result of 'a positive feedback loop between extension velocity and rift strength loss'~~Neglecting elasticity is another limitation. This assumption may first lead to an overestimation (up to a factor of three) of shallow stresses in our models (Patočka et al., 2019). In our ~~models with constant-velocity imposed at domain sides, we observe a roughly constant tectonic force F during Stage 1 (Fig 6), since the lithospheric weakening remains low (Fig 4d) . The rapid decrease in F occurs during Stage 2 (Fig. 6), associated to intense lithosphere thermal weakening (Fig. 4-b & -d, Fig. 8). One may speculate that , assuming constant tectonic forces instead of constant velocity boundaries, the decrease in plate resistance at time t_{tr} would result in an increase in extension velocity, as predicted by rifting models and reconstructed scenarios in natural cases (Brune et al., 2016). Thus, rifting acceleration in nature could represent a geodynamic tipping point associated with a positive feedback between asthenospheric upwelling and lithosphere weakening, as long as far field forces remain stable over durations long enough~~visco-plastic experiments ('plastic' being here a synonym for 'brittle'), the central peak in shallow stresses (at 5-km depth) is located in the area where strain localizes, and where free-surface elevation is noticeable. If reducing shallow stresses by a factor 4 (as shown by additional tests with depth-dependent yield stress) indeed leads to smaller central depression (factor $\sim$ 3), it does not modify the two-stage weakening scenario or the timing of incipient plate-boundary formation (see Appendix E and Suppl. Mat. S3.1). This supports the conclusion that the localization mechanisms identified in our study are controlled primarily by the rheological structure of the mid- and lower lithosphere, rather than by shallow stress alone.

~~Back-arc basins, such as the Lau and South Fiji basins (Tonga subduction zone), the West Philippines, Parace Vela and Shikoku, and Izu-Bonin-Marianas basins (IBM subduction zone) and the Japan sea (Japan-Kuril subduction zone), are relatively short-living, lasting less than ~15 to 20 Myr, including both the~~ Neglecting elasticity by assuming a viscoplastic rheology also affects the prediction of brittle deformation and fault development. Previous studies comparing viscoplastic and visco-elasto-plastic formulations have shown that, although first-order stress patterns may be comparable, elasticity implementation will change fault geometry, spatial distribution, interaction and rotation, as well as the rift-topography evolution (e.g. Olive et al., 2016). In particular, our yield-stress formulation produces distributed viscoplastic flow over a finite volume rather than localized planar faulting, and therefore does not capture the detailed geometry of brittle shear-band development. Viscoplastic formulations may exhibit mesh sensitivity and numerical convergence issues (Duretz et al., 2020, 2021). Simulating a constant yield stress prevents the formation of ~~the new extensional plate boundaries and~~ shear bands in the pseudo-brittle layer (Watremez et al., 2013) . For a moderately fast extension, the pseudo-brittle layer deforms by pure shear in a layered lithosphere if the viscosity underneath the upper brittle layer is high ($\sim 10^{23}$ Pa s, Huismans and Beaumont, 2005), which may explain the absence of shear bands in our models with a moderate yield stress increase with depth (viscosity $\sim 10^{23}$ Pa s at the ~~time window of active spreading (Sdrolias and Müller, 2006; Deschamps and Lallemand, 2002; Jolivet et al., 1994; Martínez et al., 1995; Martinez and Taylor, 2 . These studies suggest that spreading generally initiates along or near the volcanic arc, which might represent a pre-existing localized zone of weakness at lithospheric scale.It is possible that Stage 1 would be strongly reduced during the formation of back-arc basins since deformation localization might be rapidly achieved thanks to a structural heterogeneity rather than through progressive narrowing as in our models.~~

yield-creep transition for a 500-MPa yield stress at $\dot{\varepsilon} = 10^{-15}$ s^{-1}, Fig. 9-a,c and Fig. C1). More physically grounded approaches, including damage-based rheologies and visco-elasto-plastic formulations accounting for weakening by microcracks growth, may therefore improve the representation of shallow deformation (Petit et al., 2024), but remain computationnaly demanding. We acknowledge that treating the shallow brittle layer more realistically could significantly modify the deformation pattern at shallow depths, but expect the large-scale feedbacks of lithospheric weakening documented in this study to remain broadly relevant.

6 Conclusions

~~Our study demonstrates how lithospheric weakening under extension emerges from the interplay of rheology , physical feedbacks, and tectonic forcing. The simulations reveal~~ Our 2-D thermo-mechanical extension experiments show that lithospheric-scale strain localization is controlled by the interplay between rheology and self-reinforcing thermo-mechanical feedbacks. In all simulations that successfully localize, plate-boundary formation follows a robust two-stage ~~process~~pathway: an initial ~~mechanically driven narrowing of deformation zones~~stage of progressive narrowing of the deforming zone, followed by ~~thermally accelerated weakening as asthenospheric upwellingintensifies. Low- to high-temperature dislocation creep provides the most realistic mechanism for weakening the mantle lithosphere across the ductile domain. While yield-stress rheologies~~

~~can mimic some aspects of this behavior, particularly at low temperatures, they cannot capture the feedbacks associated with high-temperature dislocation creep. As a result, models restricted to~~ a second stage of rapid plate thinning driven by focused asthenospheric upwelling. This two-stage evolution provides a simple physical framework for understanding how distributed extension evolves into a localized plate boundary.

A central result is that dislocation creep substantially accelerates localization relative to yield stress plus diffusion creep alone. This effect arises not simply because viscosity is lower overall, but because dislocation creep extends weakening into a broader and colder part of the ductile lithosphere. In doing so, it enables both strain-rate-dominated weakening during Stage 1 and stronger temperature-driven weakening during Stage 2, thereby enhancing the feedbacks that promote localization. By contrast, rheologies based only on diffusion creep plus ~~yield stress tend to overestimate the duration of strain localization and the timescale of plate break-up.~~

~~This study introduces new diagnostics that decompose viscosity changes into contributions from temperature and strain rate. By disentangling the thermal and mechanical drivers of weakening, this framework clarifies why rheologies including dislocation creep localize efficiently and complements existing measures such as effective stress exponents, viscosity contrasts, and shear-zone widths. These diagnostics~~ a yield-stress cap localize more slowly because weakening in the deeper lithosphere is more restricted.

Our results also show that localization depends on the depth distribution of weakening and strength. In particular, even a thin stiff layer within the mid-lithosphere can markedly delay Stage-1 narrowing and hence delay plate-boundary formation. This suggests that low-temperature dislocation creep acts as a ductile stress-limiter at temperatures of about 800-1100 K, similarly to the effect of common yield-stress parameterizations.

More broadly, this study introduces diagnostics that partition viscosity reduction into temperature-driven and strain-rate-driven contributions. These diagnostics directly link weakening to the evolving thermal and kinematic state of the system, clarifying why some rheological combinations localize efficiently whereas others do not. They also provide a transferable ~~tool to evaluate weakening feedbacks in other geodynamical contexts, from subduction initiation to plume–lithosphere interaction~~framework for analysing weakening processes in other geodynamic settings (e.g. subduction initiation and ~~grain-size–sensitive rheologies~~ ~~.~~

~~Together, these findings establish~~ plume-lithosphere interaction) and in rheologies with additional state dependencies.
Taken together, these results identify dislocation creep as ~~critical to achieve realistic~~ a key ingredient for efficient plate-boundary ~~formation, demonstrate the robustness of the two-stage weakening scenario across a wide range of plate ages and spreading velocities, and provide a new quantitative framework for systematically comparing lithospheric weakening processes across tectonic environments.~~

formation, and show that what matters most is not simply overall plate strength, but the spatial extent of thermo-mechanical weakening within the lithospheric mantle.

Appendix A: ~~Outflow at lateral boundaries~~

We compute a velocity profile $u_x(z)$ for a 1-D Couette flow

- with the half extension velocity $v_{1/2}$ at the top and a null velocity at the bottom,
- for a vertical viscosity profile following the diffusion creep rheology (associated to a temperature profile from the half-space cooling model for a 50 Myr-old plate). The 400 km-thick layer — corresponding to the domain thickness H — is discretized into 400 constant-viscosity layers.

Incompressible Navier-Stokes equations at steady-state for this 1-D horizontal Couette flow simplify to:

$$\frac{d^2\, u_x}{d\, z^2} = 0$$

Within each layer, the shear stress is constant and relates to the local viscosity (η_i) as:

$$\tau_{xz} \;=\; -\eta_i \frac{d\, u_x}{d\, z}$$

Continuity of horizontal velocity and shear stress is enforced at each layer interface. Together with the imposed boundary conditions, this leads to a well-posed linear system which solution provides the horizontal velocity profile $u_x(z)$.

The outflow velocity profile imposed at the domain sides in our simulations $v_x(z)$ is then defined as:

$$v_x(z) = \begin{cases} v_{1/2}(1 - \frac{z}{z_{\text{LAB}}}) + V(z_{\text{LAB}})\frac{z}{z_{\text{LAB}}} & \text{for } z \leq z_{\text{LAB}} \\ V(z) & \text{for } z > z_{\text{LAB}}, \end{cases}$$

where $V(z)$ is a 10th-order polynomial interpolation of the Couette velocity profile $u_x(z)$ below z_{LAB} (polynomial coefficients listed in Table S1 in the Supplement). z_{LAB} is the depth of 'constant-velocity' plate , defined following Garel and Thoraval (2021) as the depth where the horizontal velocity drops below 99 % of the surface extension velocity $v_{1/2}$ ($z_{\text{LAB}} = 89$ km for a 50 Myrs-old plate).

We perform sensitivity tests to assess the impact of using a single plate age (50 Myrs) to compute the outflow horizontal velocity profile, for all initial thermal plate ages in the simulations (10 to 100 Myrs). Comparisons between simulations using a 50 Myr plate age and those using 10 Myr (resp. 100 Myr) for the Couette flow calculation, in setups with an initial plate age of 10 Myr (resp. 100 Myr), showed only minor differences. The overall scenario and feedbacks remained similar, with only slight variations in timing, whether expressed in Myr or in terms of accumulated strain (Fig. S3 in the Supplement).

Appendix A: Inflow at the bottom boundary

At the bottom boundary, a purely vertical inflow is allowed over a region of width L_{in}=600 km centered at the middle of the domain, i.e., at $x = L/2$ = 600 km . Outside this region, a no-slip condition is imposed with $v_x(x) = v_z(x) = 0$.

~~To ensure mass conservation, the total vertical inflow through this open bottom section should balance the total horizontal outflow through the side boundaries, which is twice the integral of the horizontal velocity profile $v_x(z)$:~~

$$\int_{\frac{L}{2}-\frac{L_{in}}{2}}^{\frac{L}{2}+\frac{L_{in}}{2}} v_z(x)\,dx = 2\int_0^H v_x(z)\,dz$$

~~Within the central open section, the vertical velocity $v_z(x)$ is left free to adjust, with the central inflow peaking at ∼1 cm yr^{-1} for v$_{1/2}$ = 1 cm yr^{-1}~~

Appendix A: End-members of deformation pattern (distributed vs. localized)

The two end-member modes of lithospheric spreading, namely, distributed deformation and localized deformation, described in section 4.1, are assigned at simulation end (40 % of strain, corresponding to 500 km total surface extension) based on two main distinct diagnostics: plateness and lateral viscosity contrasts (Fig. ~~S4 in the Supplement). The lateral restriction of the inflow ensures that strain localization develops preferentially at the domain center, without the need for an initial heterogeneity in the lithosphere — e.g. a weak seed (Huismans and Beaumont, 2003, 2007; Tetreault and Buiter, 2018), or a thermal perturbation (Brune et al., 2012; Heckenbach et al., 2021).~~

~~In one simulation — with the same rheology, initial plate age and lateral spreading as in Simulation ***ref-1*** (Sect. 4.2) — the bottom inflow isenhanced, rather than letting v_z adjust to the flow dynamics, by imposing along the bottom boundary~~

$$v_z(x) = a\left(x-\frac{L_f}{2}\right)^2 + b$$

~~with a given maximum vertical velocity $v_{\max}$=6 cm yr^{-1} at the center. The coefficients a and b, and the width of the open bottom section L_f (here ∼ 130 km, Fig. S4) are derived from the mass conservation (Eq. **??**) assuming $v_z(x=L/2)=v_{\max}$.~~

~~As a result, the strainlocalization is faster in the presence of this enhanced vertical inflow (Fig **??**a), with a shorter Stage 1 (transition time $t_{\mathrm{tr}}=4.8$ vs 6.5 Myr, associated to a faster narrowing rate) and a comparable Stage 2 duration (localization time $t_{\mathrm{PB}}=9.8$ vs. 11.8 Myr, i.e. , less than 0.5 Myr difference when removing the shift in Stage 1 duration). The enhanced asthenosphere upwelling results in a higher intraplate strain rate at the box center, hence a slightly higher mechanical weakening ($F_{\mathrm{SR}}\geq 60$ % in the dislocation creep domain in Stage 1 compared to $F_{\mathrm{SR}}\geq 50$ % in Simulation *ref-1*~~A1). In some cases we observe an intermediate case, that is, incomplete localization, for which the deformation pattern has not reached any quasi-steady state at 40% of strain. For instance, the plate thickness h_{plate} has not reached any plateau after 40 % of strain (see Fig. ~~**??**~~6b).

~~This simulation may mimic the lithosphere deformation ahead of a plume arrival: increasing the vertical mantle inflow leads to stronger weakening and faster strain localization, even without introducing a thermal anomaly or melt weakening.~~

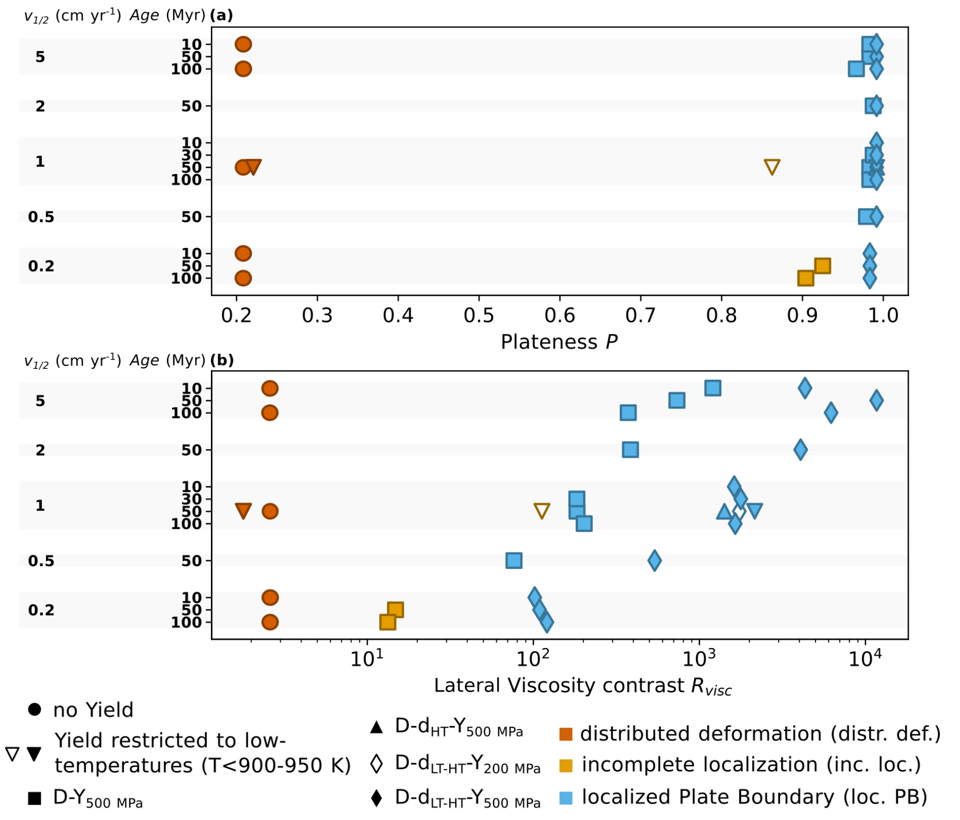

Figure A1. ~~Evolution of~~ (a) ~~vertically-averaged strain rate amplification~~ Plateness P and (b) ~~relative contributions to weakening F_T and F_{SR} computed at $x = 600$~~lateral viscosity contrast R_{visc} obtained after 40 ~~km~~ % strain for ~~the simulation with an imposed vertical inflow peaking at 6 cm yr^{-1}~~various extension rates, initial plate age, and rheologies. The ~~transition time t_{tr} is 4.8 Myr~~end-member simulations (distributed deformation, ~~while the formation of the~~ localized plate boundary~~is achieved at t_{PB}=9.8 Myr. Dashed contour refers to Simulation *ref-1* (free vertical bottom inflow)~~ ~~which outline in panel (a) the strain-rate amplification equal to 1 (in black) and~~ are depicted in ~~panel (b) $F_{SR} > 60$ %~~ red and ~~$F_T < 40$ % (~~blue, respectively. The incomplete localization case in yellow ~~)~~is intermediate between the two end-members.

Appendix B: ~~Iterative computation of creep viscosity consistent with deformation partitioning between diffusion and dislocation creeps~~

~~When both diffusion creep and dislocation creep (HT or LT-HT) are included in the rheological parameterization, the effective creep viscosity is computed as:~~

$$\eta_{creep} = \left(\frac{1}{\eta_{diff}} + \frac{1}{\eta_{disl}}\right)^{-1}$$

~~This formulation derives from assuming that strain rates are additive.~~

$$\dot{\varepsilon}_{creep} = \dot{\varepsilon}_{diff} + \dot{\varepsilon}_{disl}$$

~~under the condition of a single deviatoric stress σ~~

$$\sigma = 2\,\eta_{\text{creep}}\dot{\varepsilon}_{\text{creep}} \;=\; 2\,\eta_{\text{diff}}\,\dot{\varepsilon}_{\text{diff}} \;=\; 2\,\eta_{\text{disl}}\,\dot{\varepsilon}_{\text{disl}}$$

~~We implement the following iterative procedure to ensure that the dislocation creep viscosity η_{disl} is consistently evaluated using the dislocation creep strain rate $\dot{\varepsilon}_{\text{disl}}$. Indeed the velocity field only yields a total creep strain rate η_{creep}, and deformation partitioning between the creep mechanisms has to be computed iteratively (convergence within a few iterations - we thus enforce 20 iterations in our simulations).~~

~~This iterative procedure is initialized by computing the dislocation creep viscosity from the total creep strain rate, $\eta^0_{\text{disl}} = \eta_{\text{disl}}(\dot{\varepsilon}_{\text{creep}}, T)$ and the creep viscosity following eq. **??** as $\eta^0_{\text{creep}} = \left(\frac{1}{\eta_{\text{diff}}} + \frac{1}{\eta^0_{\text{disl}}}\right)^{-1}$ with $\eta_{\text{diff}} = \eta_{\text{diff}}(T, z)$. For the next iteration steps ($j \geq 1$), the assumption of a single stress (eq. 7) is used to modify the dislocation creep strain rate as:~~

$$\dot{\varepsilon}^j_{\text{disl}} \;=\; \dot{\varepsilon}_{\text{creep}}\,\frac{\eta^{j-1}_{\text{creep}}}{\eta^{j-1}_{\text{disl}}}$$

~~which is used to compute the dislocation creep viscosity as $\eta^j_{\text{disl}} = \eta_{\text{disl}}(\dot{\varepsilon}^j_{\text{disl}}, T)$. We then calculate a new creep viscosity as:~~

$$\eta^j_{\text{creep}} \;=\; \left(\frac{1}{\eta_{\text{diff}}} + \frac{1}{\eta^j_{\text{disl}}}\right)^{-1}$$

~~Finally, the amount of strain rate accommodated by dislocation creep is the ratio between $\dot{\varepsilon}_{\text{disl}}$ and $\dot{\varepsilon}_{\text{creep}} = \dot{\varepsilon}_{\text{diff}} + \dot{\varepsilon}_{\text{disl}}$ which, because of the condition of a single deviatoric stress, also corresponds to the ratio between the total creep viscosity and the dislocation creep viscosity :~~

$$\frac{\dot{\varepsilon}_{\text{disl}}}{\dot{\varepsilon}_{\text{creep}}} = \frac{\dot{\varepsilon}_{\text{disl}}}{\dot{\varepsilon}_{\text{diff}} + \dot{\varepsilon}_{\text{disl}}} = 1 - \frac{\dot{\varepsilon}_{\text{diff}}}{\dot{\varepsilon}_{\text{creep}}} = \frac{\eta_{\text{creep}}}{\eta_{\text{disl}}}$$

Appendix B: Transition time t_{tr} calculation

For ~~every~~ all "localized" simulations (loc. PB, Table 3, Table 4), we estimate the transition time ~~(t_{tr}) from the plate thickness (~~from the co-evolution of plate thickness $h_{plate}(t)$ ~~) evolving as a function of the~~ and width of the ~~highly deformed zone (~~enhanced deformed zone $w(t)$~~)~~. The transition time t_{tr} is defined as the point furthest from the line connecting the lithospheric structures at t_0 and t_{PB}, to the evolution curve $h_{plate}(t) - w(t)$ (Fig.B1). This point corresponds to the knee in the curve~~and corresponds to~~ , i.e. a transition between the first stage of ~~lithospheric spreading~~ extension during which deformation narrowing dominates (strong decrease in w while h_{plate} only slightly lessens) and the second stage, in which the ~~main development of the upwelling of the bottom of the lithosphere is on the contrary enhanced~~ asthenospheric upwelling dominates (moderate w reduction but strong lithospheric thinning and h_{plate} reduction). ~~Such a methodology used to define a threshold has been previously proposed, for example ,~~ Defining a transition with such a methodology was for example used to estimate the threshold in grain orientation spread to discriminate between recrystallized and relict grains of quartz from a given distribution of ~~intracristalline lattice distortion in each grain (e.g. Cross et al., 2017).~~ intracrystalline lattice orientation in a natural sample (e.g. Cross et al., 2017).

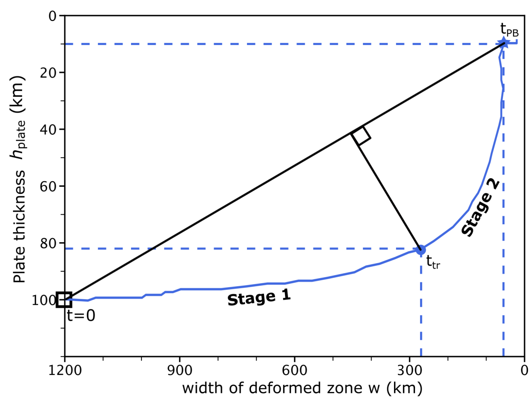

Figure B1. Definition of the transition time t_{tr} illustrated ~~by~~ using the reference experiment, Simulation *ref-1* (rheology ~~$D-d_{\text{LT-HT}}-Y_{500\,\text{MPa}}$~~ $D-d_{\text{LT-HT}}-Y_{500\,\text{MPa}}$). The transition time t_{tr} is determined as the time ~~when~~ at which the distance between the co-evolution of the deformed-zone width w and the plate thickness h_{plate} (blue line), and the straight line ~~linking~~ between the end-member states at $t = 0$ and $t = t_{PB}$ (black line) is maximum.

Appendix C: ~~Additional Figures~~Rheological feedbacks in the presence of a stiff mid-lithosphere layer

~~Additional Figure D2 displays the results obtained for~~ Simulation $D-d_{\mathrm{HT}}-Y_{500\ \mathrm{MPa}}^{950\ \mathrm{K}}$ investigates the effect of a thermal limitation imposed on the yielding realm. In this experiment, the yield stress rheology is restricted to temperatures lower than 950 K (see sect. 2.2.3) and is compared to Simulation $D-d_{\mathrm{HT}}-Y_{500\ \mathrm{MPa}}$ in which no thermal limitation is imposed (Table 3). Since brittle deformation in the lithospheric mantle has been argued to end at a temperature close to 900 K (e.g. Engeln et al., 1986; Abercrombie and Ekström, 2001; McKenzie et al., 2005), limiting yielding to a temperature around 950 K allows for modeling the lithosphere behavior if the brittle-ductile transition was controlled by a maximum temperature. Simulations performed without and with a temperature-capped yield rheology are compared using vertical profiles of temperature, strain rate and viscosity sampled at the center of the simulation box and computed at three different times (0, 4 and 13 Myr) at different stages of localization (Fig. C1).

At the start of simulations, the temperature of the yield-creep transition is close to 1000 K in Simulation $D-d_{\mathrm{HT}}-Y_{500\ \mathrm{MPa}}$ (Sect. 4.3) and is located at ~41 km depth, while the 950 K isotherm is at 38 km depth. As a consequence, if the yield stress is thermally-capped, dislocation creep is activated in a 3 km-thick layer below the yield boundary (38-41 km depth). In this layer, viscosities reach the highest values, locally exceeding 10^{24} Pa.s. After 4 Myr of lithospheric extension (end of Stage 1 in Simulation $D-d_{\mathrm{HT}}-Y_{500\ \mathrm{MPa}}$, the strain rate has increased with respect to the initial state by a factor of ~2.3 for the ~~$D-Y_{500\ \mathrm{MPa}}$ rheology~~ thermally-capped yield rheology, while this increase is doubled in Simulation $D-d_{\mathrm{HT}}-Y_{500\ \mathrm{MPa}}$. As a result, the viscosity in the yielding realm is decreased by a factor 2 for the temperature-capped yield, instead of 3 without the thermal limitation in yield.

The difference between the two simulations in the average lithospheric strain rate at the box center is amplified through time. As Stage 2 proceeds for Simulation $D-d_{\mathrm{HT}}-Y_{500\ \mathrm{MPa}}^{950\ \mathrm{K}}$, a strong lithospheric thinning at 13 Myr (1200 K increase at 5 km depth relative to the initial state) adds thermal weakening to mechanical weakening (200-fold increase in strain rate), which reduces viscosity by a factor ~2400 with respect to the initial state. The corresponding viscosity weakening is limited to a ~170-fold decrease for the thermally capped yield rheology.

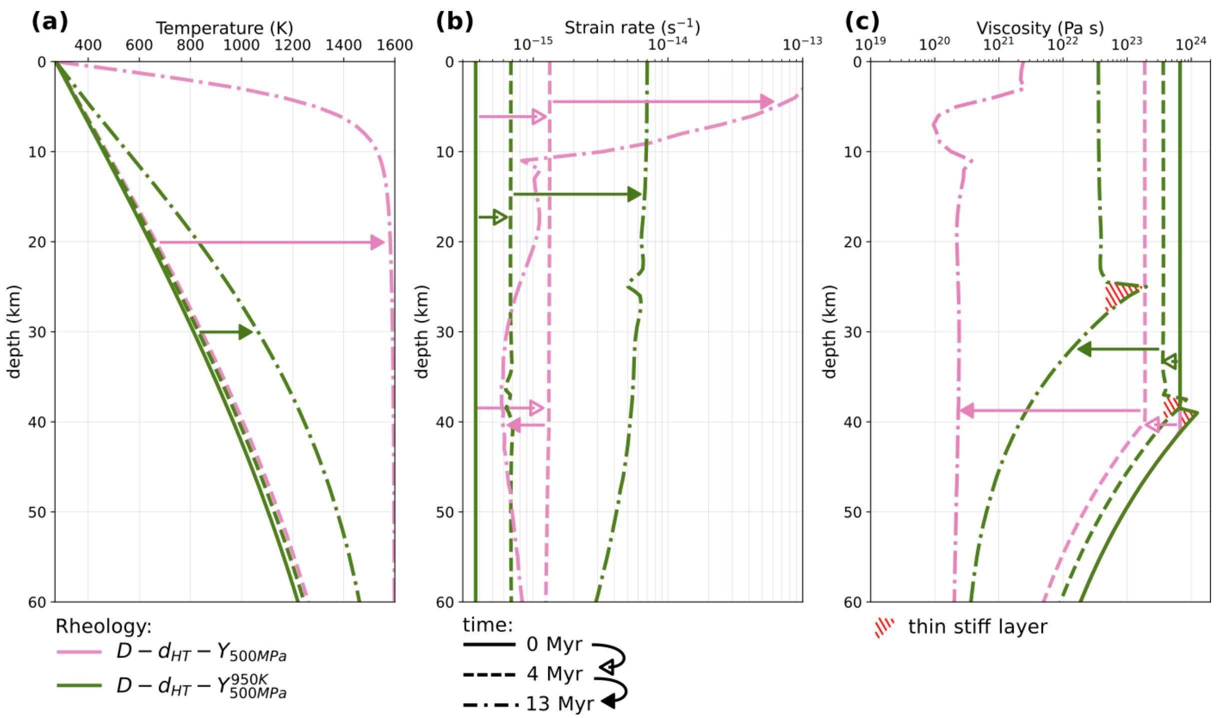

Figure C1. Vertical profiles of (a) temperature, (b) strain rate and (c) effective viscosity at $x = 600$ km at three different times (0, 4 and 13 Myr) for two rheologies $D - d_{HT} - Y_{500MPa}$ (pink) and $D - d_{HT} - Y^{950K}_{500MPa}$ (green) differing only by the temperature cut-off imposed for the yielding rheology. The thin stiff layer forming for rheology $D - d_{HT} - Y^{950K}_{500MPa}$ is highlighted by the red hatched area Arrows depict the time evolution.

Appendix D: Varying the extension rate and initial thermal plate age

Figures D1 and D2 display the thermomechanical evolution modeled at the box center obtained for rheologies $D - d_{LT-HT} - Y_{500\,\mathrm{MPa}}$ and ~~for various initial plate ages~~ $D - Y_{500\,\mathrm{MPa}}$, respectively, when the initial plate age and half-extension ~~rates~~ rate are varied (Sect. 4.4). ~~In particular~~At low velocity, the early extension stage is characterized by the cooling of the lithosphere (thermal hardening). As a consequence, the material weakening results from mechanical weakening only even in the ductile part of the lithosphere (dark green, Fig. D1a, b, d, g). In particular, panels D2c and f illustrate a scenario of incomplete localization (Sect. 4.1, Table 4), where ~~localization~~ complete localization of deformation is not achieved at the end of the simulation when strain reaches 40 %.

~~Additional~~ Figure D3 provides a global illustration of the two-stage evolution in simulations for various initial plate ages and half-extension velocities (Sect. 4.4). The curves for the same initial plate age are almost superimposed, except for low velocity $v_{1/2} = 0.2$ cm yr^{-1} which exhibits thickening during the early Stage 1. The 'incomplete localization' scenario of the simulation with rheology $D - Y_{500\,\mathrm{MPa}}$ for an initial 50 ~~Myrs-old~~ Myr-old plate and $v_{1/2} = 0.2$ cm yr^{-1} (Sect. 4.1, Table 4) is illustrated by the pink curve in Fig. D3b: at the end of the simulation (strain of 40 %), the plate is still thicker than 700 km and the deformed zone wider than 150 km.

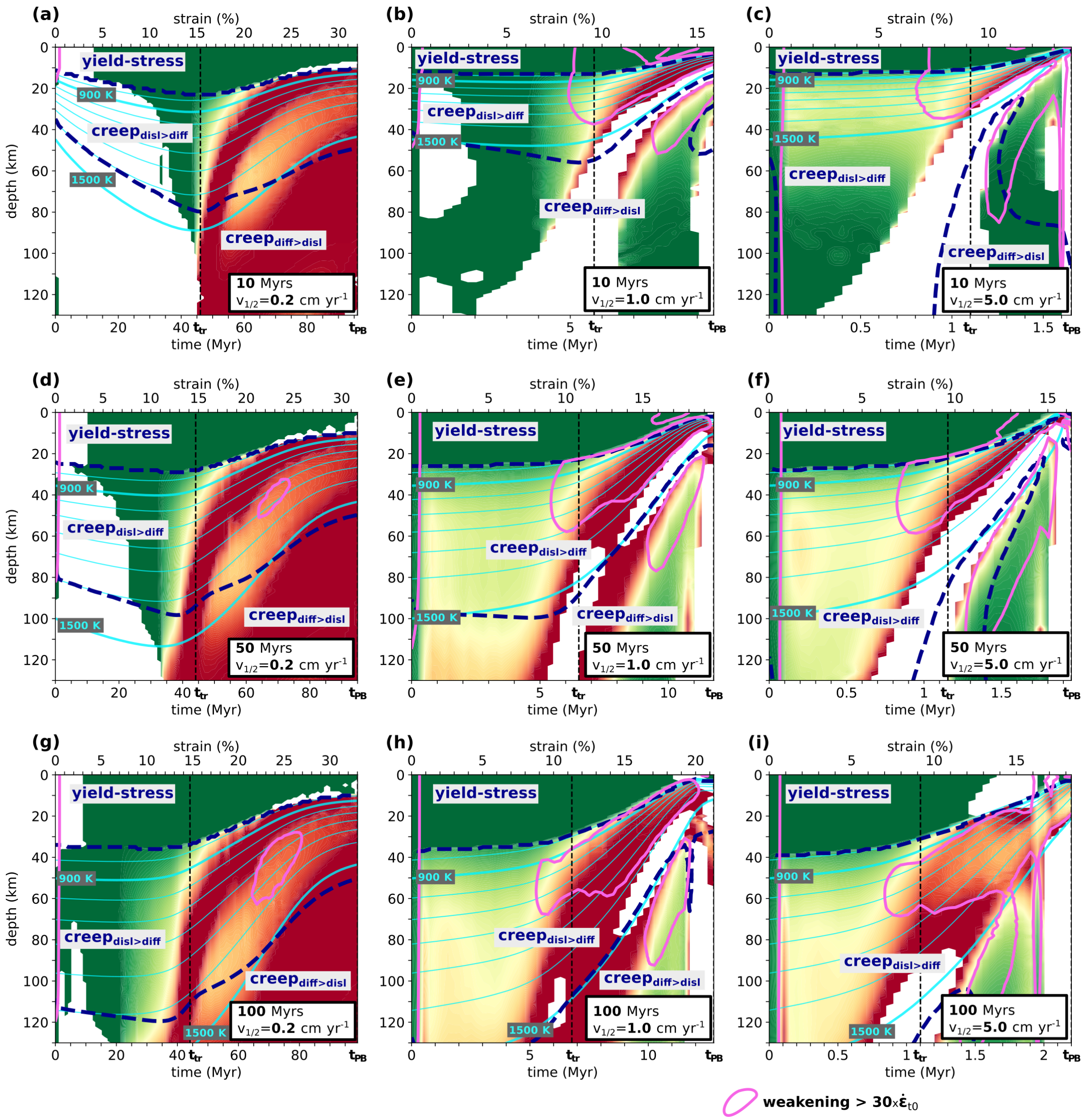

Figure D1. (This figure uses the same representation as Fig. 8 in the main text.) Depth-time evolution of the relative contributions to weakening F_T and F_{SR} calculated at box center $x = 600$ km with rheology $D - d_{\text{LT-HT}} - Y_{500\,\text{MPa}}$. Rows correspond to varying initial plate age and columns to varying half-extension velocity $v_{1/2}$. The central panel represents the reference setup (initial plate age of 50 Myr, half-extension rate of 1 cm yr^{-1}). In each panel, time varies from 0 to t_{PB} (which differs from one panel to another), and the transition time t_{tr} is indicated by a vertical dashed line. The diagnostics are calculated only in regions experiencing weakening (W0), hardening or stable regions ($W \leq 0$) being displayed in white. The color-scale is saturated between 0 and 1. Zones of intense weakening, where the weakening rate normalized by the initial strain rate in the plate $\frac{W}{\dot{\varepsilon}_{t0}}$ exceeds 30, are outlined in pink. Boundaries between dominant deformation mechanisms are outlined with dashed dark-blue lines as in Fig. 4, and isotherms from 800 to 1500 K are displayed in light blue.

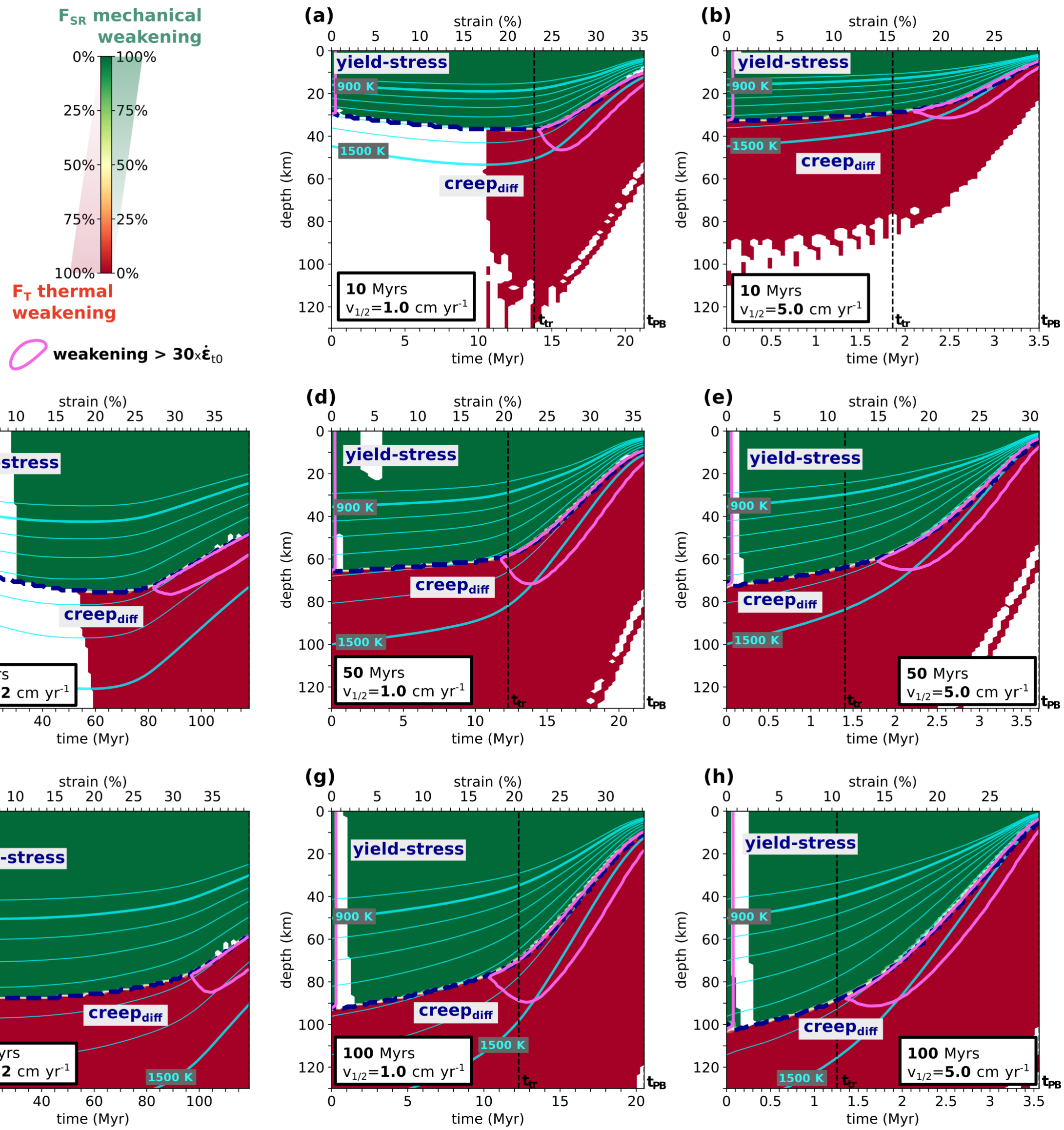

Figure D2. (This figure uses the same representation as Fig. 8) in the main text.) Depth-time evolution of the relative contributions to weakening F_T and F_{SR} ~~computed~~ calculated at ~~the horizontal position~~ box center $x = 600$ km ~~where deformation is maximum for~~ with rheology $D - Y_{500\,\mathrm{MPa}}$. Panels are ~~displayed~~ organized with rows corresponding to varying ~~by~~ initial plate age and columns ~~by~~ corresponding to varying half-extension velocity $v_{1/2}$. The central panel ~~corresponds to~~ represents the reference setup (initial plate age of 50~~Myrs~~ Myr, half-extension rate of 1 cm yr^{-1}). ~~Light blue lines are the isotherms~~ In each panel, time varies from ~~800~~ 0 to ~~1500 K~~ t_{PB} (which differs between panels), and the ~~high- weakening zone~~ transition time t_{tr} is ~~outlined~~ indicated by a vertical dashed line, except in ~~pink~~(c-f) where localization is not achieved and the results are shown for the total duration of the simulation. The diagnostics are calculated only in regions in weakening (W0), with hardening or stable regions ($W \leq 0$) shown in white. The colorscale is capped between 0 and 1. Zones of intense weakening, where the ~~dashed dark blue line delimits~~ weakening rate normalized by the initial strain rate in the plate $\frac{W}{\dot{\varepsilon}_{t0}}$ exceeds 30, are highlighted in pink. Boundaries between dominant deformation mechanisms are marked by dashed dark-blue lines as in Fig. 4, ~~Fig. 8~~ and ~~Fig.~~ isotherms from 800 to 1500 ~~D1~~K are displayed in light blue.

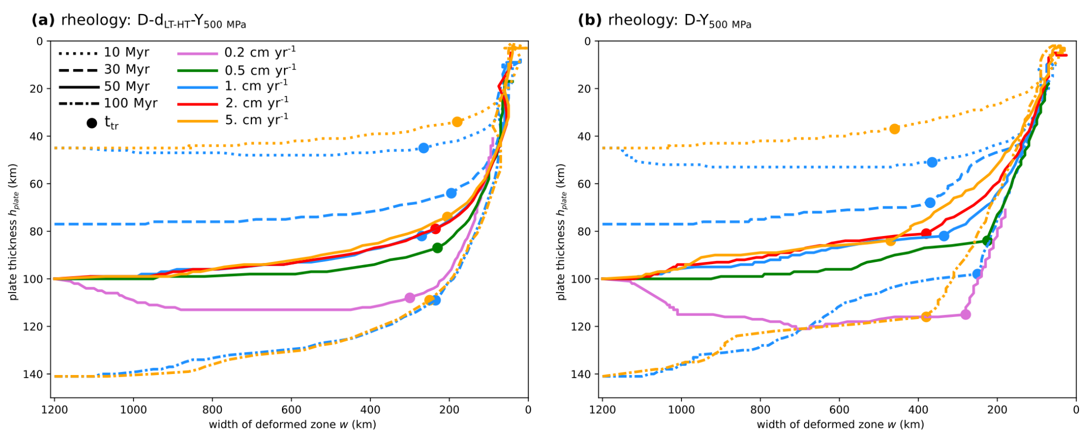

Figure D3. Co-evolution of the ~~highly deforming width $w(t)$ and of the~~ minimum plate thickness ~~h_{plate} (approximating~~ $h_{plate}(t)$ as a function of the ~~evolution~~ width of the ~~deforming lithosphere morphology),~~ most deformed zone $w(t)$ for two rheological combinations~~,~~ ~~when the initial plate age and the half-spreading velocity are varied.~~: (a) ~~Rheology:~~ $D - d_{\mathrm{LT-HT}} - Y_{500\ \mathrm{MPa}}$. (b) ~~Rheolog:~~ $D - Y_{500\ \mathrm{MPa}}$. Curves are shown for varying initial plate age (indicated by line-styles and half-spreading velocity (indicated by colors). The transition times t_{tr} between Stages 1 and 2 are marked by dots.

Appendix E: Simulations with a depth-dependent yield stress

We perform two simulations with a depth-dependent yield stress for the following two creep rheologies : (i) diffusion creep (D), (ii) diffusion creep plus low- and high-temperature dislocation creep (D-$d_{\text{LT-HT}}$). We define a depth-dependent yield stress:

$$\sigma_y(z) = \sigma_0 + z \cdot \Delta\sigma_z \tag{E1}$$

with

$$\Delta\sigma_z = \rho \cdot g \cdot \mu \tag{E2}$$

where z is depth, $\sigma_0 = 50$ MPa is the yield stress at the surface (cohesion), $\Delta\sigma_z$ (Pa m^{-1}) is the yield stress gradient and μ is the yield stress increase with pressure related to the friction coefficient, f_s. The parameter μ corresponds to the ratio between the horizontal tectonic deviatoric stress and the lithostatic pressure (neglecting pore fluid pressure), while the friction coefficient f_s is the ratio between the shear stress and the normal stress acting on a plane fault (e.g., Turcotte and Schubert, 2002; Doin and Henry, 2001) . The yield stress gradients are chosen to ensure that the transition of deformation mechanism from yield to creep corresponds to a stress of approximately 500 MPa and occurs at the same depth as in the case of a constant yield stress with depth. This transition depth depends on the creep law considered. Consequently, for the following creep rheologies: diffusion creep (D) and diffusion creep plus low- to high-temperature dislocation creep $(D - d_{\text{LT-HT}})$, one may get: $\Delta\sigma_z(D) = 6.181$ MPa km^{-1}, $\mu(D) \approx 0.19$ and $\Delta\sigma_z(D - d_{\text{LT-HT}}) = 16.423$ MPa km^{-1}, $\mu(D - d_{\text{LT-HT}}) \approx 0.51$, respectively (Fig. E1), keeping unchanged the depth of the yield-creep transition with respect to a constant yield stress ensures to maintain the rheological structure of the underneath ductile layer in the lithosphere.

The two chosen stress-increase with depth are higher than in commonly used depth-dependent yield stress formulations in large mantle convection simulations (usually lower than 1.1 MPa km^{-1}, e.g. Rolf and Tackley, 2011; Coltice et al., 2019; Arnould et al., 2023) , and corresponds to relatively high friction coefficients (typically lower than 0.2 in convection experiments, e.g. Moresi and Solomatov, 19 and closer to experiment values (~ 0.6, e.g. Byerlee, 1978).

Figure E2 shows that the transition time t_{tr}, the plate boundary time t_{PB} and the overall scenario of localization obtained for a depth-dependent yield stress are very close to the reference cases performed with a constant yield stress, for the two investigated creep rheologies. Tectonic force and the lateral viscosity contrasts are lower and higher, respectively, when comparing a depth-dependent yield stress to a constant yield stress (Fig. E2c and e, at initial state and at time t_{tr}, respectively). Moreover, the free-surface topography is not significantly modified when the yield stress is depth-dependent instead of being constant, except in the noticeable narrow area where the plate boundary forms at the very end of the simulation (Supplement S.3.1).

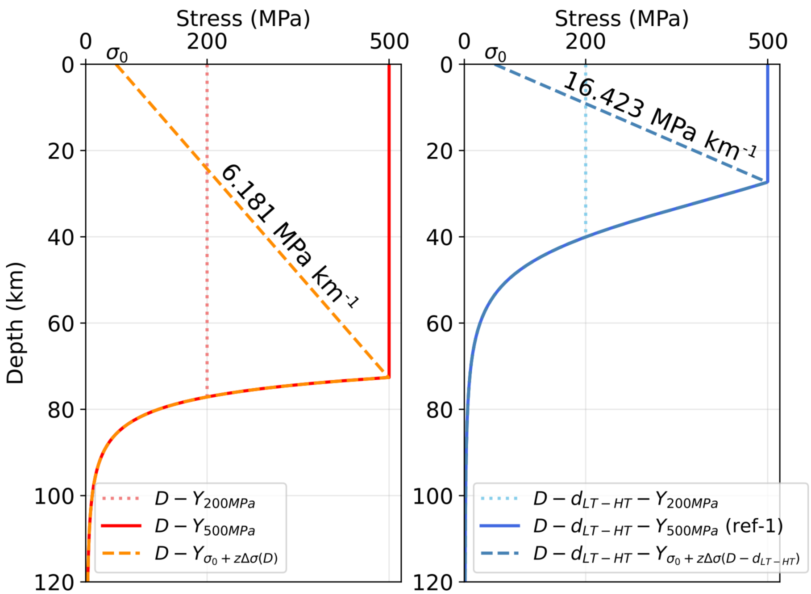

Figure E1. Strength profile computed for a uniform strain rate $\dot{\varepsilon} = 3{\cdot}10^{-15}$ s^{-1} and a temperature profile corresponding to a 50 Myrs-old lithosphere. The red and dark blue curves are respectively: diffusion, and diffusion plus low- and high-temperature dislocation creep rheologies, in combination with a depth-dependent yield stress (dashed lines), or with a constant yield stress of 200 or 500 MPa (orange dotted and light blue solid lines, respectively). The yield-creep transition for the depth-dependent yield stress is reached at a maximum strength of 500 MPa, which is consistent to the yield-creep transition depth for constant yield stress of 500 MPa combinations.

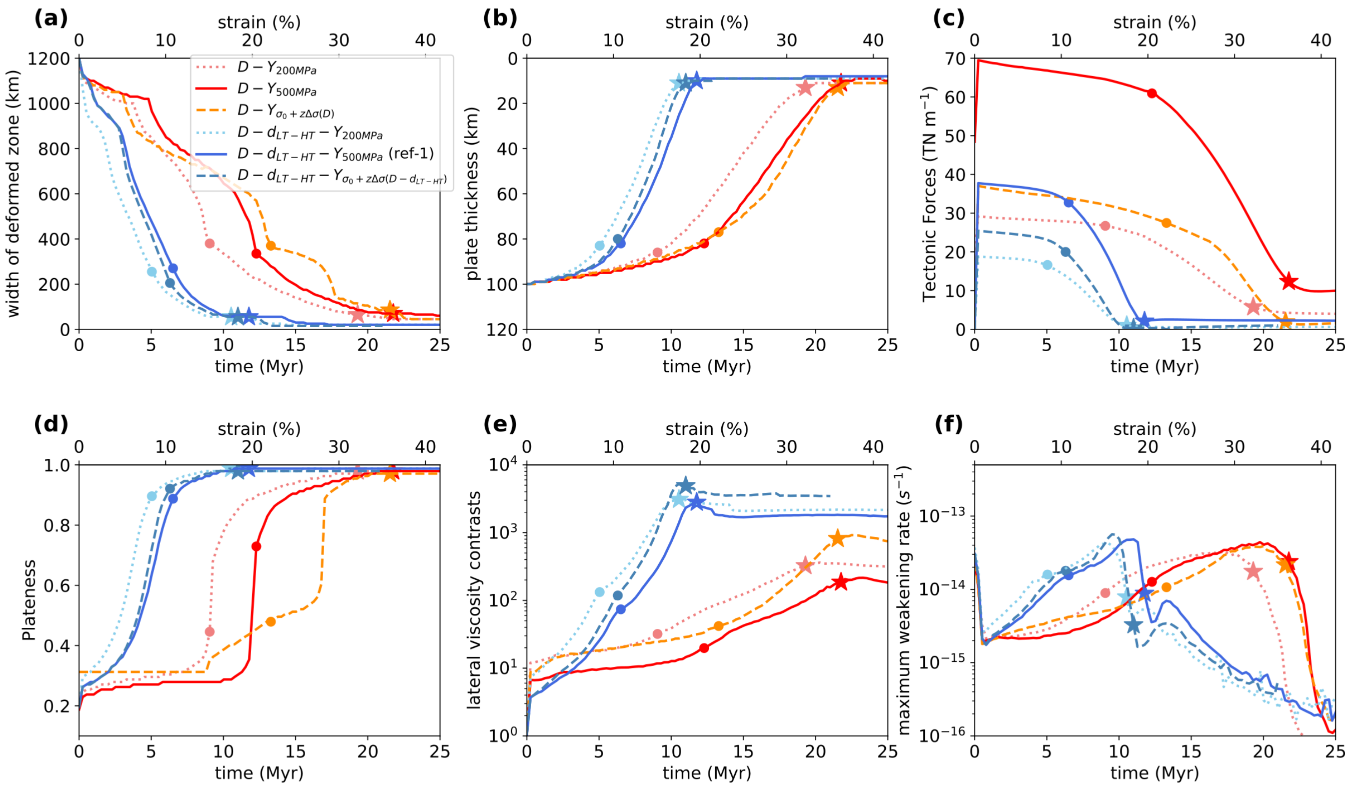

Figure E2. Temporal evolution (and corresponding cumulative strain in %) of diagnostics for two sets of simulations corresponding to two creep viscosities (diffusion creep and diffusion creep with LT-HT dislocation creep). In each set, the yield stress is either constant, and set to 200 or 500 MPa, or increasing with depth. The color and style coding used to caption simulations is the same as in Fig. E1. Note that this figure is a similar representation of diagnostics as Fig. 6) in the main text. Simulations have the same initial plate age (50 Myr) and extension velocity ($v_{1/2}$ = 1 cm yr^{-1}). (a) Width of the enhanced deformed zone w, (b) plate thickness h_{plate} at x = 600 km, (c) tectonic force F, (d) plateness P, (e) lateral viscosity contrast R_{visc}, and (f) maximum weakening rate $W_{\max}$ over the whole lithosphere thickness ($T < 1500$ K) at x = 600 km.

Code and Data availability

The Fluidity computational modeling framework, including source code and documentation, is available from https://fluidityproject.github.io (release 4.1.19, Kramer et al. (2021a)). Post-processing codes were developed using Python (3.11.11) and are available upon request from the corresponding author, with few Figures using scientific color maps of Fabio Crameri. Simulation data supporting the findings of this study are available at https://zenodo.org/records/17606932, including raw files necessary to reproduce the main numerical experiments. Additional simulation outputs not included in the repository are available upon request from the corresponding author.

Author contribution

EVB, FG, and RD designed the numerical experiments; EVB, FG, CT, and DA developed new post-processing diagnostics; EVB developed the codes for simulation analysis; EVB and CT produced the figures; all authors discussed the results and contributed to the writing of the paper; FG supervised the project and coordinated the research.

Competing interests

The authors declare that they have no conflict of interest.

Acknowledgements

The authors ~~thank~~ warmly thank Antonio Manjón-Cabeza Córdoba and Vojtěch Patočka for their constructive reviews, which greatly helped designing additional simulations and strengthen the paper's core messages, as well as M. Arnould, T. Rolf, S. Demouchy, A. Tommasi, N. Coltice, ~~and M. Arnould~~ for fruitful discussions. The numerical simulations were performed using the finite-element control-volume code *Fluidity* code ~~and (~~https://fluidityproject.github.io/), developed and maintained with the support of a large community. This work has been realized with the support of the HPC Platform MESO@LR, funded by the Occitanie/~~Pyrénnées-Méditerranée~~ Pyrénées-Méditerranée Region, Montpellier Mediterranean Metropole and the University of Montpellier, then with the support of ISDM-MESO-Platform at the University of Montpellier.

Financial support

This research was funded by the French National Research Agency (ANR) through the RheoBreak project (grant no. ANR–21-CE49-0009) led by Fanny Garel.

References

Abercrombie, R. E. and Ekström, G.: Earthquake slip on oceanic transform faults, Nature, 410, 74–77, https://doi.org/10.1038/35065064, publisher: Nature Publishing Group, 2001.

Agrusta, R., Tommasi, A., Arcay, D., Gonzalez, A., and Gerya, T.: How partial melting affects small-scale convection in a plume-fed sublithospheric layer beneath fast-moving plates, Geochemistry, Geophysics, Geosystems, 16, 3924–3945, https://doi.org/10.1002/2015GC005967, _eprint: https://agupubs.onlinelibrary.wiley.com/doi/pdf/10.1002/2015GC005967, 2015.

Allemand, P. and Brun, J.-P.: Width of continental rifts and rheological layering of the lithosphere, Tectonophysics, 188, 63–69, https://doi.org/10.1016/0040-1951(91)90314-I, 1991.

Arcay, D., Abecassis, S., and Lallemand, S.: Subduction initiation at an oceanic transform fault experiencing compression: Role of the fault structure and of the brittle-ductile transition depth, Earth and Planetary Science Letters, 618, 118 272, https://doi.org/10.1016/j.epsl.2023.118272, 2023.

Arnould, M., Rolf, T., and Manjón-Cabeza Córdoba, A.: Effects of Composite Rheology on Plate-Like Behavior in Global-Scale Mantle Convection, Geophysical Research Letters, 50, e2023GL104 146, https://doi.org/10.1029/2023GL104146, _eprint: https://agupubs.onlinelibrary.wiley.com/doi/pdf/10.1029/2023GL104146, 2023.

Asti, R., Saspiturry, N., and Angrand, P.: The Mesozoic Iberia-Eurasia diffuse plate boundary: A wide domain of distributed transtensional deformation progressively focusing along the North Pyrenean Zone, Earth-science reviews, 230, 104 040, 2022.

Ballmer, M. D., van Hunen, J., Ito, G., Bianco, T. A., and Tackley, P. J.: Intraplate volcanism with complex age-distance patterns: A case for small-scale sublithospheric convection, Geochemistry, Geophysics, Geosystems, 10, https://doi.org/10.1029/2009GC002386, _eprint: https://agupubs.onlinelibrary.wiley.com/doi/pdf/10.1029/2009GC002386, 2009.

Bercovici, D.: A simple model of plate generation from mantle flow, Geophysical Journal International, 114, 635–650, 1993.

Bercovici, D.: The generation of plate tectonics from mantle convection, Earth and Planetary Science Letters, 205, 107–121, publisher: Elsevier, 2003.

Bercovici, D. and Karato, S.-i.: Theoretical analysis of shear localization in the lithosphere, Reviews in mineralogy and geochemistry, 51, 387–420, publisher: Mineralogical Society of America, 2002.

Bercovici, D. and Ricard, Y.: Generation of plate tectonics with two-phase grain-damage and pinning: Source–sink model and toroidal flow, Earth and Planetary Science Letters, 365, 275–288, publisher: Elsevier, 2013.

Bercovici, D. and Ricard, Y.: Plate tectonics, damage and inheritance, Nature, 508, 513–516, publisher: Nature Publishing Group UK London, 2014.

Bercovici, D., Tackley, P., and Ricard, Y.: 7.07-the generation of plate tectonics from mantle dynamics, Treatise on Geophysics. Elsevier, Oxford, pp. 271–318, 2015.

Bialas, R. W., Buck, W. R., and Qin, R.: How much magma is required to rift a continent?, Earth and Planetary Science Letters, 292, 68–78, https://doi.org/10.1016/j.epsl.2010.01.021, 2010.

Billen, M. I. and Hirth, G.: Newtonian versus non-Newtonian upper mantle viscosity: Implications for subduction initiation, grl, 32, L19 304, https://doi.org/10.1029/2005GL023457, publisher: Wiley Online Library, 2005.

Brun, J. and Cobbold, P.: Strain heating and thermal softening in continental shear zones: a review, Journal of Structural Geology, 2, 149–158, publisher: Elsevier, 1980.

Brune, S., Popov, A. A., and Sobolev, S. V.: Modeling suggests that oblique extension facilitates rifting and continental break-up, Journal of Geophysical Research: Solid Earth, 117, https://doi.org/10.1029/2011JB008860, publisher: John Wiley & Sons, Ltd, 2012.

Brune, S., Popov, A. A., and Sobolev, S. V.: Quantifying the thermo-mechanical impact of plume arrival on continental break-up, Tectonophysics, 604, 51–59, https://doi.org/10.1016/j.tecto.2013.02.009, 2013.

Brune, S., Heine, C., Pérez-Gussinyé, M., and Sobolev, S. V.: Rift migration explains continental margin asymmetry and crustal hyper-extension, Nature Communications, 5, 4014, https://doi.org/10.1038/ncomms5014, 2014.

Brune, S., Williams, S. E., Butterworth, N. P., and Müller, R. D.: Abrupt plate accelerations shape rifted continental margins, Nature, 536, 201–204, https://doi.org/10.1038/nature18319, publisher: Nature Publishing Group, 2016.

Brune, S., Heine, C., Clift, P. D., and Pérez-Gussinyé, M.: Rifted margin architecture and crustal rheology: Reviewing Iberia-Newfoundland, Central South Atlantic, and South China Sea, Marine and Petroleum Geology, 79, 257–281, https://doi.org/10.1016/j.marpetgeo.2016.10.018, 2017.

Brune, S., Kolawole, F., Olive, J.-A., Stamps, D. S., Buck, W. R., Buiter, S. J. H., Furman, T., and Shillington, D. J.: Geodynamics of continental rift initiation and evolution, Nature Reviews Earth & Environment, 4, 235–253, https://doi.org/10.1038/s43017-023-00391-3, number: 4 Publisher: Nature Publishing Group, 2023.

Buck, W. R.: Modes of continental lithospheric extension, Journal of Geophysical Research: Solid Earth, 96, 20 161–20 178, https://doi.org/10.1029/91JB01485, _eprint: https://onlinelibrary.wiley.com/doi/pdf/10.1029/91JB01485, 1991.

Burov, E. and Watts, A.: The long-term strength of continental lithosphere: “jelly sandwich” or “crème brûlée”?, GSA Today, 16, 4, https://doi.org/10.1130/1052-5173(2006)016<4:TLTSOC>2.0.CO;2, 2006.

Burov, E., Watts, A., et al.: The long-term strength of continental lithosphere:" jelly sandwich" or" crème brûlée"?, GSA today, 16, 4, 2006.

Burov, E. B.: Rheology and strength of the lithosphere, Marine and Petroleum Geology, 28, 1402–1443, https://doi.org/10.1016/j.marpetgeo.2011.05.008, 2011a.

Burov, E. B.: Rheology and strength of the lithosphere, Marine and Petroleum Geology, 28, 1402–1443, https://doi.org/10.1016/j.marpetgeo.2011.05.008, 2011b.

Byerlee, J.: Friction of rocks, Pure and Applied Geophysics, 116, 615–626, https://doi.org/10.1007/BF00876528, publisher: Springer, 1978.

Chaboureau, A.-C., Guillocheau, F., Robin, C., Rohais, S., Moulin, M., and Aslanian, D.: Paleogeographic evolution of the central segment of the South Atlantic during Early Cretaceous times: Paleotopographic and geodynamic implications, Tectonophysics, 604, 191–223, https://doi.org/10.1016/j.tecto.2012.08.025, 2013.

Chen, L., Liu, L., Capitanio, F. A., Gerya, T. V., and Li, Y.: The role of pre-existing weak zones in the formation of the Himalaya and Tibetan plateau: 3-D thermomechanical modelling, Geophysical Journal International, 221, 1971–1983, 2020.

Chenin, P., Schmalholz, S. M., Manatschal, G., and Karner, G. D.: Necking of the Lithosphere: A Reappraisal of Basic Concepts With Thermo-Mechanical Numerical Modeling, Journal of Geophysical Research: Solid Earth, 123, 5279–5299, https://doi.org/10.1029/2017JB014155, _eprint: https://onlinelibrary.wiley.com/doi/pdf/10.1029/2017JB014155, 2018.

Coltice, N., Gérault, M., and Ulvrová, M.: A mantle convection perspective on global tectonics, Earth-science reviews, 165, 120–150, publisher: Elsevier, 2017.

Coltice, N., Husson, L., Faccenna, C., and Arnould, M.: What drives tectonic plates?, Science Advances, 5, eaax4295, https://doi.org/10.1126/sciadv.aax4295, publisher: American Association for the Advancement of Science, 2019.

Conrad, C. P. and Lithgow-Bertelloni, C.: How Mantle Slabs Drive Plate Tectonics, Science, 298, 207–209, https://doi.org/10.1126/science.1074161, 2002.

Crameri, F.: Geodynamic diagnostics, scientific visualisation and StagLab 3.0, Geoscientific Model Development, 11, 2541–2562, https://doi.org/10.5194/gmd-11-2541-2018, 2018.

Crameri, F. and Tackley, P. J.: Spontaneous development of arcuate single-sided subduction in global 3-D mantle convection models with a free surface, Journal of Geophysical Research: Solid Earth, 119, 5921–5942, https://doi.org/10.1002/2014JB010939, _eprint: https://agupubs.onlinelibrary.wiley.com/doi/pdf/10.1002/2014JB010939, 2014.

Crameri, F., Tackley, P., Meilick, I., Gerya, T., and Kaus, B.: A free plate surface and weak oceanic crust produce single-sided subduction on Earth, grl, 39, L03 306, https://doi.org/10.1029/2011GL050046, 2012.

Cross, A. J., Prior, D. J., Stipp, M., and Kidder, S.: The recrystallized grain size piezometer for quartz: An EBSD-based calibration, Geophysical Research Letters, 44, 6667–6674, https://doi.org/10.1002/2017GL073836, _eprint: https://onlinelibrary.wiley.com/doi/pdf/10.1002/2017GL073836, 2017.

Dannberg, J., Eilon, Z., Faul, U., Gassmöller, R., Moulik, P., and Myhill, R.: The importance of grain size to mantle dynamics and seismological observations, Geochemistry, Geophysics, Geosystems, 18, 3034–3061, publisher: Wiley Online Library, 2017.

Dannberg, J., Eilon, Z., Russell, J. B., and Gassmöller, R.: Understanding Sub-Lithospheric Small-Scale Convection by Linking Models of Grain Size Evolution, Mantle Convection, and Seismic Tomography, Geochemistry, Geophysics, Geosystems, 26, e2025GC012 289, https://doi.org/10.1029/2025GC012289, _eprint: https://agupubs.onlinelibrary.wiley.com/doi/pdf/10.1029/2025GC012289, 2025.

Davies, D. R., Wilson, C. R., and Kramer, S. C.: Fluidity: A fully unstructured anisotropic adaptive mesh computational modeling framework for geodynamics, Geochemistry, Geophysics, Geosystems, 12, https://doi.org/10.1029/2011GC003551, _eprint: https://onlinelibrary.wiley.com/doi/pdf/10.1029/2011GC003551, 2011.

Demouchy, S., Tommasi, A., Ballaran, T. B., and Cordier, P.: Low strength of Earth's uppermost mantle inferred from tri-axial deformation experiments on dry olivine crystals, Physics of the Earth and Planetary Interiors, 220, 37–49, publisher: Elsevier, 2013.

Demouchy, S., Wang, Q., and Tommasi, A.: Deforming the Upper Mantle—Olivine Mechanical Properties and Anisotropy, Elements, 19, 151–157, https://doi.org/10.2138/gselements.19.3.151, 2023.

Deschamps, A. and Lallemand, S.: The West Philippine Basin: An Eocene to early Oligocene back arc basin opened between two opposed subduction zones, Journal of Geophysical Research: Solid Earth, 107, EPM 1–1–EPM 1–24, https://doi.org/10.1029/2001JB001706, _eprint: https://agupubs.onlinelibrary.wiley.com/doi/pdf/10.1029/2001JB001706, 2002.

Doin, M.-P. and Henry, P.: Subduction initiation and continental crust recycling: the roles of rheology and eclogitization, Tectonophysics, 342, 163–191, 2001.

Duclaux, G., Huismans, R. S., and May, D. A.: Rotation, narrowing, and preferential reactivation of brittle structures during oblique rifting, Earth and Planetary Science Letters, 531, 115 952, 2020.

Duretz, T., de Borst, R., Yamato, P., and Le Pourhiet, L.: Toward robust and predictive geodynamic modeling: The way forward in frictional plasticity, Geophysical Research Letters, 47, e2019GL086 027, 2020.

Duretz, T., de Borst, R., and Yamato, P.: Modeling lithospheric deformation using a compressible visco-elasto-viscoplastic rheology and the effective viscosity approach, Geochemistry, Geophysics, Geosystems, 22, e2021GC009 675, 2021.

Duretz, T., Schmalholz, S. M., Kulakov, R., Mohn, G., Tugend, J., Halter, W., and Bardroff, A.: Lithospheric deformation with mechanical anisotropy: A numerical model and application to continental rifting, Geochemistry, Geophysics, Geosystems, 26, e2025GC012 409, 2025.

Duvernay, T., Davies, D. R., Mathews, C. R., Gibson, A. H., and Kramer, S. C.: Continental Magmatism: The Surface Manifestation of Dynamic Interactions Between Cratonic Lithosphere, Mantle Plumes and Edge-Driven Convection, Geochemistry, Geophysics, Geosystems, 23, e2022GC010 363, https://doi.org/10.1029/2022GC010363, _eprint: https://agupubs.onlinelibrary.wiley.com/doi/pdf/10.1029/2022GC010363, 2022.

Engeln, J. F., Wiens, D. A., and Stein, S.: Mechanisms and depths of Atlantic transform earthquakes, Journal of Geophysical Research: Solid Earth, 91, 548–577, https://doi.org/10.1029/JB091iB01p00548, _eprint: https://agupubs.onlinelibrary.wiley.com/doi/pdf/10.1029/JB091iB01p00548, 1986.

Evans, B. and Goetze, C.: The temperature variation of hardness of olivine and its implication for polycrystalline yield stress/, Journal of Geophysical Research: Solid Earth, 84, 5505–5524, publisher: Wiley Online Library, 1979.

Fleitout, L. and Froidevaux, C.: Thermal and mechanical evolution of shear zones, Journal of Structural Geology, 2, 159–164, publisher: Elsevier, 1980.

Foley, B. J. and Bercovici, D.: Scaling laws for convection with temperature-dependent viscosity and grain-damage, Geophysical Journal International, 199, 580–603, 2014.

Frederiksen, S. and Braun, J.: Numerical modelling of strain localisation during extension of the continental lithosphere, Earth and Planetary Science Letters, 188, 241–251, https://doi.org/10.1016/S0012-821X(01)00323-5, 2001.

Frost, H. J. and Ashby, M. F.: Deformation mechanism maps: the plasticity and creep of metals and ceramics, Pergamon press, 1982.

Fuchs, L. and Becker, T. W.: Role of strain-dependent weakening memory on the style of mantle convection and plate boundary stability, Geophysical Journal International, 218, 601–618, publisher: Oxford University Press, 2019.

Fuchs, L. and Becker, T. W.: Deformation memory in the lithosphere: A comparison of damage-dependent weakening and grain-size sensitive rheologies, Journal of Geophysical Research: Solid Earth, 126, e2020JB020 335, publisher: Wiley Online Library, 2021.

Fuchs, L. and Becker, T. W.: On the Role of Rheological Memory for Convection-Driven Plate Reorganizations, Geophysical Research Letters, 49, e2022GL099 574, publisher: Wiley Online Library, 2022.

Garel, F. and Thoraval, C.: Lithosphere as a constant-velocity plate: Chasing a dynamical LAB in a homogeneous mantle material, Physics of the Earth and Planetary Interiors, p. 106710, publisher: Elsevier, 2021.

Garel, F., Goes, S., Davies, D. R., Davies, J. H., Kramer, S. C., and Wilson, C. R.: Interaction of subducted slabs with the mantle transition-zone: A regime diagram from 2-D thermo-mechanical models with a mobile trench and an overriding plate, Geochemistry, Geophysics, Geosystems, 15, 1739–1765, https://doi.org/10.1002/2014GC005257, _eprint: https://onlinelibrary.wiley.com/doi/pdf/10.1002/2014GC005257, 2014.

Garel, F., Thoraval, C., Tommasi, A., Demouchy, S., and Davies, D. R.: Using thermo-mechanical models of subduction to constrain effective mantle viscosity, Earth and Planetary Science Letters, 539, 116 243, https://doi.org/10.1016/j.epsl.2020.116243, 2020.

Gerya, T.: Large-scale-long-term Strength of the Lithosphere: New Theory and Applications, Petrology, 32, 128–141, 2024.

Gleason, G. C. and Tullis, J.: A flow law for dislocation creep of quartz aggregates determined with the molten salt cell, Tectonophysics, 247, 1–23, https://doi.org/10.1016/0040-1951(95)00011-B, 1995.

Gouriet, K., Cordier, P., Garel, F., Thoraval, C., Demouchy, S., Tommasi, A., and Carrez, P.: Dislocation dynamics modelling of the power-law breakdown in olivine single crystals: Toward a unified creep law for the upper mantle, Earth and Planetary Science Letters, 506, 282–291, https://doi.org/10.1016/j.epsl.2018.10.049, 2019.

Gueydan, F. and Précigout, J.: Modes of continental rifting as a function of ductile strain localization in the lithospheric mantle, Tectonophysics, 612-613, 18–25, https://doi.org/10.1016/j.tecto.2013.11.029, 2014.

Gueydan, F., Morency, C., and Brun, J.-P.: Continental rifting as a function of lithosphere mantle strength, Tectonophysics, 460, 83–93, https://doi.org/10.1016/j.tecto.2008.08.012, 2008.

Gueydan, F., Précigout, J., and Montesi, L. G.: Strain weakening enables continental plate tectonics, Tectonophysics, 631, 189–196, publisher: Elsevier, 2014.

Gurnis, M., Hall, C., and Lavier, L.: Evolving force balance during incipient subduction, Geochemistry, Geophysics, Geosystems, 5, https://doi.org/10.1029/2003GC000681, _eprint: https://agupubs.onlinelibrary.wiley.com/doi/pdf/10.1029/2003GC000681, 2004.

Hansen, L. N., Kumamoto, K. M., Thom, C. A., Wallis, D., Durham, W. B., Goldsby, D. L., Breithaupt, T., Meyers, C. D., and Kohlstedt, D. L.: Low-temperature plasticity in olivine: Grain size, strain hardening, and the strength of the lithosphere, Journal of Geophysical Research: Solid Earth, 124, 5427–5449, 2019.

Heckenbach, E. L., Brune, S., Glerum, A. C., and Bott, J.: Is There a Speed Limit for the Thermal Steady-State Assumption in Continental Rifts?, Geochemistry, Geophysics, Geosystems, 22, e2020GC009 577, https://doi.org/10.1029/2020GC009577, _eprint: https://onlinelibrary.wiley.com/doi/pdf/10.1029/2020GC009577, 2021.

Heron, P. J., Pysklywec, R. N., and Stephenson, R.: Identifying mantle lithosphere inheritance in controlling intraplate orogenesis, Journal of Geophysical Research: Solid Earth, 121, 6966–6987, 2016.

Hirschmann, M. M.: Mantle solidus: Experimental constraints and the effects of peridotite composition, Geochemistry, Geophysics, Geosystems, 1, https://doi.org/10.1029/2000GC000070, _eprint: https://agupubs.onlinelibrary.wiley.com/doi/pdf/10.1029/2000GC000070, 2000.

Hirth, G. and Kohlstedt, D. L.: Experimental constraints on the dynamics of the partially molten upper mantle: Deformation in the diffusion creep regime, Journal of Geophysical Research: Solid Earth, 100, 1981–2001, publisher: Wiley Online Library, 1995a.

Hirth, G. and Kohlstedt, D. L.: Experimental constraints on the dynamics of the partially molten upper mantle: 2. Deformation in the dislocation creep regime, Journal of Geophysical Research: Solid Earth, 100, 15 441–15 449, publisher: Wiley Online Library, 1995b.

Huismans, R. S. and Beaumont, C.: Symmetric and asymmetric lithospheric extension: Relative effects of frictional-plastic and viscous strain softening, Journal of Geophysical Research: Solid Earth, 108, https://doi.org/10.1029/2002JB002026, _eprint: https://onlinelibrary.wiley.com/doi/pdf/10.1029/2002JB002026, 2003.

Huismans, R. S. and Beaumont, C.: Effect of lithospheric stratification on extensional styles and rift basin geometry, 2005.

Huismans, R. S. and Beaumont, C.: Roles of lithospheric strain softening and heterogeneity in determining the geometry of rifts and continental margins, Geological Society, London, Special Publications, 282, 111–138, https://doi.org/10.1144/SP282.6, publisher: The Geological Society of London, 2007.

Iaffaldano, G.: The strength of large-scale plate boundaries: Constraints from the dynamics of the Philippine Sea plate since 5Ma, epsl, 357, 21–30, https://doi.org/10.1016/j.epsl.2012.09.018, publisher: Elsevier, 2012.

Iaffaldano, G., Davies, D. R., and DeMets, C.: Indian Ocean floor deformation induced by the Reunion plume rather than the Tibetan Plateau, Nature Geoscience, 11, 362–366, https://doi.org/10.1038/s41561-018-0110-z, publisher: Nature Publishing Group, 2018.

Jain, C., Korenaga, J., and Karato, S.-i.: On the Yield Strength of Oceanic Lithosphere, Geophysical Research Letters, 44, 9716–9722, https://doi.org/10.1002/2017GL075043, _eprint: https://agupubs.onlinelibrary.wiley.com/doi/pdf/10.1002/2017GL075043, 2017.

Janin, A., Coltice, N., Chamot-Rooke, N., and Tierny, J.: Geodynamics of a global plate reorganization from topological data analysis, Nature Geoscience, pp. 1–7, https://doi.org/10.1038/s41561-025-01772-7, publisher: Nature Publishing Group, 2025.

Jolivet, L., Tamaki, K., and Fournier, M.: Japan Sea, opening history and mechanism: A synthesis, Journal of Geophysical Research: Solid Earth, 99, 22 237–22 259, https://doi.org/10.1029/93JB03463, _eprint: https://agupubs.onlinelibrary.wiley.com/doi/pdf/10.1029/93JB03463, 1994.

Karato, S.-i.: Deformation of earth materials: an introduction to the rheology of solid earth, Cambridge University Press, 2008.

Kaus, B. J. and Podladchikov, Y. Y.: Initiation of localized shear zones in viscoelastoplastic rocks, Journal of Geophysical Research: Solid Earth, 111, publisher: Wiley Online Library, 2006.

Kawazoe, T., Karato, S.-i., Otsuka, K., Jing, Z., and Mookherjee, M.: Shear deformation of dry polycrystalline olivine under deep upper mantle conditions using a rotational Drickamer apparatus (RDA), pepi, 174, 128–137, https://doi.org/10.1016/j.pepi.2008.06.027, publisher: Elsevier, 2009.

Kiss, D., Podladchikov, Y., Duretz, T., and Schmalholz, S. M.: Spontaneous generation of ductile shear zones by thermal softening: Localization criterion, 1D to 3D modelling and application to the lithosphere, Earth and Planetary Science Letters, 519, 284–296, https://doi.org/10.1016/j.epsl.2019.05.026, 2019.

Kiss, D., Candioti, L. G., Duretz, T., and Schmalholz, S. M.: Thermal softening induced subduction initiation at a passive margin, Geophysical Journal International, 220, 2068–2073, https://doi.org/10.1093/gji/ggz572, 2020.

Kohli, A., Wolfson-Schwehr, M., Prigent, C., and Warren, J. M.: Oceanic transform fault seismicity and slip mode influenced by seawater infiltration, Nature Geoscience, 14, 606–611, 2021.

Kohlstedt, D. L., Evans, B., and Mackwell, S. J.: Strength of the lithosphere: Constraints imposed by laboratory experiments, Journal of Geophysical Research: Solid Earth, 100, 17 587–17 602, https://doi.org/10.1029/95JB01460, _eprint: https://onlinelibrary.wiley.com/doi/pdf/10.1029/95JB01460, 1995.

Korenaga, J.: Scaling of plate tectonic convection with pseudoplastic rheology, Journal of Geophysical Research: Solid Earth, 115, 2010.

Korenaga, J. and Karato, S.-I.: A new analysis of experimental data on olivine rheology, jgr, 113, B02 403, https://doi.org/10.1029/2007JB005100, publisher: Wiley Online Library, 2008.

Kramer, S., Greaves, T., Funke, S. W., Wilson, C., Avdis, A., Davies, R., Lange, M., Chris, Candy, A., Cotter, C. J., Percival, J., Mouradian, S., Bhutani, G., Gibson, A., Gorman, G., Duvernay, T., Guo, X., Maddison, J. R., Rathgeber, F., Weiland, M., gnikit, Robinson, D., markgoffin, Piggott, M., applet199, Dargaville, S., Everett, A., Jacobs, C. T., Cavendish, A. B., and Ham, D. A.: FluidityProject/fluidity: Zenodo Release, https://doi.org/10.5281/zenodo.5221157, 2021a.

Kramer, S. C., Wilson, C. R., and Davies, D. R.: An implicit free surface algorithm for geodynamical simulations, Physics of the Earth and Planetary Interiors, 194-195, 25–37, https://doi.org/10.1016/j.pepi.2012.01.001, 2012.

Kramer, S. C., Davies, D. R., and Wilson, C. R.: Analytical solutions for mantle flow in cylindrical and spherical shells, Geoscientific Model Development, 14, 1899–1919, 2021b.

Kreemer, C., Blewitt, G., and Klein, E. C.: A geodetic plate motion and Global Strain Rate Model, Geochemistry, Geophysics, Geosystems, 15, 3849–3889, https://doi.org/10.1002/2014GC005407, _eprint: https://agupubs.onlinelibrary.wiley.com/doi/pdf/10.1002/2014GC005407, 2014.

Lallemand, S. and Arcay, D.: Subduction initiation from the earliest stages to self-sustained subduction: Insights from the analysis of 70 Cenozoic sites, Earth-Science Reviews, 221, 103 779, https://doi.org/10.1016/j.earscirev.2021.103779, 2021.

Lamb, S. and Watts, A.: The origin of mountains–implications for the behaviour of Earth's lithosphere, Current Science, pp. 1699–1718, 2010.

Le Pichon, X.: Sea-floor spreading and continental drift, Journal of Geophysical Research (1896-1977), 73, 3661–3697, https://doi.org/10.1029/JB073i012p03661, _eprint: https://agupubs.onlinelibrary.wiley.com/doi/pdf/10.1029/JB073i012p03661, 1968.

Le Voci, G., Davies, D. R., Goes, S., Kramer, S. C., and Wilson, C. R.: A systematic 2-D investigation into the mantle wedge's transient flow regime and thermal structure: complexities arising from buoyancy and a hydrated rheology, Geochem. Geophys. Geosys., p. In Press., https://doi.org/10.1002/2013GC005022, 2014.

Li, Y. and Gurnis, M.: Rapid shear zone weakening during subduction initiation, Proceedings of the National Academy of Sciences, 121, e2404939 121, https://doi.org/10.1073/pnas.2404939121, publisher: Proceedings of the National Academy of Sciences, 2024.

Mallard, C., Coltice, N., Seton, M., Müller, R. D., and Tackley, P. J.: Subduction controls the distribution and fragmentation of Earth's tectonic plates, Nature, 535, 140–143, https://doi.org/10.1038/nature17992, number: 7610 Publisher: Nature Publishing Group, 2016.

Mameri, L., Tommasi, A., Signorelli, J., and Hassani, R.: Olivine-induced viscous anisotropy in fossil strike-slip mantle shear zones and associated strain localization in the crust, Geophysical Journal International, 224, 608–625, publisher: Oxford University Press, 2021.

Martinez, F. and Taylor, B.: Mantle wedge control on back-arc crustal accretion, Nature, 416, 417–420, https://doi.org/10.1038/416417a, publisher: Nature Publishing Group, 2002.

Martínez, F., Fryer, P., Baker, N. A., and Yamazaki, T.: Evolution of backarc rifting: Mariana Trough, 20°–24°N, Journal of Geophysical Research: Solid Earth, 100, 3807–3827, https://doi.org/10.1029/94JB02466, _eprint: https://agupubs.onlinelibrary.wiley.com/doi/pdf/10.1029/94JB02466, 1995.

Mazzotti, S. and Gueydan, F.: Control of tectonic inheritance on continental intraplate strain rate and seismicity, Tectonophysics, 746, 602–610, https://doi.org/10.1016/j.tecto.2017.12.014, 2018.

McKenzie, D., Jackson, J., and Priestley, K.: Thermal structure of oceanic and continental lithosphere, Earth and Planetary Science Letters, 233, 337–349, publisher: Elsevier, 2005.

Mei, S., Suzuki, A., Kohlstedt, D., Dixon, N., and Durham, W.: Experimental constraints on the strength of the lithospheric mantle, jgr, 115, B08 204, https://doi.org/10.1029/2009JB006873, 2010.

Meyer, G. G., Brantut, N., Mitchell, T. M., and Meredith, P. G.: Fault reactivation and strain partitioning across the brittle-ductile transition, Geology, 47, 1127–1130, 2019.

Meyer, S. E., Kaus, B. J. P., and Passchier, C.: Development of branching brittle and ductile shear zones: A numerical study, Geochemistry, Geophysics, Geosystems, 18, 2054–2075, https://doi.org/10.1002/2016GC006793, _eprint: https://onlinelibrary.wiley.com/doi/pdf/10.1002/2016GC006793, 2017.

Mohn, G., Karner, G. D., Manatschal, G., and Johnson, C. A.: Structural and stratigraphic evolution of the Iberia–Newfoundland hyper-extended rifted margin: a quantitative modelling approach, Geological Society, London, Special Publications, 413, 53–89, https://doi.org/10.1144/SP413.9, 2015.

Montési, L. G.: Fabric development as the key for forming ductile shear zones and enabling plate tectonics, Journal of Structural Geology, 50, 254–266, https://doi.org/10.1016/j.jsg.2012.12.011, 2013.

Montési, L. G. J. and Zuber, M. T.: A unified description of localization for application to large-scale tectonics, Journal of Geophysical Research: Solid Earth, 107, ECV 1–1–ECV 1–21, https://doi.org/10.1029/2001JB000465, _eprint: https://onlinelibrary.wiley.com/doi/pdf/10.1029/2001JB000465, 2002.

Moresi, L. and Solomatov, V.: Mantle convection with a brittle lithosphere: thoughts on the global tectonic styles of the Earth and Venus, Geophysical Journal International, 133, 669–682, https://doi.org/10.1046/j.1365-246X.1998.00521.x, 1998.

Morra, G., Seton, M., Quevedo, L., and Müller, R. D.: Organization of the tectonic plates in the last 200 Myr, Earth and Planetary Science Letters, 373, 93–101, https://doi.org/10.1016/j.epsl.2013.04.020, 2013.

Mulyukova, E. and Bercovici, D.: The generation of plate tectonics from grains to global scales: A brief review, Tectonics, 38, 4058–4076, publisher: Wiley Online Library, 2019.

Müller, R. D., Zahirovic, S., Williams, S. E., Cannon, J., Seton, M., Bower, D. J., Tetley, M. G., Heine, C., Le Breton, E., Liu, S., Russell, S. H. J., Yang, T., Leonard, J., and Gurnis, M.: A Global Plate Model Including Lithospheric Deformation

Along Major Rifts and Orogens Since the Triassic, Tectonics, 38, 1884–1907, https://doi.org/10.1029/2018TC005462, _eprint: https://agupubs.onlinelibrary.wiley.com/doi/pdf/10.1029/2018TC005462, 2019.

Nakagawa, T. and Iwamori, H.: Long-Term Stability of Plate-Like Behavior Caused by Hydrous Mantle Convection and Water Absorption in the Deep Mantle, Journal of Geophysical Research: Solid Earth, 122, 8431–8445, https://doi.org/10.1002/2017JB014052, _eprint: https://onlinelibrary.wiley.com/doi/pdf/10.1002/2017JB014052, 2017.

Okino, K., Kasuga, S., and Ohara, Y.: A New Scenario of the Parece Vela Basin Genesis, Marine Geophysical Researches, 20, 21–40, https://doi.org/10.1023/A:1004377422118, company: Springer Distributor: Springer Institution: Springer Label: Springer Publisher: Kluwer Academic Publishers, 1998.

Olive, J.-A., Behn, M. D., Mittelstaedt, E., Ito, G., and Klein, B. Z.: The role of elasticity in simulating long-term tectonic extension, Geophysical Journal International, 205, 728–743, 2016.

Parsons, B. and Richter, F. M.: A relation between the driving force and geoid anomaly associated with mid-ocean ridges, Earth and Planetary Science Letters, 51, 445–450, https://doi.org/10.1016/0012-821X(80)90223-X, 1980.

Patočka, V., Čížková, H., and Tackley, P.: Do elasticity and a free surface affect lithospheric stresses caused by upper-mantle convection?, Geophysical Journal International, 216, 1740–1760, 2019.

Patočka, V., Čížková, H., and Pokorný, J.: Dynamic Component of the Asthenosphere: Lateral Viscosity Variations Due To Dislocation Creep at the Base of Oceanic Plates, Geophysical Research Letters, 51, e2024GL109 116, https://doi.org/10.1029/2024GL109116, _eprint: https://agupubs.onlinelibrary.wiley.com/doi/pdf/10.1029/2024GL109116, 2024.

Petit, L., Olive, J.-A., Schubnel, A., Le Pourhiet, L., and Bhat, H. S.: A brittle constitutive law for long-term tectonic modeling based on sub-critical crack growth, Geochemistry, Geophysics, Geosystems, 25, e2023GC011 229, 2024.

Precigout, J., Gueydan, F., Gapais, D., Garrido, C. J., and Essaifi, A.: Strain localisation in the subcontinental mantle — a ductile alternative to the brittle mantle, Tectonophysics, 445, 318–336, https://doi.org/10.1016/j.tecto.2007.09.002, 2007.

Pérez-Gussinyé, M.: A tectonic model for hyperextension at magma-poor rifted margins: an example from the West Iberia–Newfoundland conjugate margins, Geological Society, London, Special Publications, 369, 403–427, https://doi.org/10.1144/SP369.19, 2013.

Pérez-Gussinyé, M. and Liu, Z.: Continental Rifted Margins 1: Definition and Methodology, Wiley, 1 edn., ISBN 978-1-78945-061-3 978-1-119-98692-8, https://doi.org/10.1002/9781119986928, 2022.

Pérez-Gussinyé, M., Morgan, J. P., Reston, T. J., and Ranero, C. R.: The rift to drift transition at non-volcanic margins: Insights from numerical modelling, Earth and Planetary Science Letters, 244, 458–473, https://doi.org/10.1016/j.epsl.2006.01.059, 2006.

Ranalli, G. and Murphy, D. C.: Rheological stratification of the lithosphere, Tectonophysics, 132, 281–295, https://doi.org/10.1016/0040-1951(87)90348-9, 1987.

Raterron, P., Wu, Y., Weidner, D. J., and Chen, J.: Low-temperature olivine rheology at high pressure, Physics of the Earth and Planetary Interiors, 145, 149–159, 2004.

Richards, M. A., Yang, W.-S., Baumgardner, J. R., and Bunge, H.-P.: Role of a low-viscosity zone in stabilizing plate tectonics: Implications for comparative terrestrial planetology, Geochemistry, Geophysics, Geosystems, 2, 2001.

Rolf, T. and Tackley, P. J.: Focussing of stress by continents in 3D spherical mantle convection with self-consistent plate tectonics, Geophysical Research Letters, 38, https://doi.org/10.1029/2011GL048677, _eprint: https://onlinelibrary.wiley.com/doi/pdf/10.1029/2011GL048677, 2011.

Rolf, T., Coltice, N., and Tackley, P. J.: Linking continental drift, plate tectonics and the thermal state of the Earth's mantle, Earth and Planetary Science Letters, 351-352, 134–146, https://doi.org/10.1016/j.epsl.2012.07.011, 2012.

Rosenbaum, G., Regenauer-Lieb, K., and Weinberg, R. F.: Interaction between mantle and crustal detachments: A nonlinear system controlling lithospheric extension, Journal of Geophysical Research: Solid Earth, 115, 2010.

Ruh, J. B., Tokle, L., and Behr, W. M.: Grain-size-evolution controls on lithospheric weakening during continental rifting, Nature Geoscience, 15, 585–590, publisher: Nature Publishing Group UK London, 2022.

Rybacki, E. and Dresen, G.: Deformation mechanism maps for feldspar rocks, Tectonophysics, 382, 173–187, https://doi.org/10.1016/j.tecto.2004.01.006, 2004.

Rybacki, E., Gottschalk, M., Wirth, R., and Dresen, G.: Influence of water fugacity and activation volume on the flow properties of fine-grained anorthite aggregates, Journal of Geophysical Research: Solid Earth, 111, https://doi.org/10.1029/2005JB003663, _eprint: https://onlinelibrary.wiley.com/doi/pdf/10.1029/2005JB003663, 2006.

Schellart, W. P.: Quantifying the net slab pull force as a driving mechanism for plate tectonics, Geophysical Research Letters, 31, https://doi.org/10.1029/2004GL019528, _eprint: https://agupubs.onlinelibrary.wiley.com/doi/pdf/10.1029/2004GL019528, 2004.

Schierjott, J. C., Thielmann, M., Rozel, A. B., Golabek, G. J., and Gerya, T. V.: Can grain size reduction initiate transform faults?—insights from a 3-D numerical study, Tectonics, 39, e2019TC005 793, publisher: Wiley Online Library, 2020.

Schmalholz, S. M. and Fletcher, R. C.: The exponential flow law applied to necking and folding of a ductile layer, Geophysical Journal International, 184, 83–89, https://doi.org/10.1111/j.1365-246X.2010.04846.x, 2011.

Schmalholz, S. M., Medvedev, S., Lechmann, S. M., and Podladchikov, Y.: Relationship between tectonic overpressure, deviatoric stress, driving force, isostasy and gravitational potential energy, Geophysical Journal International, 197, 680–696, 2014.

Sdrolias, M. and Müller, R. D.: Controls on back-arc basin formation, Geochemistry, Geophysics, Geosystems, 7, https://doi.org/10.1029/2005GC001090, _eprint: https://agupubs.onlinelibrary.wiley.com/doi/pdf/10.1029/2005GC001090, 2006.

Semple, A. G. and Lenardic, A.: Feedbacks between a non-Newtonian upper mantle, mantle viscosity structure and mantle dynamics, Geophysical Journal International, 224, 961–972, https://doi.org/10.1093/gji/ggaa495, 2021.

Solomatov, V.: Scaling of temperature-and stress-dependent viscosity convection, Physics of Fluids, 7, 266–274, publisher: AIP, 1995.

Solomatov, V. S.: Initiation of subduction by small-scale convection, Journal of Geophysical Research: Solid Earth, 109, https://doi.org/10.1029/2003JB002628, _eprint: https://onlinelibrary.wiley.com/doi/pdf/10.1029/2003JB002628, 2004.

Solomatov, V. S. and Moresi, L.-N.: Three regimes of mantle convection with non-Newtonian viscosity and stagnant lid convection on the terrestrial planets, Geophysical Research Letters, 24, 1907–1910, https://doi.org/10.1029/97GL01682, _eprint: https://agupubs.onlinelibrary.wiley.com/doi/pdf/10.1029/97GL01682, 1997.

Tackley, P. J.: Self-consistent generation of tectonic plates in three-dimensional mantle convection, Earth and Planetary Science Letters, 157, 9–22, https://doi.org/10.1016/S0012-821X(98)00029-6, 1998.

Tackley, P. J.: Self-consistent generation of tectonic plates in time-dependent, three-dimensional mantle convection simulations 1 Pseudoplastic yielding, Geochemistry, Geophysics, Geosystems, 1, https://doi.org/10.1029/2000GC000036, _eprint: https://onlinelibrary.wiley.com/doi/pdf/10.1029/2000GC000036, 2000a.

Tackley, P. J.: Self-consistent generation of tectonic plates in time-dependent, three-dimensional mantle convection simulations 2. Strain weakening and asthenosphere, Geochemistry, Geophysics, Geosystems, 1, https://doi.org/10.1029/2000GC000043, _eprint: https://onlinelibrary.wiley.com/doi/pdf/10.1029/2000GC000043, 2000b.

Tarayoun, A., Mazzotti, S., and Gueydan, F.: Quantitative impact of structural inheritance on present-day deformation and seismicity concentration in intraplate deformation zones, Earth and Planetary Science Letters, 518, 160–171, https://doi.org/10.1016/j.epsl.2019.04.043, 2019.

Taylor, B., Zellmer, K., Martinez, F., and Goodliffe, A.: Sea-floor spreading in the Lau back-arc basin, Earth and Planetary Science Letters, 144, 35–40, https://doi.org/10.1016/0012-821X(96)00148-3, 1996.

Tetreault, J. L. and Buiter, S. J. H.: The influence of extension rate and crustal rheology on the evolution of passive margins from rifting to break-up, Tectonophysics, 746, 155–172, https://doi.org/10.1016/j.tecto.2017.08.029, 2018.

Thielmann, M. and Kaus, B. J.: Shear heating induced lithospheric-scale localization: Does it result in subduction?, Earth and Planetary Science Letters, 359, 1–13, publisher: Elsevier, 2012.

Thoraval, C., Tommasi, A., and Doin, M.-P.: Plume-lithosphere interaction beneath a fast moving plate, Geophysical research letters, 33, publisher: Wiley Online Library, 2006.

Tommasi, A., Knoll, M., Vauchez, A., Signorelli, J. W., Thoraval, C., and Logé, R.: Structural reactivation in plate tectonics controlled by olivine crystal anisotropy, Nature Geoscience, 2, 423–427, publisher: Nature Publishing Group UK London, 2009.

Toth, J. and Gurnis, M.: Dynamics of subduction initiation at preexisting fault zones, Journal of Geophysical Research: Solid Earth, 103, 18 053–18 067, https://doi.org/10.1029/98JB01076, _eprint: https://agupubs.onlinelibrary.wiley.com/doi/pdf/10.1029/98JB01076, 1998.

Trompert, R. and Hansen, U.: Mantle convection simulations with rheologies that generate plate-like behaviour, Nature, 395, 686–689, https://doi.org/10.1038/27185, publisher: Nature Publishing Group, 1998.

Tucholke, B., Sibuet, J.-C., and Klaus, A., eds.: Proceedings of the Ocean Drilling Program, 210 Scientific Results, vol. 210 of *Proceedings of the Ocean Drilling Program*, Ocean Drilling Program, https://doi.org/10.2973/odp.proc.sr.210.2007, 2006.

Tucholke, B. E., Sawyer, D. S., and Sibuet, J.-C.: Breakup of the Newfoundland–Iberia rift, Geological Society, London, Special Publications, 282, 9–46, https://doi.org/10.1144/SP282.2, 2007.

Turcotte, D. L. and Schubert, G.: Geodynamics, Cambridge University Press, New York, second edn., 2002.

Ueda, K., Gerya, T., and Sobolev, S. V.: Subduction initiation by thermal–chemical plumes: Numerical studies, Physics of the Earth and Planetary Interiors, 171, 296–312, https://doi.org/10.1016/j.pepi.2008.06.032, 2008.

Ulvrova, M. M., Brune, S., and Williams, S.: Breakup Without Borders: How Continents Speed Up and Slow Down During Rifting, Geophysical Research Letters, 46, 1338–1347, https://doi.org/10.1029/2018GL080387, _eprint: https://onlinelibrary.wiley.com/doi/pdf/10.1029/2018GL080387, 2019.

Van Heck, H. and Tackley, P.: Planforms of self-consistently generated plates in 3D spherical geometry, Geophysical Research Letters, 35, 2008.

Wang, Q.: Homologous temperature of olivine: Implications for creep of the upper mantle and fabric transitions in olivine, Science China Earth Sciences, 59, 1138–1156, https://doi.org/10.1007/s11430-016-5310-z, company: Springer Distributor: Springer Institution: Springer Label: Springer Publisher: Science China Press, 2016.

Wang, Z., Li, J., Feng, Z., Wang, L., and Liu, C.: Mechanism of Structure Variations at Rifted Margins in the Central Segment of South Atlantic: Insights from Numerical Modeling, Acta Geologica Sinica-English Edition, 97, 1229–1242, 2023.

Warren, J. M. and Hansen, L. N.: Ductile deformation of the lithospheric mantle, Annual Review of Earth and Planetary Sciences, 51, 581–609, 2023.

Watremez, L., Burov, E., d'Acremont, E., Leroy, S., Huet, B., Le Pourhiet, L., and Bellahsen, N.: Buoyancy and localizing properties of continental mantle lithosphere: Insights from thermomechanical models of the eastern Gulf of Aden, Geochemistry, Geophysics, Geosystems, 14, 2800–2817, https://doi.org/10.1002/ggge.20179, _eprint: https://onlinelibrary.wiley.com/doi/pdf/10.1002/ggge.20179, 2013.

Weinstein, S. A. and Olson, P. L.: Thermal convection with non-Newtonian plates, Geophysical Journal International, 111, 515–530, https://doi.org/10.1111/j.1365-246X.1992.tb02109.x, 1992.

Whitney, D. L., Delph, J. R., Thomson, S. N., Beck, S. L., Brocard, G. Y., Cosca, M. A., Darin, M. H., Kaymakci, N., Meijers, M. J., Okay, A. I., et al.: Breaking plates: Creation of the East Anatolian fault, the Anatolian plate, and a tectonic escape system, Geology, 51, 673–677, 2023.

Wilks, K. R. and Carter, N. L.: Rheology of some continental lower crustal rocks, Tectonophysics, 182, 57–77, https://doi.org/10.1016/0040-1951(90)90342-6, 1990.

Wu, B., Conrad, C. P., Heuret, A., Lithgow-Bertelloni, C., and Lallemand, S.: Reconciling strong slab pull and weak plate bending: The plate motion constraint on the strength of mantle slabs, Earth and Planetary Science Letters, 272, 412–421, https://doi.org/10.1016/j.epsl.2008.05.009, 2008.

Yuen, D. A. and Schubert, G.: On the stability of frictionally heated shear flows in the asthenosphere, Geophysical Journal International, 57, 189–207, publisher: Blackwell Publishing Ltd Oxford, UK, 1979.

Zhang, L., Zlotnik, S., and Li, C.-F.: Anomalous Subduction Initiation: Young Under Old Oceanic Lithosphere, Geochemistry, Geophysics, Geosystems, 22, e2020GC009 549, https://doi.org/10.1029/2020GC009549, _eprint: https://agupubs.onlinelibrary.wiley.com/doi/pdf/10.1029/2020GC009549, 2021.

Zhong, X. and Li, Z.-H.: Forced Subduction Initiation at Passive Continental Margins: Velocity-Driven Versus Stress-Driven, Geophysical Research Letters, 46, 11 054–11 064, https://doi.org/10.1029/2019GL084022, _eprint: https://agupubs.onlinelibrary.wiley.com/doi/pdf/10.1029/2019GL084022, 2019.

Zhou, X., Li, Z.-H., Gerya, T. V., and Stern, R. J.: Lateral propagation–induced subduction initiation at passive continental margins controlled by preexisting lithospheric weakness, Science advances, 6, eaaz1048, 2020.

Zwaan, F., Chenin, P., Erratt, D., Manatschal, G., and Schreurs, G.: Complex rift patterns, a result of interacting crustal and mantle weaknesses, or multiphase rifting? Insights from analogue models, Solid Earth, 12, 1473–1495, 2021.

Zwaan, F., Erratt, D., Manatschal, G., Chenin, P., and Schreurs, G.: On the delayed expression of mantle inheritance–controlled strain localization during rifting, Geology, 52, 764–768, 2024.

Čı´žková, H., van Hunen, J., van den Berg, A. P., and Vlaar, N. J.: The influence of rheological weakening and yield stress on the interaction of slabs with the 670 km discontinuity, Earth and Planetary Science Letters, 199, 447–457, publisher: Elsevier, 2002.